University of Padova

Department of Information Engineering

Ph.D. course on Bioelectromagnetism and Electromagnetic Compatibility

XXI Cycle

Ph.D. Thesis

Evaluation of Uncertainty and Repeatability in Measurement: two application studies in Synchronization and EMC Testing

Supervisor: Ch.mo Prof. Claudio Narduzzi

Co-examiner: Dott. Ing. Alessandro Sona

Ph.D. candidate: Ing. Marco Stellini

January, 2009

Abstract

Efficient organization of measurement tasks requires the knowledge and characterization of the parameters and of the effects that may affect the measurement itself. Uncertainty analysis is an example of how measurement accuracy is often difficult to quantify. Repeatability also assumes a key role. This is the ability to replicate the tests and related measurements at different times. The research was focused on this aspect of analysis of test repeatability. Some specific case studies in the field of measurements relating to synchronization between network nodes and to measurements for Electromagnetic Compatibility have been considered.

Synchronization between the components of a system is a particularly important requirement when considering distributed structures. The network nodes developed for this research are based on both PCs with a Real Time operating system (RTAI) and Linux-based embedded systems (FOX Acme Systems Board) interfaced to an auxiliary module with a field-programmable gate array (FPGA). The aim of the tests is to measure and classify the uncertainty due to jitter in the Time Stamping mechanism, and consequently to evaluate the resolution and repeatability of synchronization achieved in different traffic conditions using a standardized protocol for synchronization (IEEE 1588-PTPd).

The work in the Electromagnetic Compatibility has likewise focused on the repeatability of measurements typical of some practical applications. Some experiments involving LISN calibration have been carried out and some improvements are presented to reduce uncertainty. Theoretical and experimental uncertainty analysis associated with the ESD tests has been conducted and some possible solutions are proposed. A study on the performance of sites for radiated tests (Anechoic chambers, open-area test site) has been started using simulations and experimental testing in order to assess the capability of different sites. Obtained results are compared with different reference sources.

Finally, the results of a research project carried out at the University of Houston for the propagation of electromagnetic fields are reported.

Sommario

Organizzare una efficiente campagna di misure richiede la conoscenza e la caratterizzazione dei parametri e degli effetti che possono influire sulla misura stessa. L'analisi dell'incertezza è un esempio di come l'accuratezza sia spesso difficile da quantificare. Oltre all'incertezza tuttavia assume un ruolo chiave la ripetibilità, ovvero la possibilità di replicare il test e le relative misure in momenti diversi. L'attività di ricerca ha riguardato proprio questo aspetto di analisi della ripetibilità dei test prendendo in considerazione alcuni casi di studio specifici sia in ambito di Misure relative alla Sincronizzazione tra nodi di un sistema distribuito sia di Misure per la Compatibilità Elettromagnetica.

La sincronizzazione è un'esigenza particolarmente sentita quando si considerano strutture di misura distribuite. I nodi di rete sviluppati per queste ricerche sono basati sia su PC dotati di sistema operativo Real Time (RTAI) sia su sistemi embedded Linux-based (Acme Systems FOX Board) interfacciati ad un modulo ausiliario su cui si trova un field-programmable gate array (FPGA). I test condotti hanno permesso di misurare e classificare l'incertezza dovuta al jitter nel meccanismo di Time Stamp, e conseguentemente di valutare la risoluzione e la ripetibilità della sincronizzazione raggiunta in diverse condizioni di traffico utilizzando un protocollo di sincronizzazione standardizzato secondo l'IEEE 1588 (PTPd).

In ambito di compatibilità elettromagnetica, il lavoro svolto si è concentrato sull'analisi della ripetibilità di misure tipiche di alcune applicazioni pratiche in ambito EMC. E' stata svolta una analisi approfondita dei fenomeni parassiti legati alla taratura di una LISN e sono stati introdotti alcuni miglioramenti costruttivi al fine di ridurre i contributi di incertezza. Si è condotta una indagine teorico-sperimentale sull'incertezza associata alla misura di immunità con generatore di scariche elettrostatiche e l'individuazione di possibili soluzioni. E' stato avviato uno studio sulle prestazioni dei siti per le misure dei disturbi irradiati (camere anecoiche, open-area test site) mediante simulazioni teoriche e prove 'in campo' al fine di valutare i limiti di impiego dei diversi siti e comparare i risultati ottenuti con sorgenti di riferimento.

Infine, vengono riportati i risultati di una ricerca svolta presso l'Università di Houston e relativa alla propagazione di campi elettromagnetici.

Contents

List of Figures

List of Tables

General Introduction

The lower the accuracy and precision of a measurement instrument are,
the larger the measurement uncertainty is.

My PhD thesis is based upon several different experiences regarding the set-ups and analysis of synchronization protocols, EMC measurements and test bed calibrations. All of these activities were born out of well-defined industrial application problems. The analysis of synchronization accuracy was suggested as an interesting research topic by Tektronix, a leader in test, measurement and monitoring equipment. Starting from the problems of synchronizing distributed network architectures, we realized specific test beds in the Electronic Measurement Laboratory of Padova University.
CREI-Ven, a licensed laboratory for EMC testing where I've worked during my PhD career, also played a large role in my studies. I participated in many activities concerning the repeatability of EMC tests and calibrations. It was a great experience that allowed me to view the many difficulties and problems that arise in a laboratory environment and the various solutions for these problems.
The first part of the thesis discusses tests and analysis for synchronization solutions. The second half typical problems regarding EMC measurements. Finally, a measurement project carried out in Houston University to deal with the evaluation of the inducted current for TASER application is described.
The common thread that links these activities is the application of fundamental metrological concepts in uncertainty and repeatability evaluation.

In general, the result of a measurement is only an approximation or estimate of the value of the specific quantity subject to measurement, that is, the measurand, and thus the result is complete only when accompanied by a quantitative statement of its uncertainty. In metrology, measurement uncertainty describes a region about an observed value of a physical quantity which is likely to enclose the true value of that quantity. Assessing and reporting measurement uncertainty is fundamental in engineering and experimental sciences. Within the scope of Legal Metrology and Calibration Services, measurement uncertainties are specified according to the ISO Guide to the Expression of Uncertainty in Measurement (abbreviated GUM) [1].

Two approaches are needed to estimating the sources of uncertainties: *Type A* and *Type B* evaluations.

Type A uncertainties are caused by unpredictable fluctuations in the readings of a measurement apparatus, or in the experimenter's interpretation of the instrumental reading; these

fluctuations may in part be due to interference of the environment with the measurement process. These effects are evaluated by statistical methods over repeated measurements.

Type B uncertainties are biases in measurement which lead to the situation where the mean of many separate measurements differs significantly from the actual value of the measured attribute and are estimated from any other information. This could be information from past experience of the measurements, from calibration certificates, manufacturer's specifications, from calculations, from published information, and from common sense.

Measurement uncertainty is related with both the random and systematic errors of a measurement, and depends on both the accuracy and precision of the measurement instrument. Random are errors where repeating the measurement gives a randomly different result. Systematic, where the same influence affects the result for each of the repeated measurements. All measurements are prone to systematic errors, often of several different types. Sources of systematic error may be imperfect calibration of measurement instruments, imperfect methods of observation, or changes in the environment which interfere with the measurement process. Distance measured by radar will be systematically overestimated if the slight slowing down of the waves in air is not accounted for. Incorrect zeroing of an instrument leading to a zero error is an example of systematic error in instrumentation. So is a clock running fast or slow.
There is not always a simple correspondence between the classification of uncertainty components into categories 'random' *Type A* and 'systematic' *Type B*. In fact, the nature of an uncertainty component is conditioned by the use made of the corresponding quantity, that is, how that quantity appears in the mathematical model that describes the measurement process. When the corresponding quantity is used in a different way, a random component may become a systematic component and vice versa. Thus the terms random uncertainty and systematic uncertainty can be misleading when generally applied.

Beyond the concept of uncertainty in the measure, the accuracy and repeatability of the test have a significant importance and are interesting specially for accreditation tests.
Accuracy is the degree of closeness of a measured or calculated quantity to its actual (true) value. Accuracy is closely related to precision, also called reproducibility or repeatability, the degree to which further measurements or calculations show the same or similar results. In fact, repeatability is the variation in measurements taken by a single person or instrument on the same item and under the same conditions. A measurement may be said to be repeatable when this variation is smaller than some agreed limit. According to the Guidelines for Evaluating and Expressing the Uncertainty of NIST Measurement Results [2], repeatability conditions include:

- the same measurement procedure;
- the same observer;
- the same measuring instrument, used under the same conditions;
- the same location;
- repetition over a short period of time.

While repeatability is the variation arising when all efforts are made to keep conditions constant by using the same instrument and operator, and repeating during a short time period, reproducibility is the variation arising using the same measurement process among different instruments and operators, and over longer time periods. Ideally a measurement device is both accurate and precise, with measurements all close to and tightly clustered around the known value. The accuracy and precision of a measurement process is usually established by repeatedly measuring some traceable reference standard [1] as shown in the figure.

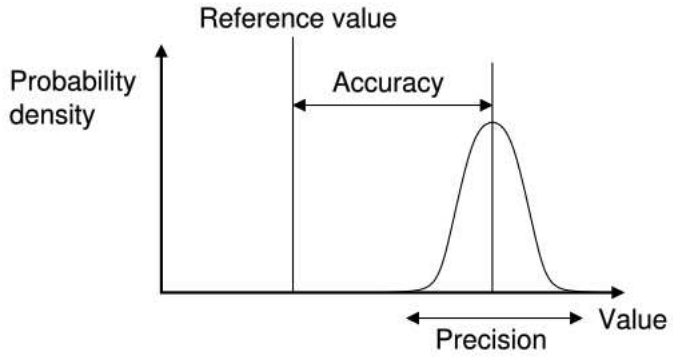

Figure 1: Accuracy

Calibration tasks also play a key role in measurement accuracy. Calibration is the process of comparing a known device, which will be called a standard reference, to an unknown device, which will be referred to as the instrument under test. In other words, calibration is the process of comparing a measurement device whose accuracy is unknown or has not been verified to one with known characteristics. The purposes of calibration are to ensure that a measurement device is functioning within the limit tolerances that are specified by its manufacturer, characterize its performance, or ensure that it has the accuracy required to perform its intended task.

In the work described in this Ph.D. thesis general methods for the analysis and evaluation of uncertainty and repeatability have been applied to experimental problems in two different application areas, namely, time synchronization and EMC testing. In both parts of the work specific attention has been dedicated to the design of test beds and measurement layouts, whereby accuracy and repeatability can be thoroughly analyzed, and their influencing factors understood. The two problems considered in this work represent state of the art applications, where analysis and minimization of uncertainty is one of the essential requirements for successful implementations. Experimental results, proposed in the first part, are analysed to evaluate the accuracy of synchronization task in different network architectures. These tests were implemented in the Electronic Measurement Laboratory of the Engineering Faculty of the University of Padova. PCs and embedded systems are used as general net-node and the IEEE 1588 precision time protocol is used for the synchronization process. A special effort is made to obtain high accuracy in the time-stamp mechanism and consequently low uncertainty in the final results. Part I describes hardware and software implementations used in the tests and discusses the results in

[1] A reference standard is the highest level of measurement standard available in a calibration facility for a particular measurement function.

terms of maximum resolution of synchronization.
Electromagnetic compatibility (EMC) tests and calibrations are instead investigated in the second part. Special devices like an anechoic chamber, open-area test site or climatic chamber are required for an accurate analysis, so all these tests were performed in an electronic research center in Padova. Significant results presented in the chapters of Part II regard: (i) some issues concerning the measurement accuracy of radiated emission for products in the electromagnetic compatibility test stage, (ii) the accurate calibration of LISN (Line Impedance Stabilization Network) focusing on the effects of parasitic parameters, (iii) the analysis of uncertainty contributions and repeatability in electrostatic discharge tests.
Finally, in chapter 6, experimental results of a research project regarding measurement of induced current for TASER application are reported. This project was carried out during a period at the University of Houston, Department of Electrical and Computer Engineering.

Part I

Analysis of Accuracy in Time Synchronization

Introduction - Part I

The first part of this thesis introduces the main concepts in time synchronization and presents some test beds designed to evaluate synchronization performances and accuracy for a generic network environment in a variety of different conditions. The distribution of a time reference has long been a significant research topic in measurement. Over the years, traditional methods based on radio broadcasting have been complemented by satellite-based reference systems (namely, the Global Positioning System, GPS) and, lately, supplemented by network-based time distribution. In fact, local area network (LAN) technology is increasing its importance in the field of instrumentation and measurement, following the adoption of LXI (LAN eXtensions for Instrumentation) as the main support for communication and data exchange within a measuring system. LANs are also widely used for distributed measurement and control in industrial environments, where restrictive time-constraints must be considered. Analysis on synchronization when no dedicated hardware is present in a node, effects of network traffic, as well as the study of timestamping inaccuracies are presented. Tests show the capabilities and limitations of different network synchronization approaches when a generic, heterogeneous network environment is considered.

Measurement and control systems are widely used in test and measurement, industrial automation, communication systems, electrical power systems and many other areas of modern technology. The timing requirements placed on measurement and control systems are becoming increasingly stringent. Traditionally these systems have been implemented in a dedicated architecture in which timing constraints are met by careful attention to programming combined with communication technologies with deterministic latency. In recent years an increasing number of such systems increasingly utilize a distributed architecture and networking technologies. We here intend distributed topology like a system in which hardware components are located in geographically diverse areas, consequently networked nodes communicate and coordinate their actions only by passing messages. When the instrument is part of a distributed measurement system, the localization, instrument calibration and time synchronization become needed for accurate measure.
Localization is a geographical problem that becomes complex when devices frequently change location. Instrument calibration is a more classical topic, some examples are proposed in the next section of this thesis (Part II). Finally, timing requirements are investigated here, specially in term of synchronization among nodes. In systems where devices are located very near to each other, typically a few meters, sharing a common timing signal is generally the easiest and most accurate method of synchronization. Instead, sharing a common timing signal becomes

unfeasible when the distance between devices increase. Even at moderate distances, e.g. 50 meters, a common timing signal may require significant costs for cabling and configuration. This has led to alternate means for enforcing the timing requirements in such systems. One such technique is the use of wired Ethernet communications which are becoming more common in measurement and control applications. In a general network environment the most widely used technique for synchronizing the clocks is the Network Time Protocol, NTP, or the related SNTP.
Measurement and control systems have a number of specific requirements that must be met by a clock synchronization technology. In particular:

- Timing accuracies are often in the sub-microsecond range,
- These technologies must be available on a range of networking technologies including Ethernet but also other technologies found in industrial automation and similar industries,
- A minimum of administration is highly desirable,
- The technology must be capable of implementation on low cost and low-end devices,
- The required network and computing resources should be minimal.

The level of precision achievable depends heavily on time jitter (the variation in latency) in the network also due to the topology. Point-to-point connections provide the highest precision. Hubs impose relatively little network jitter. Under very low or no network load, switches have a very low processing time, typically 2 to 10 μs plus packet reception time, and have low latency jitter of about 0.4 μs. But with network switches, a single queued maximum length packet imposes a delay for the following packet of about 122 μs, and under high load conditions, more than one packet can be in the queue. Variable switch latency means that raw data sent from two different data acquisition nodes to the same receiving node may be delayed differently. Prioritization of packets, eg: IEEE 802.1p, does not fully solve the problem, as at least one long packet can be in front of a synchronization packet and so will impose up to 122 μs to the jitter of transmission.
An effective way to reduce the effect of jitter in Ethernet networks is the use of dedicated system components that contain real-time clocks or transparent switches. However this solution presents some practical problems specially for the high costs. The commonly used switched Ethernet is a preferred solution for many applications due to the price decrease, high bandwidth, priority features (e.g. VoIP) and the ready availability of Ethernet switches and Ethernet enabled products fulfilling industrial environment requirements. In this case switch latency will vary depending on the switch load. This implies time jitter in synchronization mechanism that can be solved if the raw data are time stamped [2]. The receiving node can resend the incoming raw data based on the time stamps, and raw data from several acquisitions can be correctly compared. So, devices periodically exchange information and adjust their local timing sources to match each other.

[2]Time Stamp: is the operation for denoting the date and/or time at which a certain event occurred.

IEEE 1588

The timing accuracy that can be achieved in a LAN based on switched Ethernet, where time synchronization data is distributed via general infrastructure, depends on two factors:

1. Time stamping of incoming and outgoing time packets. Time stamping shall preferably be performed at the lowest possible level in the OSI protocol stack in order to avoid the variable latency through the protocol stack.

2. Variable network latency. The switch latency depends on the network load, drop link speed, packet sizes and the switch architecture.

The synchronization of distributed clocks requires a continuous process. A clock is essentially a two part device, consisting of a frequency source and an accumulator. A typical example of 2 clocks that need to maintain the same time is schematically shown in figure 2. The initial offset represents the difference at the moment in which the synchronization protocol starts. Calling $P_1 = \frac{\partial Clock_1}{dt}$ the time derivative of first clock and $P_2 = \frac{\partial Clock_2}{dt}$ the time derivative of second clock, in general we have $P_1 \neq P_2$. In theory, if two clocks were set identically and their frequency sources ran at the exact same rate, they would remain synchronized indefinitely. In practice, however, clocks are set with limited precision, frequency sources run at slightly different rates, and rate of a frequency source changes over time and temperature. Most modern electronic clocks use a crystal oscillator as a frequency source. The frequency of a crystal oscillator varies due to initial manufacturing tolerance, temperature and pressure changes, and aging. Because of these inherent instabilities, distributed clocks must continually be synchronized to match each other in frequency and phase.

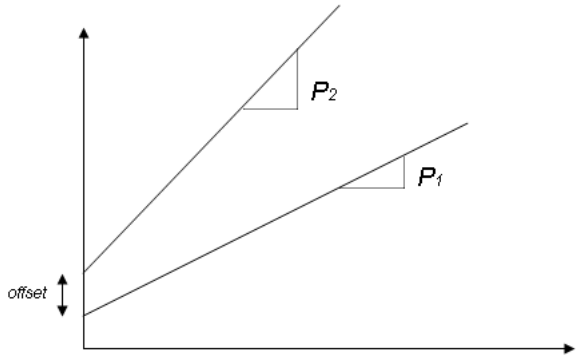

Figure 2: drift

IEEE 1588 provides a standard protocol for synchronizing clocks connected via a multicast capable network, such as Ethernet. Released as a standard in 2002, IEEE 1588 was designed to provide fault tolerant synchronization among heterogeneous networked clocks requiring little network bandwidth overhead, processing power, and administrative setup. IEEE 1588 provides this by defining a protocol known as the precision time protocol, or PTP. A heterogeneous network of clocks is a network containing clocks of varying characteristics, such as the origin of a clock's time source, and the stability of the clock's frequency. The PTP protocol provides a fault tolerant method of synchronizing all participating clocks to the highest quality clock in

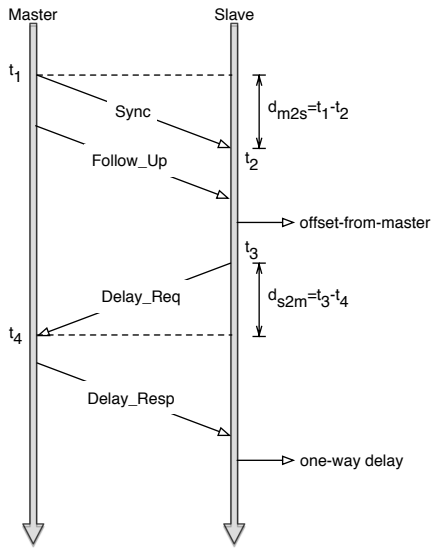

Figure 3: IEEE 1588 multicast communications

the network. IEEE 1588 defines a standard set of clock characteristics and defines value ranges for each. By running a distributed algorithm, called the best master clock algorithm (BMC), each clock in the network identifies the highest quality clock; that is the clock with the best set of characteristics.
The highest ranking clock is called the 'grandmaster' clock, and synchronizes all other 'slave' clocks. If the 'grandmaster' clock is removed from the network, or if its characteristics change in a way such that it is no longer the 'best' clock, the BMC algorithm provides a way for the participating clocks to automatically determine the current 'best' clock, which becomes the new grandmaster. The best master clock algorithm provides a fault tolerant, and administrative free way of determining the clock used as the time source for the entire network.
Slave clocks synchronize to the 1588 grandmaster by using bidirectional multicast communication (see figure 3). The grandmaster clock periodically issues a packet called a 'sync' packet containing a timestamp of the time when the packet left the grandmaster clock. The grandmaster may also, optionally, issue a "follow up" packet containing the timestamp for the sync packet. The use of a separate "follow up" packet allows the grandmaster to accurately timestamp the 'sync' packet on networks where the departure time of a packet cannot be known accurately beforehand. For example, the collision detection and random back off mechanism of Ethernet communication prevents the exact transmission time of a packet from being known until the packet is completely sent without a collision being detected, at which time it is impossible to alter the packet's content.

A slave clock receives the grandmaster's 'sync' packet and timestamps the packet's arrival time using its own clock. The difference in the 'sync' packet's departure timestamp and the 'sync' packet's arrival timestamp is the combination of the slave clock's offset from the master and the network propagation delay. By adjusting its clock by the offset measured at this point, the offset between the master and slave can be reduced to the network propagation delay only. IEEE 1588 operates under the assumption that the network propagation delay is symmetrical.

That is, the delay of a packet sent from the master to the slave is the same as the delay of a packet sent from the slave to the master. By making this assumption, the slave can discover, and compensate for the propagation delay. It accomplishes this by issuing a 'delay request' packet which is time stamped on departure from the slave. The 'delay request' message is received and time stamped by the master clock, and the arrival timestamp is sent back to the slave clock in a 'delay response' packet. The difference in these two timestamps is the network propagation delay.

By sending and receiving these synchronization packets, the slave clocks can accurately measure the offset between their local clock and the master's clock. The slaves can then adjust their clocks by this offset to match the time of the master. The IEEE 1588 specification does not include any standard implementation for adjusting a clock; it merely provides a standard protocol for exchanging these messages, allowing devices from different manufacturers, and with different implementations to interoperate.

One of the most common implementation is PTPd (daemon) described in [13]. PTPd is a complete implementation of the IEEE 1588 specification and the source code is freely available under a BSD-style license.

Chapter 1

Test Bed description

In this chapter two different test beds for synchronization analysis are proposed. As recalled in the introduction, PTP synchronization relies on the exchange of data packets containing timestamps. In the net, timestamps are generated both by the node acting as time reference and by the node which requires synchronization. The end result depends on two main factors: timestamping accuracy and symmetry of packet propagation delays.
The aim of the investigation is to understand how accurate a software implementation of PTP can be. As noted before, dedicated hardware can be effective, but expensive solutions. Since software-only implementations of the PTP protocol have been proposed on the literature, it is interesting to understand their potential as well as their limitations, in view of their much more limited cost.
Software timestamping is affected by many concurrent activities in a computer system, like kernel tasks, intensive disk IO or other traffic in the network interface. It is well known that, to achieve high accuracy, timestamping should be performed at the Media Access Control (MAC) level within the network interface card. If software-only implementations are considered, packet time-stamping needs to be implemented as a real-time activity within the operating system kernel and enjoy high priority. To this aim special solutions are used in the proposed tests: in the first case using a real-time operating system, in the second one using embedded systems.
The PTP implementation employed for these works is the PTP daemon (PTPd) discussed in the introduction.

1.1 Timing accuracy of scheduled software tasks

An operating system (commonly abbreviated OS) is the software component of a computer system that is responsible for the management and coordination of activities and the sharing of computer resources. The operating system acts as a host for applications that are run on the machine. As a host, one of the purposes of an operating system is to handle the details of the operation of the hardware. This relieves application programs from having to manage these details and makes it easier to write applications. Almost all computers, including handheld computers, desktop computers, supercomputers, and even video game consoles, use an operat-

ing system of some type. Some of the oldest models may however use an embedded operating system, that may be contained on a compact disk or other data storage device.
Operating systems offer a number of services to application programs and users. Applications access these services through application programming interfaces (APIs) or system calls. By invoking these interfaces, the application can request a service from the operating system, pass parameters, and receive the results of the operation (figure 1.1). Executing a program involves

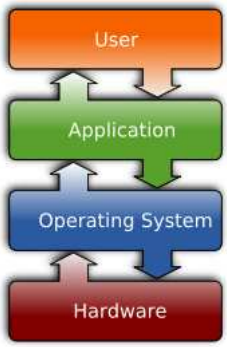

Figure 1.1: A layer structure showing where Operating System is located on generally used software systems on desktops

the creation of a process by the operating system. The kernel creates a process by setting aside or allocating some memory, loading program code from a disk or another part of memory into the newly allocated space, and starting it running.
Interrupts are central to operating systems as they allow the operating system to deal with the unexpected activities of running programs and the world outside the computer. Interrupt-based programming is one of the most basic forms of time-sharing, being directly supported by most CPUs. Interrupts provide a computer with a way of automatically running specific code in response to events. Even very basic computers support hardware interrupts, and allow the programmer to specify code which may be run when that event takes place.
When an interrupt is received, the computer's hardware automatically suspends whatever program is currently running by pushing the current state on a stack, and its registers and program counter are also saved. This is analogous to placing a bookmark in a book when someone is interrupted by a phone call. This task requires no operating system as such, but only that the interrupt be configured at an earlier time.
In modern operating systems, interrupts are handled by the operating system's kernel. Interrupts may come from either the computer's hardware, or from the running program. When a hardware device triggers an interrupt, the operating system's kernel decides how to deal with this event, generally by running some processing code, or ignoring it. The processing of hardware interrupts is a task that is usually delegated to software called device drivers, which may be either part of the operating system's kernel, part of another program, or both. Device drivers may then relay information to a running program by various means.
A program may also trigger an interrupt to the operating system, which are very similar in function. If a program wishes to access hardware for example, it may interrupt the operating system's kernel, which causes control to be passed back to the kernel. The kernel may then process the request which may contain instructions to be passed onto hardware, or to a device

driver. When a program wishes to allocate more memory, launch or communicate with another program, or signal that it no longer needs the CPU, it does so through interrupts.

Common contemporary operating systems include Microsoft Windows, Mac OS, Linux and Solaris. Microsoft Windows has a significant majority of market share in the desktop and notebook computer markets, however for applications where a hard layer access is required Linux systems represent the best solutions. Linux is a standard time-sharing operating system which provides good average performance and highly sophisticated services. Linux suffers from a lack of real time support. To obtain a timing correctness behavior, it is necessary to make some changes in the kernel sources, i.e. in the interrupt handling and scheduling policies. In this way, you can have a real time platform, with low latency and high predictability requirements, within full non real time Linux environment (access to TCP/IP, graphical display and windowing systems, file and data base systems, etc.).

1.1.1 RTAI Extension

Accuracy in recording the interrupt time is essential. The operation should be implemented by a specific real-time software task within the operating system kernel; for this reason a real-time operating system (RTOS) is required, so that a deterministic time from event to system response is ensured []. A real time system can be defined as a "system capable of guaranteeing timing requirements of the processes under its control". In fact, an RTOS does not necessarily have high throughput; rather, an RTOS provides facilities which, if used properly, guarantee deadlines can be met generally (soft real-time) or deterministically (hard real-time). An RTOS will typically use specialized scheduling algorithms in order to provide the real-time developer with the tools necessary to produce deterministic behavior in the final system. An RTOS is valued more for how quickly and/or predictably it can respond to a particular event than for the given amount of work it can perform over time. Key factors in an RTOS are therefore a minimal interrupt latency and a minimal thread switching latency.
Since an interrupt handler blocks the highest priority task from running, and since real time operating systems are designed to keep thread latency to a minimum, interrupt handlers are typically kept as short as possible. The interrupt handler defers all interaction with the hardware as long as possible; typically all that is necessary is to acknowledge or disable the interrupt (so that it won't occur again when the interrupt handler returns). The interrupt handler then queues work to be done at a lower priority level, often by unblocking a driver task (through releasing a semaphore or sending a message). The scheduler often provides the ability to unblock a task from interrupt handler context.

The choice for the RTOS used in the tests fell on RTAI (Real Time Application Interface []). It is a real-time extension for the Linux kernel - which allows the implementation of applications with strict timing constraints. RTAI is a patch to the standard Linux kernel and a library which has a hardware abstraction layer, a real-time scheduler and real-time interprocess communication (IPC) services. RTAI offers the same services of the Linux kernel core, adding the features of an industrial real time operating system. It consists basically of an interrupt

dispatcher: RTAI mainly traps the peripherals interrupts and if necessary re-routes them to Linux. It is not an intrusive modification of the kernel; it uses the concept of HAL (hardware abstraction layer) to get information from Linux and to trap some fundamental functions. This HAL provides few dependencies to Linux Kernel. RTAI considers Linux as a background task running when no real time activity occurs. Since the documentations describe simple and easy the adaptation in the Linux kernel, our experience in the RTAI installation was very complicated. In fact it requires a good knowledge in Linux systems and kernel configurations.

1.1.2 Time response performance

This paragraph shows the results obtained when measuring real-time behaviour of a RTAI-Linux operating system running on standard PC platforms. During this study, we've focused on a comparison of the time response in the RTAI system with respect to a non real time system. In particular, we have measured the time elapsed between the interrupt signal activation and the start of the interrupt routine, via counter values stored in a digital oscilloscope.
The schematic representation of test bed is reported in figure 1.2. The signal generated by

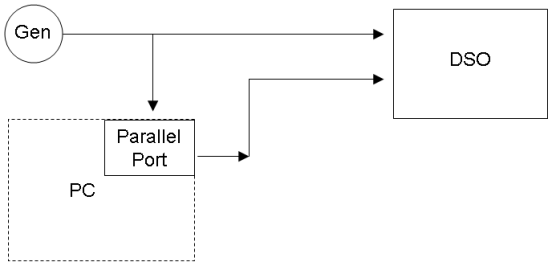

Figure 1.2: Parallel-test

the Agilent 33220A (GEN) goes both in the parallel port of the PC and in one channel of the Tektronix TDS 5032B oscilloscope (DSO). PC is a pentium MMX with Slackware Linux 10.2 patched with RTAI 3.0r4. Signal received in the input pin of parallel port generates an interrupt in the PC which runs a special task-module as discussed later. This module switches the voltage level at an output pin of the same port, so that the response time could be directly measured by a digital oscilloscope.
Test is done two times, with or without RTAI task application. (inserire cofigurazione della misura) Screens shot of measured system response delay are shown on figures 1.3(a) and 1.3(b). Recorded with infinite trace persistence time, rising edge is the input stimulus, falling edges are responses. Tests have evidenced that an interrupt generated in the parallel port is served with an average response delay of the order of 3 μs both with and without real time system. However, in the case of non real time system, response time presents many longer contributions over 500 μs (fig. 1.3(a)). Instead with RTAI system the response delay is normally between 1.2 μs and 5.6 μs; mean value is 3.14 μs and the standard deviation is 0.94 μs. Occasionally response times are longer, up to about 12 μs (fig. 1.3(b)). It can be assumed that the assessment can be applied as well to timestamping accuracy. In figure 1.4 the histogram of response delays is plotted in the upper half of the display and refers to a set of 1000 responses.

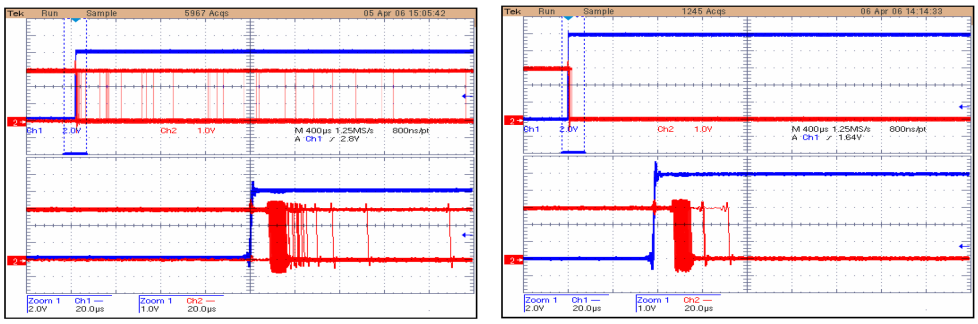

(a) (b)

Figure 1.3: 1.3(a) Normal s.o. response and 1.3(b) RTAI s.o. response

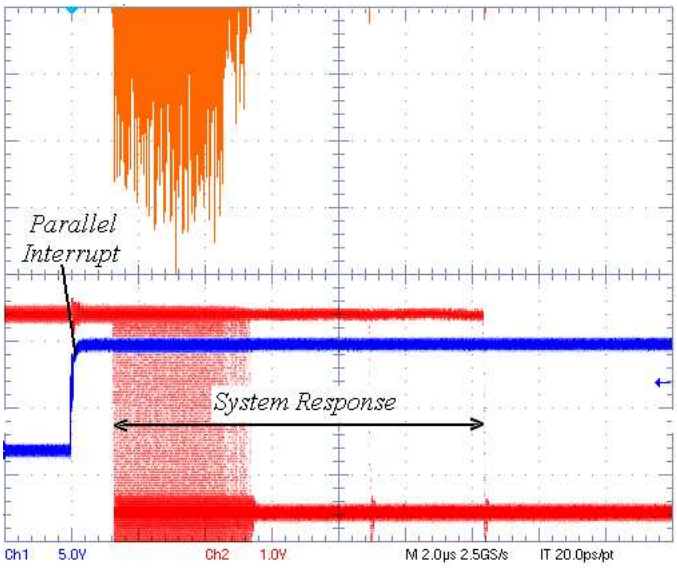

Figure 1.4: RTAI histogram of 1000 responses

1.2 First Test Bed Implementation - PC nodes with background traffic

In order to investigate the characteristic of the PTP implementation and the performances of the synchronization in the distributed network environments, an experimental set up is here proposed. Main characteristic is the presence of software time stamp to monitoring the node clocks and consequently the accuracy of synchronization. The test bed, shown in figure 1.5, is composed of the following elements:
- PC_1 and PC_2 are two identical PCs, using Pentium III 600MHz processors and running SUSE Linux version 9.2, which exchange PTP synchronization messages;
- PC_3 is a Windows PC using a Pentium III 550MHz processor and equipped with Windows 2000 Professional. This machine supports large data transfers to the PCs under test. This is done by having PC_1 and PC_2 execute a continuous FTP 'get' operation from PC_3;
- a common commercial SWITCH allows connection among the nodes;
- GEN is a signal generator providing an accurate timing pulse, which is sent to PC_1 and PC_2 simultaneously.

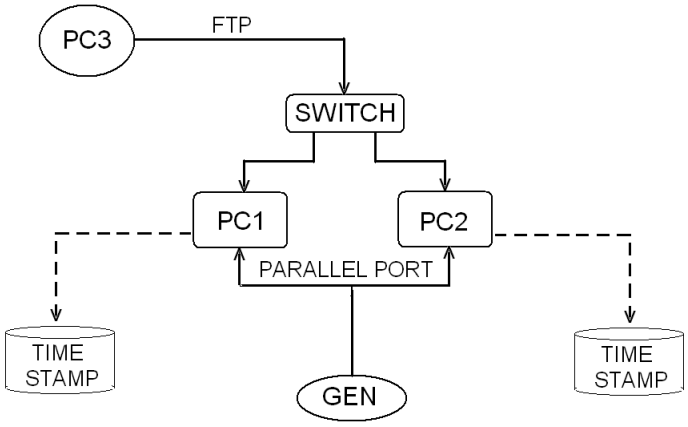

Figure 1.5: realized PTP test bed.

The test bed presents a sufficiently stable and accurate time reference (SPECIFICHE STRUMENTO) obtained from an external generator (Tektronix AFG3021). The pulse provided by the generator is fed into a parallel port input of both PC_1 and PC_2, whereby a hardware interrupt is generated. This triggers a time-stamping operation: a real-time process, implemented within each computer, handles the interrupt, reads the system time and writes the resulting timestamp into a log file. The purpose of the test is to evaluate the capability of the two nodes PC_1 and PC_2 to track each other. By comparing the log file of PC_1 with the log file of PC_2, information regarding the effective synchronization between the PCs are obtained.
The procedure is similar to the actual timestamping process that a node carries out when a PTP packet is received and should have a very similar behavior. Therefore both PC_1 and PC_2 had the RTAI 3.1 patch installed.

The code used for software time stamp is reported below:

```
#include <linux/module.h>
#include <rtai.h>
#include <rtai_sched.h>

#define BASEPORT 0x378

int count=0;
struct timeval tval;

static void handler(void)
{
        count++;
        do_gettimeofday(&tval);
        outb_p(count,BASEPORT);
        rt_printk(">>> timestamp = %d \t; %d \n", tval.tv_sec, tval.tv_usec);
        rt_ack_irq(7);
}

int xinit_module(void)
{
        int ret;
        ret = rt_request_global_irq(7, (void *)handler);
        rt_enable_irq(7);
        outb_p(0x10, BASEPORT + 2);//set port to interrupt mode; pins are output
        do_gettimeofday(&tval);
        rt_printk(">>> inizio = %d \t; %d \n", tval.tv_sec, tval.tv_usec);
        rt_set_oneshot_mode();
        return 0;
}

void xcleanup_module(void)
{
        rt_printk("Unloading  parallel port latency test\n");
        rt_disable_irq(7);
        rt_free_global_irq(7);
}

module_init(xinit_module);
module_exit(xcleanup_module);
MODULE_LICENSE("GPL");
```

To simulate traffic into the LAN, another program can be run in the PCs under test, which performs continuous downloads from the FTP server with a speed of about 32 Mbps over Fast Ethernet for each PC (total: 64 Mbps). Inclusion of the FTP server PC_3 in the architecture allows the assessment of PTP performances in a network carrying a significant and unbalanced traffic load. It is also important to assess the effects of different degrees of activity in the nodes. To simulate computer activities in a controlled way, two programs were written; one (*CPU-jam*) keeps the CPU busy and another (*disk-jam*) forces the PC to continuously write data on its hard disk. For most tests we used a normal 100Mb Ethernet switch without boundary

clock, while a 10Mb Ethernet switch was used to simulate a network bottleneck.

1.3 Second Solution - Synchronization with emulated cross-traffic

We now shall take a more general view of the synchronization problem and consider generic network environments where distributed measurement may coexist with other network applications. An example is provided by a system where instruments or sensor nodes exchange data while sharing the same network infrastructure with applications such as network printers, IP telephony and so on. It should be remembered that timing protocols are only one facet of the synchronization problem. In fact, the protocol has the task of assuring that accurate timing information are propagated to all nodes within a synchronization domain. The next step is the implementation of a suitable procedure for regulating the local clock, ensuring that it tracks the reference to within desired bounds (this is sometimes called a clock servo). In generic network environments it is also necessary to account for at least two other factors: one is the presence of traffic, which causes the packets carrying timing information to suffer from variability in propagation time; the other is the degree of accuracy with which time is recorded, by packet timestamping, at different nodes.
In the next tests the network nodes are two embedded systems Linux based.

1.3.1 Embedded Systems

An embedded system is a special-purpose computer system designed to perform one or a few dedicated functions,[!!] often with real-time computing constraints. It is usually embedded as part of a complete device including hardware and mechanical parts. In contrast, a general-purpose computer, such as a personal computer, can do many different tasks depending on programming. Embedded systems control many of the common devices in use today.

Since the embedded system is dedicated to specific tasks, design engineers can optimize it, reducing the size and cost of the product, or increasing the reliability and performance. Some embedded systems are mass-produced, benefiting from economies of scale.

Physically, embedded systems range from portable devices such as digital watches and MP3 players, to large stationary installations like traffic lights, factory controllers, or the systems controlling nuclear power plants. Complexity varies from low, with a single microcontroller chip, to very high with multiple units, peripherals and networks mounted inside a large chassis or enclosure.

In general, ‘embedded system’ is not an exactly defined term, as many systems have some element of programmability. For example, Handheld computers share some elements with embedded systems - such as the operating systems and microprocessors which power them - but are not truly embedded systems, because they allow different applications to be loaded and peripherals to be connected.

Embedded systems are interesting for this work because they typically allow lower level access to system resources. It can be assumed that the system clock is among the accessible

resources which that modifications are faster and less affected by jitter.

The system chosen for the tests is the FOX Board [3]. The FOX Board is an Embedded Linux Core Engine with reduced size and low power requirements. This system has an ETRAX 100LX microprocessor, a 100MIPS RISC CPU made by Axis Communications and 16MB of RAM. Presents some interfaces like Ethernet 10/100Mb port, 2 USB host 1.1, slots for two 20x2 pin strip step with 48 I/O lines, I2C bus, SPI, serial and parallel ports. Through the ethernet interface it is possible to have access to the internal Web server, FTP server, SSH, Telnet and the complete TCP/IP stack. Moreover, a free and Open Source Software Development Kit are available which enables a strong customization of Linux Kernel.

1.3.2 Test Bed

A schematic representation of the test bed is illustrated in figure 1.6. Node 1 and Node 2 represent the systems that need to execute simultaneous operations at a given time. For this purpose they must first be synchronized by a suitable protocol. The Source node generates cross-traffic with a given profile towards the Sink node, the latter simply destroying the received packets. The Hub is used to allow communication among the nodes which, in real life, might be separated by a whole network. In a more complex test environment, its place could be taken by a network emulator (such as, for instance, NIST Net); however, for the aims of this work a hub is enough, since it fulfills the basic purpose of mixing the timing packets exchanged between the two nodes with an external packet flow designed to reproduce the desired traffic profile. To monitoring the traffic, there is one measure point. It consist on one PC with DAG card [1] which allows to capture all packets into the net.

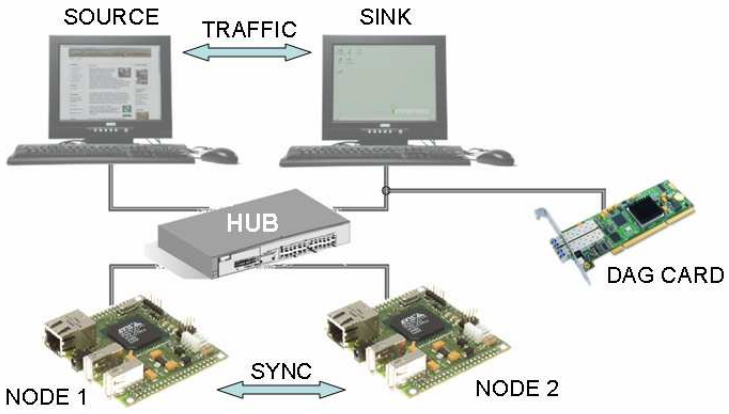

Figure 1.6: Test environment.

The test bed configuration differs from the previously one, where a Source node interacts with either Node 1 or Node 2, causing it to carry out data transfers. The latter is representative of the case when a remote measuring instrument needs to send significant amounts of data over the network. This set up considers instead the more common case where accurate time refer-

[1] DAG network monitoring interface cards provide 100% packet or cell capture, regardless of interface type, packet size, or network loading.

encing is an important issue, but measuring nodes generate and exchange limited amounts of data. Cross-traffic then assumes a great importance when the performance of synchronization protocols must be evaluated in networks characterized by the convergence of different applications. In this context it plays an important role and needs to be accurately modeled. The emphasis of the tests is on the effects of cross-traffic on the one-way delay of packets containing timing information.

1.3.3 Cross traffic generation

Different strategies can be adopted to emulate cross-traffic, however some constraints must be taken into account. First of all traffic models must reproduce real traffic properties, which are well described in the literature [6], in a general way not limited to some specific situation. This is a very important feature since there is a rapid evolution in network applications and in their behavior, so the attention must not be focused on a particular scenario.

It is also desirable to handle models whose parameters have a physical meaning and that can be strictly controlled to evaluate synchronization issues under well defined test conditions.

We chose to model packet traffic using ON/OFF sources that can be modeled with chaotic maps. This analytical model is able to accurately and concisely represent network traffic, in particular its strong correlation at all the time scales of engineering interest. This property, usually known as long range dependence (LRD), leads to a self-similar model of traffic. The Hurst parameter H [6] provides a measure of traffic correlation degree and needs to be taken into account since it strongly affects delays in network buffers.

Chaotic maps, proposed as traffic model in [7], are low dimensional nonlinear systems whose time evolution is described by the knowledge of an initial state and a set of dynamical laws. The traffic generator is an ON/OFF source that sends one packet when the source is in the ON state, while no packets are transmitted when the source is in the OFF state. A one-dimensional chaotic map is used to describe state changes. This map has a state variable xn that evolves over time according to the nonlinear system:

$$x_{n+1} = f_1(x_n), \qquad \text{if:} \qquad 0 < x_n \leq d\text{that is:} y_n = 0; \tag{1.1}$$

$$x_{n+1} = f_2(x_n), \qquad \text{if:} \qquad d < x_n < 1\text{that is:} y_n = 1, \tag{1.2}$$

where y_n is the indicator variable, describing the state of the source during the n-th time interval $[(n-1)\cot T, n \cdot T)$. If the indicator variable is zero the source is OFF, while if y_n is equal to 1 the source is ON.

The functions $f_1(x_n)$ and $f_2(x_n)$ are respectively given by:

$$f_1(x_n) = x_n + (1-d)\left(\frac{x_n}{d}\right)^{m_1} \tag{1.3}$$

$$f_2(x_n) = x_n - d\left(\frac{1-x_n}{1-d}\right)^{m_2} \tag{1.4}$$

where $m_1,\ m_2 \in (1,2)$ and $d \in (0,1)$ are the parameters of the map.

The average number of packets generated by the map represents the traffic load λ , which is related to the probability that the source is in the ON region. Analytical approximations for calculating the traffic load can be found in the literature and are out of the scope of this paper. However it is important to note that this traffic parameter is strongly dependent on the map parameter d, which specifies the ratio between the ON and OFF region. In particular, the value of λ is greater for d near to zero, while it becomes smaller as d tends to 1.

1.3.4 Implementation issues

The proposed ON-OFF chaotic traffic source has been implemented by using the client-server paradigm. In this implementation the server represents the traffic *Source* of figure 1.6, while the client represents the traffic *Sink*. At the client side, the user sets the source parameters $m_1,\ m_2,\ d$ and T. These parameters are successively sent to the server by using a control channel over TCP in order to obtain a reliable communication. After receiving the source parameters, the server starts to send UDP packets toward the client as specified by the chaotic map described in this paragraph. We chose the UDP transport protocol to generate cross-traffic in order to avoid packet retransmissions and in general flow control, that otherwise would modify the statistical traffic model. The control channel is finally used by the client to stop traffic generation.

Some remarks need to be carefully considered in cross-traffic generation. In fact there is a strict relationship between the time step T of the packet generator at the source and the data rate R of the real system. Let N_b be the byte length of packets generated by the traffic source. This means that a packet takes a time equal to $T_p = N_b/R$ to be transmitted over the wire. The ratio T_p/T provides the percentage of bandwidth occupied by the source.

The need to carry out tests with a realistic bandwidth occupation translates into a design requirement for the test bed. At present, T is limited to a minimum value of 1 ms by the Java implementation. Then, for a 100 Mb/s network, if $N_b = 500$, the packet time is $T_p = 40\ \mu s$ and $T_p/T = 4\%$, which is too low for the presence of cross-traffic to have some effect on the system. Since the actual implementation of traffic source cannot generate packets over shorter intervals, the other solution consists in slowing down the system rate by a time rescaling operation. Therefore by choosing a 10 Mb/s network, $N_b = 500\ byte$ and $T = 1\ ms$ we obtain $T_p = 400\ \mu s$ and $T_p/T = 40\%$. Finally, a bandwidth occupation equal to 100% can be obtained if the byte length of the packet is set to $N_b = 1,250\ byte$.

1.3.5 Validation of the traffic generator

The validation of the traffic generator is done by checking if the statistical properties of the actual traffic correspond to the parameters of the theoretical traffic model. As previously noted, the generated traffic should be self-similar with an estimated Hurst parameter not too far from the theoretical one.

The diagram reported in figure 1.7 is obtained by a well-known wavelet based statistical tool [12] for the analysis of long-range dependent network traffic. If in this plot an alignment can be found then traffic is LRD and the Hurst parameter can be estimated from the slope of the

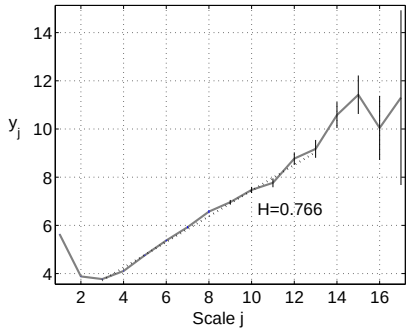

Figure 1.7: Hurst parameter estimation from measured data.

regression line. In this case, that corresponds to traffic used in Sec. VI.B, the estimated Hurst parameter is equal to $\hat{H} = 0.77$ that is in good agreement with the theoretical value $H = 0.78$.

Chapter 2

Synchronization Tests and Analysis

In this chapter tests carried out with different network setups are presented and discusses. Using the first test bed we observed: i) how long PTPd takes to achieve synchronization, to within a specified tolerance, starting from a given time offset; ii) the effective tracking accuracy that can be reached; iii) possible anomalies and events requiring more detailed analysis; iv) critical conditions that can influence PTP synchronization. The aim of the second test bed is to explore the capabilities and limitations of different network synchronization approaches when a generic, heterogeneous network environment is considered.

2.1 Preliminary Investigations

Using the first test bed proposed in 1.2 some tests have been conducted.

2.1.1 Single Clock Analysis

The two clocks of PC_1 and PC_2 were first measured separately. The generator was set to provide a reference pulse every 30 s (30 PPS) and the two PCs were left running free without PTPd. Tests evidence that both clocks are skewed with respect to the reference: PC_1 loses on average 33.4 μs/sec, while PC_2 loses on average 41.1 μs/sec (figure 2.1). Variability is limited to a range of $\pm$0.12 μs/s; this agrees very well with the timing variability shown in figure 1.4. Although the room where tests were carried out has no temperature control, conditions remained reasonably stable, therefore it can be assumed that the skew between the clocks of PC_1 and PC_2 has a constant value of about 7.8 μs/s. The PTP master sends a SYNC message over the network once every 2 s; in this time interval the estimated offset between PC_1 and PC_2 in the test bed would be about 15 μs.

2.1.2 Performance limits

In the first test PC_1 and PC_2 were directly connected via a cross cable. No other activity was undertaken and the link was free from other network traffic, allowing to assess the upper limit of synchronization performances. A reference timing pulse was generated every 30 s also in this case.

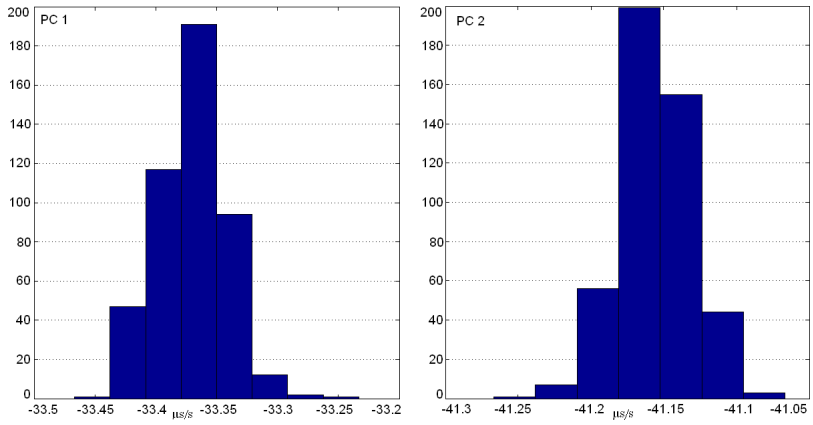

Figure 2.1: single clock of PC_1 and PC_2

Measurement results are illustrated in figure 2.2(a), which covers a 45 minute interval during which the time offset between master and slave clock have been plotted.
As a general trend, every test can be divided into three phases: the *start-up*, when the master clock is determined by comparing the two nodes; the *non-linear response phase*, during which the PTP algorithm progressively reduces the offset between the two nodes and whose length depends on the initial offset value; finally, the *linear-response phase*, where the PTP servo algorithm allows the two clocks to track each other more or less closely, depending on the particular network configuration. Confirming the clock analysis of previously section, the best clock algorithm always selected PC_1 as master clock in every test we performed, while servo clock is PC_2.

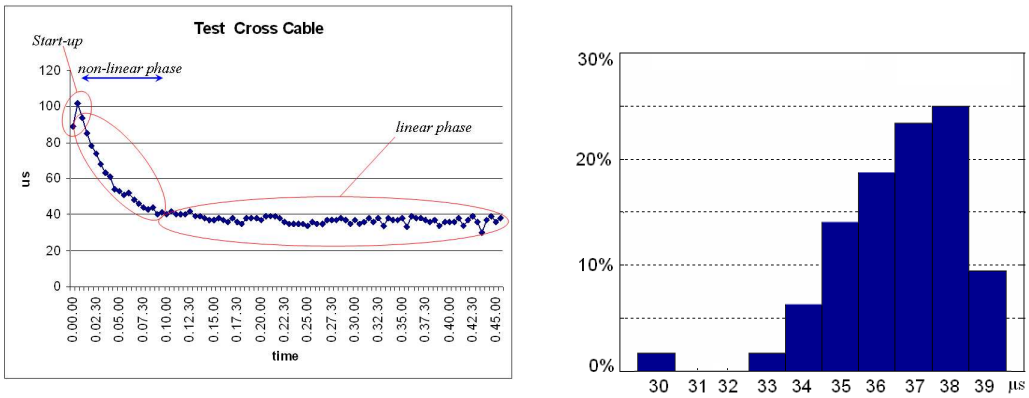

(a) (b)

Figure 2.2: 2.2(a): PTPd synchronization phases- 2.2(b): Test 1: PC_1 and PC_2 connected by a cross cable

When the clock servo has achieved good convergence, the tracking behavior is best described by plotting a histogram of measured values. Figure 2.2(b) shows the histogram of the time offset between master (PC_1) and slave (PC_2) in the final phase: the slave clock mean offset from the master is approximately 37 μs with a variability mostly within ± 3 μs around this value.

We did not analyze in detail the causes of the delay but, given the nature of the connection, it seems reasonable to assume that any possible path asymmetry would have to be related to the transmit and receive operations within the nodes. On the other hand, the extent of variability is still in good agreement with that of timestamping which, in this very simple configuration, is clearly the main factor of timing uncertainty.

2.1.3 Network switch

In this test the setup consists of PC_1 and PC_2 connected via a 100 Mbps switch. Without any additional network and computational load, the switch causes a larger offset than with the cross cable but doesn't appreciably increase variability. Figure 2.3(a) shows mean offset is about 51 μs.

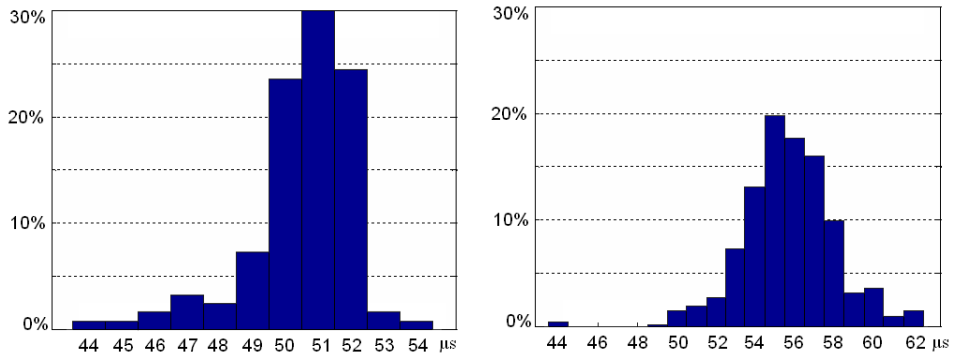

(a) (b)

Figure 2.3: PC_1 and PC_2 connected by a 100Mb/s switch: 2.3(a) Test 2 - 2.3(b) Test 2a with CPU-jam task running on both machines.

Another test with the 100Mb switch is shown in figure 2.3(b). In this case the *CPU-jam* software is running in both PCs and it can be noticed how the task introduces a modest increase in variability, as well as some abnormal events, that could be called delay spikes.

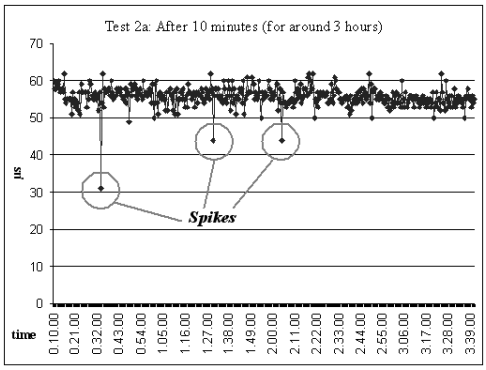

Figure 2.4: Test 2a: spikes caused by concurrent CPU activities.

These spikes are evidenced in figure 2.4, where the time offset between the two clocks during the linear-response phase is plotted for over three hours. They are probably due to

occasional situations where system resources for the real-time timestamping procedure cannot be released immediately, resulting in incorrect timestamp values.

2.1.4 Network traffic

An aspect that requires attention is the possible effect of network traffic on the exchange of PTP packets. In a LXI system, for instance, measuring instruments such as a modern digitizing oscilloscope may easily generate very large data streams when the acquired waveforms are transferred to the controller. This might occasionally increase the transit time of a PTP packet and, consequently, affect synchronization.
The next test demonstrates the influence of network traffic on PTPd. The full setup shown in figure 1.5 has been employed and the traffic load consists in a file transfer from PC_3 to the other nodes. This data stream takes up about 60% of the available bandwidth, possibly causing queuing delays and interfering with PTP packets. Figure 2.5(a) shows that the mean offset grows only slightly, to around 60 μs, but variability has increased by over an order of magnitude to about 140 μs and several delay spikes over 100 μs have occurred.

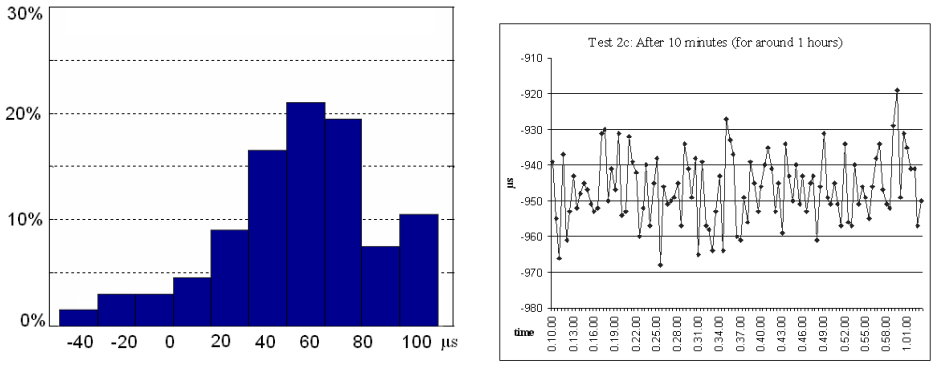

(a) (b)

Figure 2.5: 2.5(a) Test 2b: same as test 2a with additional FTP data stream - 2.5(b) Test 2c: same as test 2a with disk-jam task runing.

This behavior required further investigation; in particular, it would be important to determine whether the much greater offset variability is caused by increased and variable packet transit times within the network, or by a degradation of the real-time behavior of the timestamping procedure.
For this purpose the test was re-run, but execution of the *disk-jam* task replaced the FTP transfer activity. In this way, both CPUs are equally busy transferring data to and from the respective hard disks, but no network traffic is generated. Any PTP packet can be transmitted without delay, since the full network bandwidth is freely available. However, once the destination node is reached, the packet timestamping task may be hindered by disk read and write activities causing non-negligible interference, so that timestamps suffer from jitter. The effect is shown in figure 2.5(b), where the time offset measured during the linear-response phase is plotted for 50 minutes. The mean offset has changed very significantly, but variability remains within a comparatively narrow range of about 50 μs.
Interpretation of these results is not straightforward. The narrower range of delay variation,

compared to that of figure 2.5(a), could suggest that excessive network traffic and intensive disk IO share the responsibility for timing jitter: as already noted in [2], both factors may have detrimental effects on software-only timestamping. However, the test conditions under which figure 2.5(b) was obtained might instead mean that the system has almost been saturated by disk IO alone.

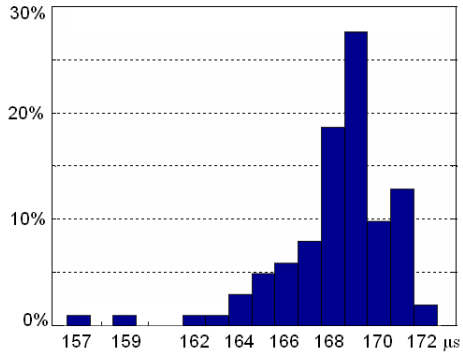

Figure 2.6: Test 3 with 10Mbps switch.

A similar effect is illustrated in figure 2.6, which refers to a test without any additional traffic load, where the 100Mb switch is replaced by a 10 Mb switch, causing a network bottleneck. In this case available bandwidth is reduced to just 10% and mean offset has increased to around 169 μs, but variability remains in the same range as in figure 2.3(b). Comparing figure 2.6 with the histograms of figures 2.3(b) and 2.5(a), it appears that variability is little affected by pure bandwidth reduction, the additional load caused by superposed network traffic being a more important factor.

2.1.5 Measurement Analysis

To summarize results of the previous sections, table 2.1.5 shows, for each test setup, the average time offset, statistical mode (the most common value obtained) and standard deviation, together with the maximum delay spikes (lower and higher) detected during the tests.

Network Setup	Time offset [μs]			Delay spikes [μs]	
	Mean	Mode	σ	lower	higher
Cross cable	36.6	38	1.67	30	39
100Mbps - PTP only	50.5	51	1.61	44	54
100Mbps - CPU-jam	55.6	55	2.39	44	62
100Mbps - FTP	50.8	60	5.72	-96	131
10 Mbps - PTP only	168.2	169	2.49	157	172

Table 2.1: summary of time offset measurements

Time offset after synchronization results from the superposition of two factors. The first is *Network-related Delay*, which accounts for asymmetries both in propagation time within the network and in timestamping latencies of transmitted and received packets. Switch effects further contribute to the offset, which increases with respect to cross-cable connection by about

14 μs with a 100Mb switch and by about 130 μs with a 10Mb switch.

Another factor is System Response which causes further increase in timestamping latency and asymmetry, due to the computational and IO activities in a node. Measurements showed how a job running in parallel increases the mode and standard deviation values, while the distribution is stretched out, as illustrated in figure 2.7.

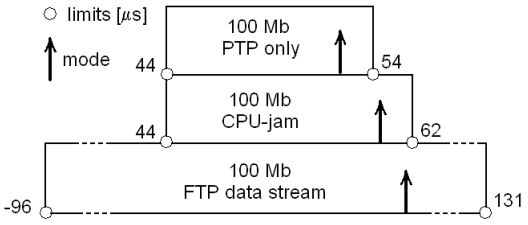

Figure 2.7: Trend of distributions in 'linear response phase'

Other important considerations concern the time the algorithm takes to synchronize from a starting time offset to within 100 μs, already called 'non-linear response phase'. Convergence time does not depend on the particular network setup but only on the initial offset. Table 2.1.5 shows some results for different connections with only PTPd running.

Network Connection	Starting Offset		
	500 ms	2 ms	0.2 ms
Cross Cable	$\sim$ 30 minutes	$\sim$ 2 minutes	$\sim$ 10 sec.
100 Mbps	$\sim$ 30 minutes	$\sim$ 2 minutes	$\sim$ 10 sec.
10 Mbps	$\sim$ 30 minutes	$\sim$ 2 minutes	-

Table 2.2: Convergence times in the 'non-linear response' phase.

These times are determined by a particular internal software parameter called $adjfreq\_max$. This parameter sets the limit for the allowed change of the software clock tick rate. Initially, the clock servo tends to specify a very large change, that exceeds this limit. Therefore a saturation effect occurs and the clock tick rate is adjusted by applying the maximum allowable change, as long as the offset comes close enough to the end value.

2.2 Further Generic Tests

In this section, further and more general purpose tests are presented using the set up proposed in 1.3.2. As first step an analysis of the timestamp mechanism is proposed. In fact, when nodes are synchronized they should execute the same operation at a certain time. To check this condition the same signal generator used in previously section[1] has been connected to an external input of both *Node 1* and *Node 2*. When the nodes receive the pulse they record a timestamp value, that represents a clock system measurement. Under the hypothesis that the difference in propagation delays from the signal source to the two node inputs is negligible, information about jitter and synchronization accuracy can be evaluated by comparing timestamp logs [9].

[1] providing an accurate (± 1 ppm) timing pulse

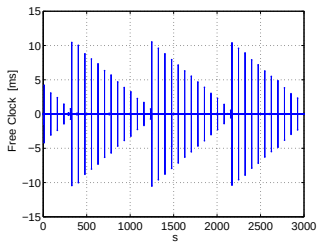

Figure 2.8: Differences between measured timestamp values and the reference time signal.

Also in this case, the timestamp code consists of a continuous loop reading the input pin state. A call is made to the timestamping routine when a change in the input state is detected and a timestamp value is hence collected and stored in a file.

The measurement system has been first used to analyze the timestamping variability due to software interrupt latencies. Different mechanisms contribute to the uncertainty associated to the timestamps, for instance processor scheduling time and interrupt latency. In order to contain as much as possible the effect of these error sources, the timestamping operation has been implemented by a kernel module. However, as can be seen from measurements reported in figure 2.8, there are still several timing spikes. These phenomena are caused by the presence of system latencies associated to tasks with different priorities and are generally observed when a task scheduler is active in the system [13].

It is clear from the plot that the software timestamp mechanism is occasionally affected by very large errors, which make observation of the clock features difficult. To prevent this, a thresholding operation is applied on data. Let $t(i)$ be the raw time value measured in correspondence of the ith pulse provided by the signal generator. The corrected value $t^\star(i)$ is obtained as:

$$t^\star(i) = \begin{cases} t(i) & \text{if: } \Delta t(i) < \tau_{TH} \\ t^\star(i-1) + \Delta T & \text{if: } \Delta t(i) \geq \tau_{TH} \end{cases}, \tag{2.1}$$

where $\Delta t(i) = |t(i) - t^\star(i-1)|$, ΔT is the nominal period of the reference time pulse provided by the signal generator and $t^\star(i-1)$ is the previous corrected timestamp value. τ_{TH} is the threshold value used to separate spikes from acceptable values.

The resulting clock increments deviation from the reference value ΔT, defined as: $t^\star(i) - t^\star(i-1)$, are presented in the histogram of figure 2.9(a). This shows the superposition of two effects: the timestamp jitter and the clock rate fluctuations. The latter account for the narrow peak in the middle part of the histogram and are the primary object of the analysis.

To better evidence this contribution, a normal probability plot of the same data is shown in Fig. 2.9(b). This evidences that, for probability levels between 1% and 99%, rate fluctuations can be considered Gaussian, with a mean of $-9.6\ \mu s$ and a standard deviation of $4.2\ \mu s$. This provides a characterization of single clock behavior. Since in this case the reference clock provides a timing pulse every $100\ ms$ the average clock drift is $-96\ \mu s/s$. Normal plots are a particularly effective tool for this kind of analysis and will be used also in the next sections to analyze synchronization.

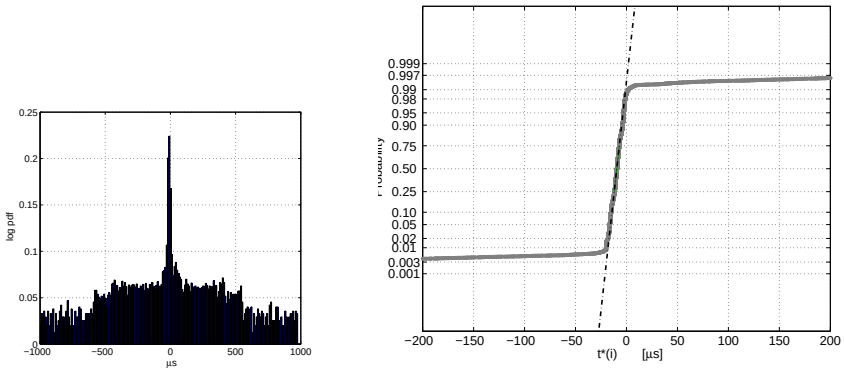

(a) (b)

Figure 2.9: 2.9(a): Histogram of clock increments - 2.9(b) Normal plot of clock increments

2.2.1 Synchronization analysis

Two different kinds of nodes have been considered in the tests. In the first case, *Node1* and *Node2* are the same PCs used in previously section (Pentium III 600MHz processor running a Linux 2.6 kernel), while in the second case two embedded systems are considered (Fox Board presented in 1.3.1 with 100MHz processor and a 'bare bones' Linux 2.6 kernel). The PTPd version [14] of the IEEE 1588 synchronization protocol is run on these nodes to have them properly synchronized.

The difference $d(i) = t_1(i) - t_2(i)$, where $t_1(i)$ and $t_2(i)$ are respectively the times measured by *Node1* and *Node2* in correspondence to the same event $e(i)$, gives the synchronization limits of the distributed system under analysis.

It should be remembered that ideally a phase synchronized system will provide identically null $d(i)$ values, while a frequency synchronized system can be allowed to have a constant offset. In this work we are mainly concerned with frequency synchronization.

Analysis with unloaded network

In the absence of cross-traffic, two main contributions concur to determine the total variability in $d(i)$ measurements, as illustrated in figure 2.10, where a histogram of $d(i)$ values has been reported. Uncertainties can be attributed to jitter in the timestamping mechanism and to the variability associated with the synchronization protocol. Therefore, it can be safely assumed that, while the synchronization protocol accuracy affects the central part of this distribution, spikes are generally associated with the timestamping mechanism, as previously noted. In the following we shall only consider the central part of the histograms since we are interested in synchronization effects.

Figure 2.11(a) plots the clock differences $d(i)$, over a time interval of 600 seconds, both for PC nodes and for embedded nodes.

It should be noticed that the reference clock provides a timing pulse every $500\ ms$. This is a higher rate than the default PTP value for SYNC packets and allows to sample the difference $d(i)$ with better resolution.

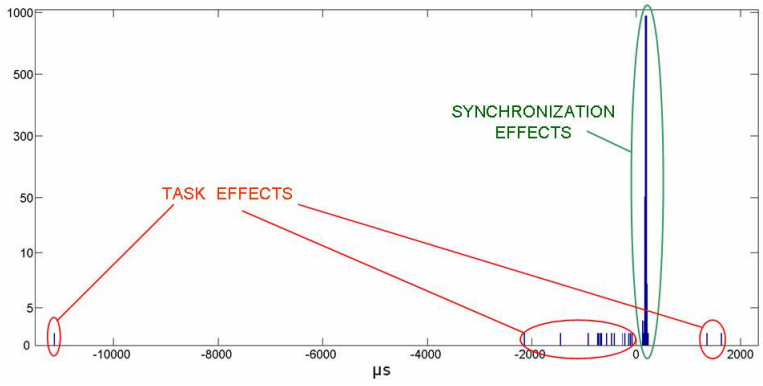

Figure 2.10: Contributions to the time measurements variability.

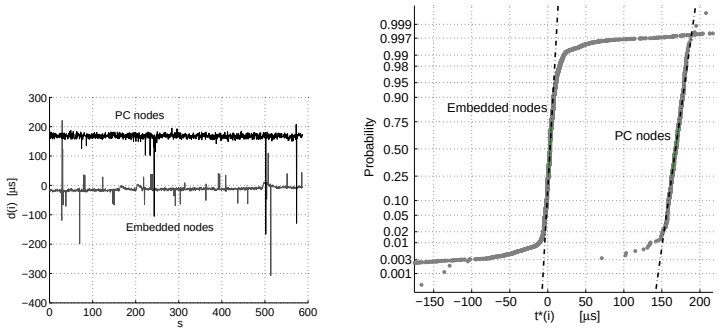

(a) (b)

Figure 2.11: Analysis done without cross-traffic. 2.11(a) Time behavior of the $d(i)$. Zoom on 10 minutes of measurement values - 2.11(b) Normal plot of $d(i)$ done on 3 hours of measurement values

Normal plots of $d(i)$ values are presented in figure 2.11(b) and evidence the differences between the two kinds of nodes. It can be seen that, for a probability level between 1% and 99%, a Gaussian distribution can be assumed for both cases. For embedded nodes the estimated mean offset is $3.1\ \mu s$ with a standard deviation of $4.4\ \mu s$, comparable with the standard deviation of the free clock. If PC nodes are considered, the mean and standard deviation of the offset between the two clocks are respectively equal to $168\ \mu s$ and $7.1\ \mu s$. It is important to recall that the accuracy of the reference clock period is about $\pm 0.5\ \mu s$.

Analysis with cross-traffic network load

These measurements aim to study the synchronization accuracy when cross-traffic is present. The results have been obtained with a cross-traffic generated with a packet generator time step $T = 1\ ms$, and for chaotic map parameters $d = 0.3$ and $m_1 = m_2 = 1.7$, which corresponds to a Hurst parameter equal to $H = 0.78$. This is a typical value for a communication network with a normal traffic load.

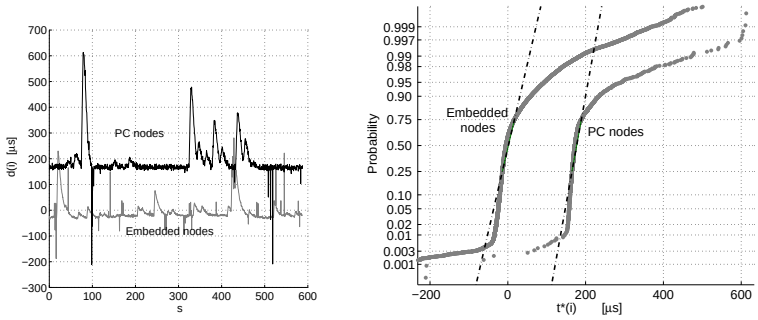

(a) (b)

Figure 2.12: Analysis done with cross-traffic. 2.12(a) Time behavior of the $d(i)$. Zoom on 10 minutes of measurement values- 2.12(b) Normal plot of $d(i)$ values for 3 hours of measurement values

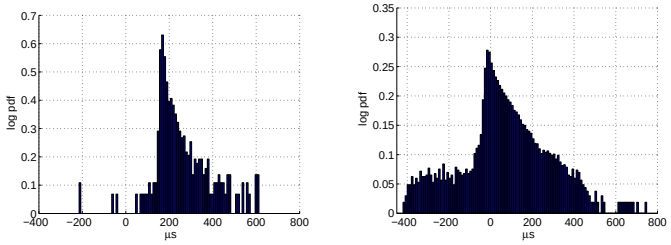

(a) (b)

Figure 2.13: Analysis done with cross-traffic. 2.13(a) Histogram of the $d(i)$ values obtained for PC nodes- 2.13(b) Histogram of the $d(i)$ values obtained for embedded nodes

By comparing figure 2.12(a) with figure 2.11(a) it can be noted that the variability in measurements of $d(i)$ is now mainly due to the presence of 'bursts'. These are presumably caused by large propagation delays due to packet retransmissions, that occur when PTP packets interfer with cross-traffic. The peak amplitude of these events may be correlated with the delays

introduced by the medium-access control policy implemented by the physical layer. The time duration instead depends on the impulse response of the PTP clock servo and on the clock drift correction mechanism. The latter effect can be noted by comparing the bursts obtained with the two different kinds of nodes: the shape is the same for a given system set-up, independently from the amplitude, while it changes if another system is taken into account.

In figure 2.12(b) the normal probability plots of $d(i)$ values have been reported. It can be noted that the two distributions are quite similar, as can be seen also in the histograms of figures 2.13(a) and 2.13(b). Both largely differ from a Gaussian model, this makes no sense to estimate the mean and standard deviation from the normal probability plot.

Part II

Calibration and Repeatability in EMC Tests

Introduction - Part II

Part II of the thesis, dealing with some specific problems related to uncertainty and repeatability in Electromagnetic Compatibility (EMC) Tests, is organized as follows. In Chapter 3, some considerations about magnetic field propagation within an anechoic chamber are reported. Simulation analysis and experiments have been performed for magnetic radiating circuits (magnetic loop). In Chapter 4 an accurate calibration of Line Impedance Stabilization Networks (LISN) is presented, focusing on the effects of parasitic parameters at the Equipment Under Test (EUT) port. Finally, in Chapter 5 the uncertainty contributions associated to the measurement for air electrostatic discharge (ESD) immunity tests are analyzed. The effects of different type A uncertainty contributions are compared and the ESD repeatability is assessed.

Electromagnetic compatibility (EMC) is the branch of electrical sciences which studies the unintentional generation, propagation and reception of electromagnetic energy with reference to the unwanted effects (Electromagnetic Interference, or EMI) that such energy may induce.

The effects of EMI are extremely variable in character and magnitude, ranging from simple annoyance to catastrophe. Some examples of the potential effects of EMI are:

- interference to television and radio reception,
- loss of data in digital systems or in transmission of data,
- delay in production of equipment exhibiting intra-unit, subsystem, or system-level EMI,
- malfunction of medical electronic equipment, automotive control, navigation equipment.

The goal of EMC is the correct operation, in the same electromagnetic environment, of different equipment which use electromagnetic phenomena, and the avoidance of any interference effects.

In order to achieve this, EMC pursues two different kinds of issues. *Emission* issues are related to the unwanted generation of electromagnetic energy, and to the countermeasures which should be taken in order to reduce such generation and to avoid the escape of any remaining energy into the external environment. Susceptibility or *immunity* issues, in contrast, refer to the correct operation of electrical equipment in the presence of unplanned electromagnetic disturbances.

Interference, or noise, mitigation and hence electromagnetic compatibility is achieved by addressing both emission and susceptibility issues, i.e., attenuating the sources of interference,

making the coupling path between source and victim less efficient, and making the potential victim systems less vulnerable.
In electromagnetic compatibility contexts measurement uncertainty estimation is a critical factor, since it plays an essential role in the decision on the conformity/nonconformity of a product to applicable standards. Furthermore, the subject of measurement uncertainty in EMC test is very complex because the equipment that is being tested was not designed specifically for the test (i.e. there is no 'EMC' connection port), the test method usually includes set-up factors that affect the measurement, the test equipment is often itself complex and includes several separated but interconnected components, and finally the variations between different test sites might compromise measurement reproducibility.

EMI/EMC Test Lab

EMI/EMC Laboratories test equipment can be configured to perform specific tests to investigate the limits of compliance in terms of electromagnetic interference and ensure that all the designed circuits meet the basic EMI standards in terms of electromagnetic emission and immunity. The generic standards [15] [16] list a series of phenomena which should be tested, like conducted and radiated emissions or ESD transient and surge immunity. Most product standards cover the same phenomena, although there may be exceptions and additions, so often it is not necessary for all of the phenomena to be tested at all stages.
EMC tests mainly concern two different specific types of tests: for pre-compliance or full compliance.

Pre-compliance. While a product is in development, the EMC effects of alternative design decisions and of remedial measures will need to be checked. Different layouts, different filters and different screening regimes need to be compared and this should be done as development progresses rather than at its conclusion, as otherwise a design which is ineffective in EMC terms may have excessive development resources spent on it. Therefore there is a need for a diagnostic test facility - which needs not be truly equivalent to the compliance test set-up - to be available throughout the development phase. Once a prototype is ready, this represents the model which will be subject to full compliance testing and it is advisable to carry out some preliminary tests to the same standards. This has several purposes:
- to avoid unpleasant surprises. If a product is clearly well outside the required limits, it is pointless submitting it to the compliance test before remedial work has brought it to a point at which there is a reasonable chance of success;
- to define the worst-case configuration and operating mode. For a complex product with many options, modes and configurations, the worst case to submit for full compliance may not be immediately obvious and finding it may take much longer than the test itself;
- to define the criteria for immunity test failure. It may not be clear until this point exactly what happens to the product when it is subjected to incoming transient or RF interference. It is the manufacturer's responsibility to define what actually constitutes a test failure in the immunity context.

Full compliance. A full compliance test set-up must be capable of carrying out all those

tests that the manufacturer intends to do in-house, to the required standard setup. The choice of which tests to do in-house and which at an external test house is affected by several factors, the most prominent being:
- the available budget, skills and resources
- the nature of the EUT(s)
- the requirements of the applicable standards

Set-up for EMC tests are reported in the product standards with many technical details. However, EMI measurements may significantly affect the parameter measured, resulting in error. For instance, the location of antennas may affect the calibration curve error also around 30 dB in undamped shielded-room measurements of radiated emissions. A measurement with an oscilloscope may corrupt the measured signal as a result of either the additional ground connection or by radiated pick up on the oscilloscope test leads. Moreover ground loop connections, cable route, attenuator mismatch, external environment conditions are some possible causes of inaccurate measure. The next chapters describe some of these critical measurement conditions.

EMC measurements could be influenced by different setup conditions such as table positioning [2] and table material [3], and conducted emissions could be influenced by factors such as length [4], height, and manner of main cable meandering [5] as well as positioning of the equipment under test [6].

Standards

The level of immunity into equipment depends on how critical the correct functioning of the equipment is and on the electromagnetic environment in which it is designed to operate. Many EMI requirements take the criticality and environment into account by classifying equipment and by imposing different susceptibility test levels in the different classes.
EMI can be considered a form of environmental pollution: in order to reduce the impact of this pollution, some control on the environmental level of conducted and radiated emissions of noise is necessary.
Many countries impose commercial regulations on the emission from data-processing equipment; industrial, scientific, and medical (ISM) equipment; vehicles; appliances; etc. The majority of military regulations and standards, and some commercial specifications, also require that equipment be demonstrated immune to susceptibility test levels.
Commercial requirements are typically confined to limits on conducted and radiated emissions. However, with the advent of European Union (EU) EMC Directive, mandatory and routine immunity (susceptibility) test requirements were imposed for the first time on commercial equipment. The EMC requirements encompass equipment from RF ac welders to electric drills, household equipment, and digital device.

Chapter 3

Field propagation in SA-Chamber

For test purposes emission are subdivided into radiated emissions from the system as a whole, and conducted emissions present on the interface and power cables. Conventionally, the break-point between radiated (high frequency) and conducted (low frequency) emissions is set at 30 MHz.
Radiated emission compliance testing should be done at an open area test site (OATS). The characteristics of a minimum standard OATS are defined in the standards [CISPR16] and [EN 55 022]. Such a site offers a controlled RF attenuation characteristic between the emitter and the measuring antenna (known as site attenuation). In order to avoid influencing the measurement there should be no objects that could reflect RF in the vicinity of the site. The CISPR site dimensions are shown in figure 3.1. The ellipse defines the area which must be flat and free of reflecting objects, including overhead wires. So, for good repeatability between different test sites, a substantially larger surrounding area free from reflecting objects is advisable.
It is however impossible to avoid ground reflections which are regularized by the use of a 'ground plane'. The minimum ground plane dimensions are also shown in figure 3.1. Close attention to the construction of the ground plane is necessary. It should preferably be solid metal sheets welded together, even if bonded wire mesh is often used.

In practice, radiated emission tests of electronic products are often performed in a semi-anechoic chamber (SAC). In a semi-anechoic chamber, electromagnetic field absorbers are

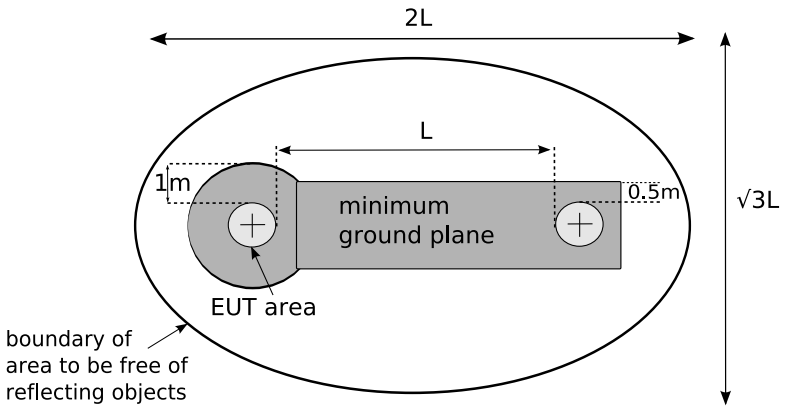

Figure 3.1: cispr-OATS

placed at the chamber walls and ceiling to avoid reflections of the radiated waves and echoes at the receiver input of the measurement apparatus. The only exception is for the ground plane, which must be a conducting metal plane, without absorbers.
In order to reduce the costs due to the expensive absorbing materials and the large dimensions of the chamber required by the standard, pre-compliance test sites are often realized and frequently used. In fact, the distance between EUT and receiving antenna determines the overall dimensions of the site and hence its cost. Three commonly specified distances are 3 m, 10 m and 30 m. Confidence checks can be carried out on a 3m range, on the assumption that levels measured at 10 m will be 10 dB lower (field strength should be proportional to 1/d). This assumption is not entirely valid at the lower end of the frequency range where 3m separation is approaching the near field.
Standards define the requirements for screened anechoic enclosures for emission measurement [17]. The major requirement is to establish that the site attenuation is not significantly affected by wall reflections. To this aim the concept of normalized site attenuation (NSA) is used to estimate the SAC response. NSA is defined in [ANSI C63.4] as the site attenuation divided by the antenna factors (AFs) of the radiating and receiving antennas (all in linear units). The standard requires NSA values within ± 4 dB from the theoretical NSA, and over the whole radiated emission frequency range 30 MHz to 1 GHz. Due to the fact that semi anechoic chambers usually do not satisfy the above recalled criteria in terms of NSA (especially in the lowest range of frequency), it is important to investigate the accuracy obtained from the measurements.
In the past, several scientific researches have studied the correlation between measurements performed in an ideal test site and measurements carried out in some non-compliant sites. In [19], Garn introduced the concept of 'chamber factors', through which the E field estimates obtained in a non-compliant site can be corrected in order to achieve values that can be used to directly verify the compliance of the product to the emission limits. The chamber factor was also introduced in [20] along with the concept of 'grey factor'. Despite its effectiveness, the use of correction factors has non-negligible practical drawbacks: it requires a complex handling of the general measurement results and, moreover, a number of preliminary reference measurements performed in an open area test site (OATS) are always needed.
In this chapter a number of simulation analysis and experiments are reported to evaluate the limits of radiated emission tests when performed within chambers that do not fulfil the NSA requirements. In fact, the repeatability of radiated emission tests and their uncertainty is directly related to the radiating circuits present inside the EUT and even to the external coverage type and dimensions.

3.1 Chamber Factors

The characterization of a test enclosure in terms of chamber factors requires several measurements at different test configurations, i.e. for different transmit antennae (dipole or loop), antenna positions and polarizations. For each configuration, the correction factor can be determined as follows:

$$C_F[dB] = E_{REF}[dB\mu V/m] - E_{ENC}[dB\mu V/m] \tag{3.1}$$

where C_F is the correction factor, E_{REF} is the field strength measured at the reference site, and E_{ENC} is the field strength measured in the enclosure, i.e. the semi-anechoic chamber. The reference site is a good OATS, i.e. having only very small deviations from the ideal values of NSA. A dipole and a loop antenna are used as transmit antennae to provide fields with different wave impedance. A biconical antenna is used as a receive antenna. When plotted in a graph, the values of C_F typically appear with a superimposed spread. The upper envelope curve obtained is the worst-case chamber factor, while the mean between the upper and lower curve is the mean chamber factor. The spread of the correction factors is the grey factor.
Determined chamber factors can be used to adjust the field strength estimates obtained in radiated emission tests of the EUT. In particular, the chamber factors (in dB) are to be added to the field strength estimates (in dBμV/m) measured in the semi-anechoic chamber in order to obtain the open-site equivalent values (in dBμV/m).
Chamber factors are functions of frequency and polarization, and depend on EUT physical features, such as dimensions and radiating circuit type (loop or dipole-like). Indeed, the absorbers used in the chamber have properties that depend on the wave impedance, which is constant in the far field region, and may vary considerably in the near field one. On the other hand, the extension of near and far field regions is strongly related to the wave frequency and EUT dimensions. Approximately, the near field region includes the points whose distance from the EUT is lower than λ, while the far field region includes the points located far away from the EUT, by more than $2D^2/\lambda$, D being the largest dimension of the EUT. Therefore, upon varying the frequency and D, the properties of the absorbers may considerably change, and, consequently, the chamber response too.
In a pre-compliance analysis of radiated emissions, measurement of the chamber response as a function of the frequency and EUT dimensions is very essential. To this aim, [18] requires the application of the so-called 'volume method', which consists of measurements to be performed with the transmit antenna placed at different locations within the volume that a EUT may occupy. A limit of this method is that it does not consider the real effects of the EUT emissions, hence the effects of its possibly large dimensions, i.e. the parameter D. This fact could even lead to relevant inaccuracy in the estimate of radiated emissions.

3.2 Characterization of the Investigated Test Site

A first set of preliminary experiments has been performed with the aim of characterizing a semi-anechoic chamber of size 7.94 m (L) x 3.74 m (W) x 3.34 m (H). For a good characterization of this site, three specific investigations have been conducted. The first step consists of computing the difference of site attenuation with respect to the theoretical reference (NSA). The second one is related to obtaining the chamber factors as described in the previous section. Finally a comparison between the SAC and a self made OATS is presented.

3.2.1 NSA Characterization

NSA has been measured according to the approach defined in [18], in the frequency range 30 MHz to 1 GHz and with variable step size (1 MHz for 30-100 MHz, 5 MHz for 100-500 MHz, and 10 MHz for 500-1000 MHz). In particular, a couple of biconical and log periodic antennas, one transmit and another receive, have been used in the range 30 - 200 MHz and 200 - 1000 MHz, respectively. The antennas have been positioned in the chamber according to the volume method and with the transmit antenna located within a cylindrical test volume of 2 m diameter. For each considered frequency and transmit antenna position, a number of measurements have been repeated for the two polarizations. The worst-case values obtained are summarized in figure 3.2(a), where the difference (in dB) between the measured and reference NSA is plotted versus frequency. The plot clearly shows that the employed chamber does not satisfy the above recalled ± 4 dB requirement. In particular, the highest differences are observed in the range 30 - 200 MHz.

3.2.2 CF Characterization

Chamber factors have been determined as described in (3.1). In particular, E_{ENC} has been assessed in the semi-anechoic chamber under test, while E_{REF} has been evaluated in the open field site of Seibersdorf at the Austrian Research Centre. A calibrated reference radiator (RefRad [1]) has been used to generate the signal. Three antennas have been then connected: a dipole of 65 cm length and a square loop of 30 cm side length, in the range 30 - 200 MHz, and a dipole of 20 cm length, in the range 200 - 1000 MHz. The measurement of field strength has been carried out by using a biconical antenna in the range 30 - 200 MHz, and a log periodic antenna in the range 200 - 1000 MHz. For measurements in the semi-anechoic chamber the receive antenna has been moved at a scan range of 1 to 2 m above the floor and with a measurement distance of 3 m. For each considered frequency, transmit antenna type and position, a number of measurements have been repeated for the two polarizations. The magnitude of worst-case values obtained are summarized in figure 3.2(b), where the chamber factors are plotted for both horizontal and vertical polarization. The plot shows once again the limits of the chamber response, for which significant correction factors are needed.

3.2.3 OATS Characterization

Further NSA measurements have been conducted in an OATS reference site. The self-made OATS consisted of a 6 m x 7 m conducting ground plane, positioned over a flat concrete ground plane free of obstacles. A picture of this OATS is shown in figure 3.3(a). The conducting ground plane has been realized by using two metallic layers, each consisting of 30 cm width aluminium[2] stripes placed side by side with overlaps of about 3 cm. The stripes have been

[1] RefRad is a battery operated combo generator for producing a well defined field strength in the frequency range of 1 MHz to 1 GHz.

[2] thin aluminium cooking sheets

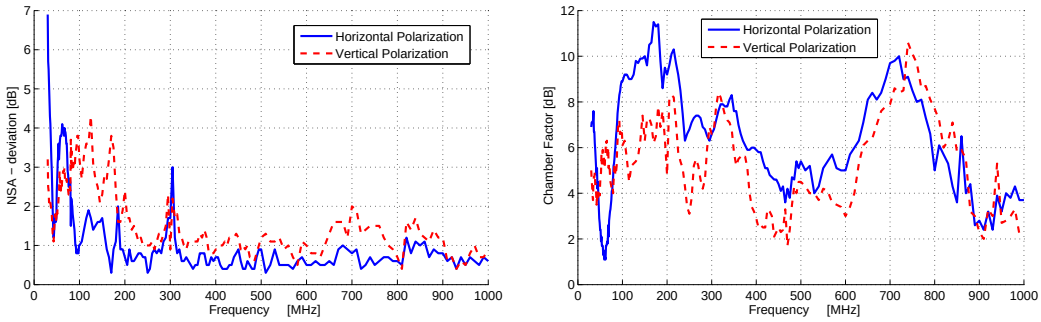

(a) (b)

Figure 3.2: Estimated values versus frequency: (a) NSA - (b) Chamber Factor

positioned orthogonally in the two layers in order to emulate as well as possible the properties of an ideal ground plane. From a set of measurements, NSA has been measured and found to be in good agreement with the theoretical values, over the whole frequency range 30 MHz - 1 GHz.

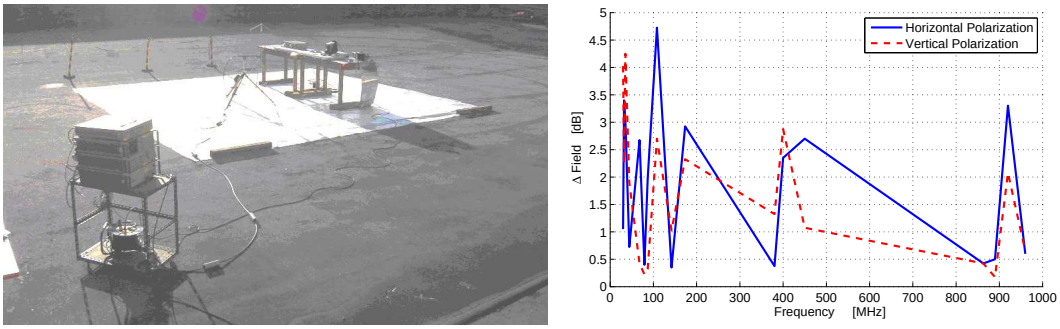

(a) (b)

Figure 3.3: (a) The employed OATS - (b) Difference between field estimates in the OATS and in the chamber.

NSA results of the anechoic chamber have been compared with the same measurements performed in the OATS. The mean values obtained, in terms of field deviations between OATS and chamber estimates, Δ_{FIELD}, are summarized in figure 3.3(b). As can be seen, the obtained Δ_{FIELD} is always lower than 3 dB, with the exception of the following cases: horizontal polarization and frequencies 108.2 MHz and 920 MHz, for which Δ_{FIELD} = 4.7 and 3.3 dB, respectively.

3.3 Considerations about Radiated Emission Test in Anechoic Chambers

As mentioned above, the behaviour of the absorbers in the chamber depends on the wave impedance Z_W [20], which is constant in the far field region, and may vary considerably in the near field one. Electric sources generate high-impedance fields in the near-field, while

magnetic sources generate low impedance fields in the near-field. Actual EUT will typically contain both types of radiating sources. At low frequencies, the anechoic material on the walls and ceiling can be located in the near-field of the EUT in small chambers. Therefore the absorber effectiveness may be affected, depending on the EUT nature (electric or magnetic source of noise) and dimensions (larger EUTs are giving smaller distance between the EUT and anechoic material).
Secondly, in the case of large equipment, the EUT radiating structure may couple with the walls and ceiling of the chamber. This can produce modifications in the EUT radiating properties, compared to the radiation obtained in an OATS, where no walls and ceiling are present. Both effects can lead to inaccuracy in the radiated emission measurements.
These situations are only partially taken into account with the NSA parameter of the anechoic chamber. NSA measurements are performed using 'electrical' antennas to generate the field: the anechoic material (near the transmitting antenna) can be affected only by wave impedance values higher than Z_0. Moreover, the 'volume method' considers the behaviour of the chamber when the source of noise is at the edge of the volume, but no information is given concerning the problems of real equipment that may have physical dimensions significantly larger than the used transmitting antenna.
For these reasons, the deviation of the normalized site attenuation from the theoretical value is suitable to describe the situation of EUTs radiating in the near field with high values of Z_W (electric field), with physical dimensions similar to the antenna used for NSA measurements.

3.4 Simulation Analysis

The EUT nature is modelled here by the presence of internal circuits that can be described, in terms of field radiation, as electric dipoles or magnetic loops. In particular, Z_W will assume values lower or higher than Z_0 = 120 π, i.e. the wave impedance in the far field region, and proportional or inversely proportional to the distance d between the interested point and the EUT, depending on the dominating source of field, i.e. loop or dipole, respectively.
Theoretical analysis and specific simulations to estimate the radiation of a magnetic field (using a loop antenna) are now reported. A convenient geometrical arrangement for the field analysis of a loop antenna is to position the antenna symmetrically on the x-y plane, at z=0, as shown in figure 3.4(a) [21]. With the assumption of constant current distribution (I_0) in a thin wire, the generic equations for magnetic field propagation are equations (2) reported below, where a is the radius of the loop antenna in meters, r the distance from the center of the loop in meters, and $k^2 = \omega^2\mu\epsilon \approx 2\pi/\lambda$.

$$
\begin{aligned}
H_r &= j\frac{ka^2 I_0 \cos\theta}{2r^2}\left[1+\frac{1}{jkr}\right]e^{-jkr} \\
H_\theta &= -\frac{(ka)^2 I_0 \sin\theta}{4r}\left[1+\frac{1}{jkr}-\frac{1}{(kr)^2}\right]e^{-jkr} \\
H_\phi &= 0
\end{aligned}
\tag{3.2}
$$

It is possible to simplify these equations in the assumptions of near field when $kr \ll 1$ or far field when $kr \gg 1$. In the frequency range investigated (30-200MHz) kr is equal to 1.8 and 12.6 respectively for 30 MHz and 200 MHz. So approximations for near or far field are not applicable. However, since the classical NSA formulation is based on the assumption of far field, preliminary tests are performed in this simpler case.

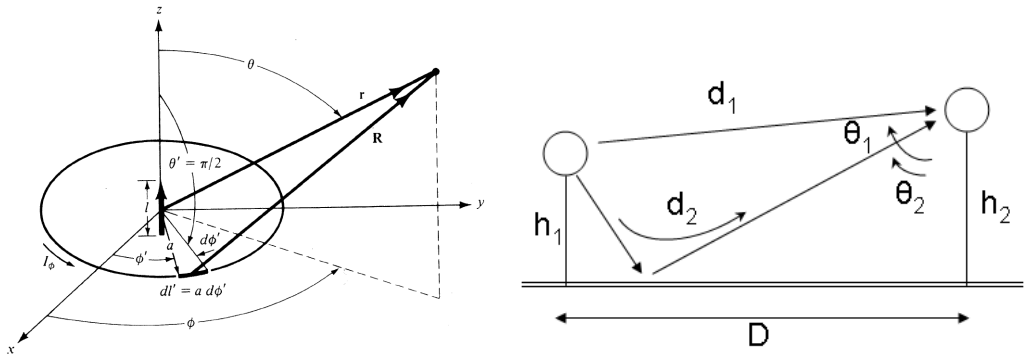

(a) (b)

Figure 3.4: (a) Geometry for circular loop - (b) Propagation geometry for loop antenna

3.4.1 Far Field Approximation

Classical NSA formulation is based on the far field assumption where $kr \gg 1$ [22]. In this case equations (3.2) become:

$$\begin{aligned} H_\theta &\approx \frac{-(ak)^2 I_0 e^{-jkr}}{4r} \sin\theta \\ H_r &= H_\phi = 0 \end{aligned} \tag{3.3}$$

Referring to figure 3.4(b), h_1 and h_2 are the heights of the transmitting and receiving antennas, D the separation distance, $d_1 = \sqrt{D^2 + (h_1 - h_2)^2}$ is the length of the direct ray, $d_2 = \sqrt{D^2 + (h_1 + h_2)^2}$ the length of the reflected ray, and finally $\theta_1 = \arcsin(D/d_1)$ and $\theta_2 = \arcsin(D/d_2)$. it is possible to obtain the following equation:

$$\begin{aligned} H_1 &= H_\theta(r = d_1) \\ &= \frac{-(ak)^2 I_0}{4} \cdot \left(\frac{1}{d_1} e^{-jkd_1}\right) \frac{D}{d_1} \\ H_2 &= H_\theta(r = d_2, \underbrace{\rho_R,\ \phi_R}_{reflected}) \\ &= \frac{-(ak)^2 I_0}{4} \cdot \left(\frac{|\rho_G| e^{-jkd_2} e^{j\phi_G}}{d_2}\right) \frac{D}{d_2} \end{aligned} \tag{3.4}$$

where ρ_G is the reflection coefficient of the ground plane, ϕ_G is the reflection coefficient

phase angle; in case of total reflection without phase displacement: $\rho = 1$ and $\phi = 0$. The total field is the algebraic sum of H_1 and H_2 and final equation is:

$$H_{TOT} = \frac{-(ak)^2}{4} I_0 D \cdot \left(\frac{e^{-jkd_1}}{d_1^2} + \frac{|\rho_G| e^{-j(kd_2 - \phi_G)}}{d_2^2} \right) \tag{3.5}$$

The magnitude of (3.5) is:

$$|H_{TOT}| = \frac{-(ak)^2}{4} I_0 D \cdot \frac{\sqrt{d_2^4 + d_1^4 |\rho_G| + 2(d_1 d_2)^2 |\rho_G| \cos(\phi_G - k(d_2 - d_1))}}{(d_1 d_2)^2} \tag{3.6}$$

The electrical size of loop (circumference) determines the efficiency of the loop antenna [21]. Loop antennas are usually classified as either electrically small or electrically large based on the loop circumference (C). An electrically small loop circumference is less than $\lambda/10$, while for an electrically large loop the circumference is $\approx \lambda/10$. For convenience we define $K = C/\lambda$

To maintain a good 'match' between the circumference of the loop and its working frequency range, three different antenna radii have been used: a_1= 16 cm for the frequency range 30 MHz to 80 MHz, a_2= 6 cm for the frequency range 80 MHz to 140 MHz and a_3= 3.4 cm for the frequency range 140 MHz to 200 MHz. Such solutions are shown in table 3.1 where the values of K are reported for each antenna in the respective frequency range.

Radius [cm]	f_{min} [MHz]	f_{MAX} [MHz]	K_{min}	K_{MAX}
16	30	80	0.1	0.27
6	80	140	0.1	0.18
3.4	140	200	0.1	0.14

Table 3.1: Loop Diameters

The effects of the variation in radiation patterns with respect to the value K are reported in figure 3.5. Pictures show the radiation patterns for the best case with $C = 0.1\lambda$ (K=0.1), assuming a uniform current distribution and for K=0.27. These patterns indicate that the field radiated by the loop along its axis (θ=0°) is zero. The shape of the propagation is similar in both cases. Unfortunately this propagation pattern regards the far field case and near field effects are not accounted for. In the latter case, multiple lobes should appear.

Using equation (3.6), predictions of H field radiation with $I_0 = 500\mu A$, $D = 3m$, $h_1 = h_2 = 1m$, are shown in figure 3.6 for the three loops.

3.4.2 Validation of the model

To evaluate the accuracy of the predictions obtained with the simplified equations and also to preliminarily investigate the effect of a magnetic field source, the loop antennas previously described are then used as transmitting devices in their respective working frequency ranges (D = 3 m, h1 = h2 = 1 m). The measurement of the field strength has been carried out by using a calibrated biconical antenna, so electric field is obtained using the antenna factors. With

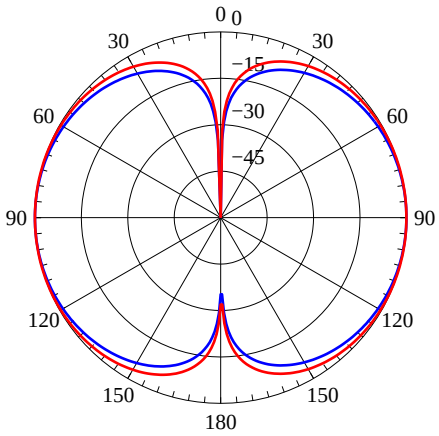

Figure 3.5: Elevation plane normalized amplitude pattern [dB] C=0.1 λ (blue) and C=0.27 λ (red)

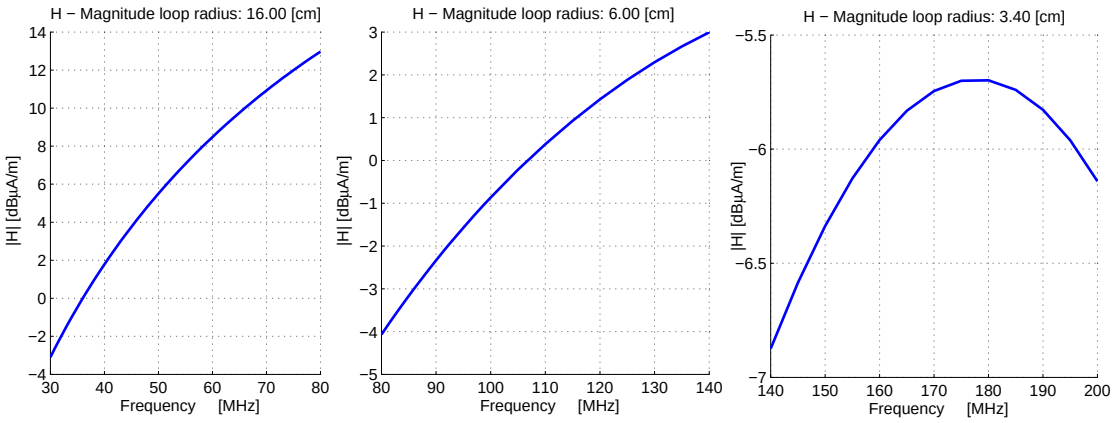

Figure 3.6: Loop antenna: H-Magnitude predictions.

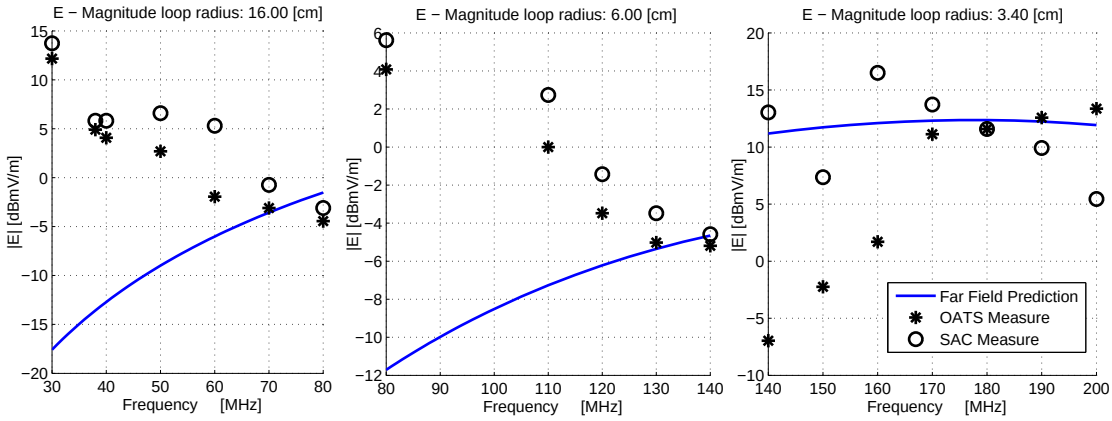

Figure 3.7: Loop antenna: Measurement results.

respect to the predictions, the relation is $E = \eta \cdot H$ [3]. The second step consists in repeating the measurements with the same set-up within the anechoic chamber. The tests are finally compared with the theoretical propagation formula. Results are presented in figure 3.7 in terms of equivalent electric field (continuous line = field prediction, star dots = OATS measurements, circle dots = SAC measurements).

OATS and SAC behaviour is similar, with some overestimation in the SAC measurements (for cases a_1 and a_2). All trends are closer to the field prediction only at higher frequencies, while in the lower frequency range the measured field values are very high compared to the theoretical ones.

These preliminary results highlight the need to study the matter in greater depth to understand the gap between the theoretical predictions and experimental measurements. Some remarks can be made. For instance, the radius of an antenna plays a key role in the ideal condition and hypothesis, like the constant current in the loop. Moreover, the theoretical radiated field has been calculated by adopting the same hypothesis made for NSA prediction, i.e. the near field contribution has been neglected and only far field radiation considered. Finally, a practical limit related to current measurement has played a large role specially in the range 140 - 200 MHz. In this range, in fact, the current clamp used for measurement presents some problems due to the size of the ring around the transmitting cable.

3.4.3 Full Analysis

To better investigate these aspects, the full equations of field propagation, reported in (3.2), are considered. In this case, to analyze the performances of the antennas near the ground plane, image theory is used. It is based on the imaginary sources combined with the real one. The equivalent system gives the same radiated field on and above the conductor as the actual system itself.

In receiving mode the center of the loop is considered. In this point the H-field strength is calculated from (3.2) and we suppose that this value is constant in the area of the loop. So we eventually have that, transmitting a sinusoidal waveform, the received signal is

[3] In far field conditions, the wave impedance is $\eta = 377\Omega$

$$V_{oc} = \frac{d}{dt}\left[\pi a^2 \mu_0 H sin(\omega t)\right] = \pi a^2 \mu_0 H \omega cos(\omega t) \tag{3.7}$$

where a is once again the radius of transmitting loop and $\mu_0 = 4\pi \cdot 10^{-7}\ [H/m]$ the magnetic permeability in vacuum. In fasorial form the equation becomes:

$$V_{oc} = j\omega\pi a^2 \mu_0 H$$

.

Furthermore the angle of the incident field on the receiving antenna has to be considered. As seen in Figure 3.8 three orientations have been selected for the loops and each one gives different patterns and angles of incidence for direct and reflected waves.

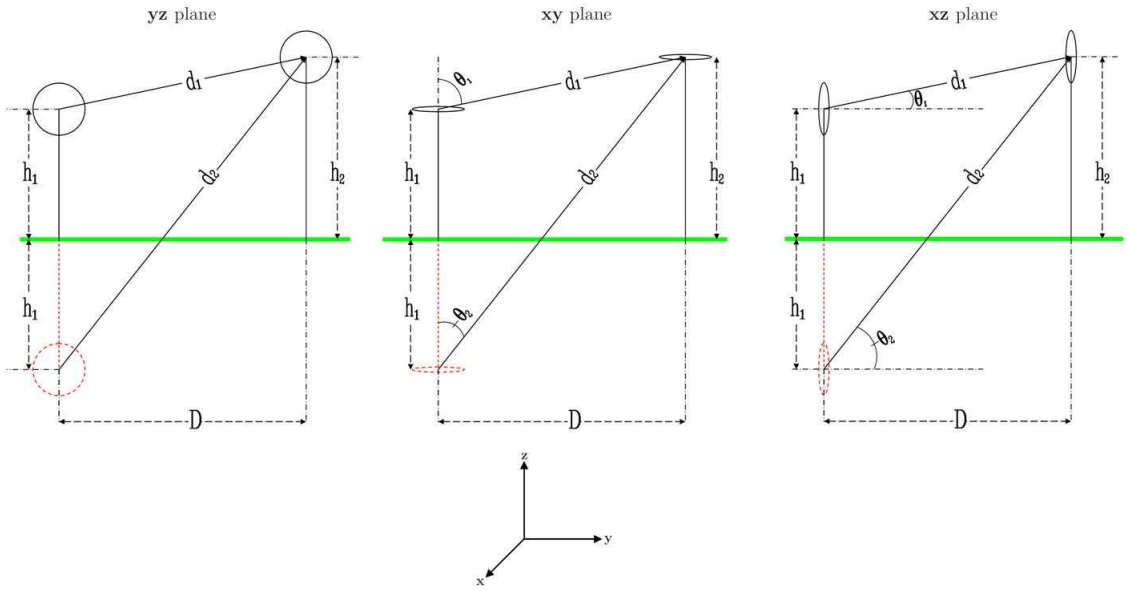

Figure 3.8: Transmitting and receiving positions

Since (3.2) give the H-field in polar coordinates, and we need to know the strength of the orthogonal component along the $\hat{\mathbf{a}}_\mathbf{z}$ versor (see Fig. 3.4(a)), the following transformation rules are required.

$$\left\{ \begin{array}{l} \hat{\mathbf{a}}_\mathbf{x} = \hat{\mathbf{a}}_\mathbf{r} sin\theta cos\phi + \hat{\mathbf{a}}_\theta cos\theta cos\phi - \hat{\mathbf{a}}_\phi sin\phi \\ \hat{\mathbf{a}}_\mathbf{y} = \hat{\mathbf{a}}_\mathbf{r} sin\theta sin\phi + \hat{\mathbf{a}}_\theta cos\theta sin\phi + \hat{\mathbf{a}}_\phi cos\phi \\ \hat{\mathbf{a}}_\mathbf{z} = \hat{\mathbf{a}}_\mathbf{r} cos\theta - \hat{\mathbf{a}}_\theta sin\theta \end{array} \right\}. \tag{3.8}$$

Since the ground plane is assumed to be a perfect conductor, its reflection coefficient should be $|\rho| \approx 1$ and so the principle of images can used. This principle is applied to an electromagnetic field source radiating nearby a perfect conductor: in this case the radiated field can be thought of as the field generated by the source in a free space plus the field produced by an *image radiator* placed in an appropriate point of the conductor. The position of this image radiator has to be calculated so that $E_{SItan} = -E_{SRtan}$, where E_{SRtan} is the tangential electric field on the conductor surface due to the real source and E_{SItan} is the tangential electric field on the conductor surface due to the image source. When the conductor is a plane this

electromagnetic problem is solved very easily. Indeed the images of loop antennas are simply the same antennas placed symmetrically in underground as shown in figure 3.9. The distances

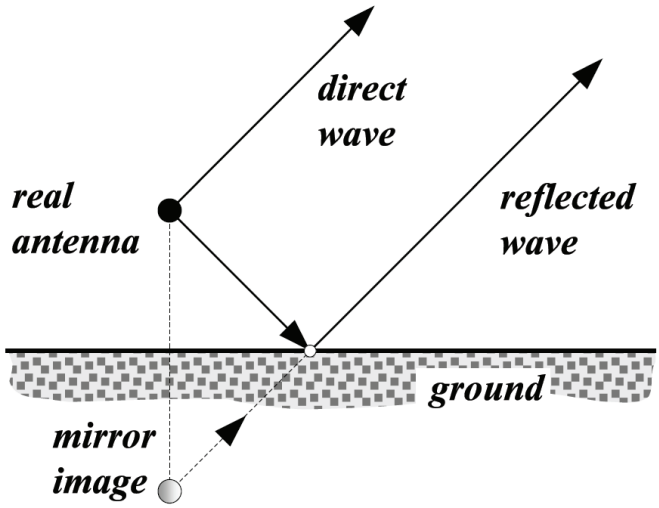

Figure 3.9: Images principle

between the receiving antenna and the sources can be calculated as $d_1 = \sqrt{D^2 + (h_1 - h_2)^2}$, $d_2 = \sqrt{D^2 + (h_1 + h_2)^2}$ and then used to find θ_1 and θ_2 angles shown in figure 3.8:

Plane (Y-Z) In this case the position is not relevant, indeed $\theta_1 = \theta_2 = \pi/2 \Rightarrow sin\theta = 1$, $cos\theta = 0$. This means that, according to 3.8, all the component along the $\hat{a}_z$ versor is due to the component along $\hat{\theta}$. Therefore $H1_r = H2_r = 0$.

Plane (X-Y) Using the sin-theorem[4] and solving the triangles $D - d_1 - (h_2 - h_1)$ and $D - d_2 - (h_2 + h_1)$ we obtain: $\theta_1 = \arcsin(D/d_1)$ e $\theta_2 = \arcsin(D/d_2)$. It's very important to note that in this situation the virtual current in the mirror image flows in the opposite verse with respect to the real one. Therefore being i the current in the real loop, the current in $H2_r$ and $H2_\theta$ is inverted: $I_0 = -I$ (see also A);

Plane (X-Z) Using the sin-theorem and solving the triangles $D - d_1 - (h_2 - h_1)$ and $D - d_2 - (h_2 + h_1)$ we obtain: $\theta_1 = \arcsin \frac{(h_2 - h_1)}{d_1}$ e $\theta_2 = \arcsin \frac{(h_2 + h_1)}{d_2}$;

Used in (3.2), these distances and angles gives us the polar components of the H-field which can be transformed into orthogonal components using (3.8).

$$H1_r = j \frac{ka^2 I_0 \cos\theta_1}{2d_1^2} \left[1 + \frac{1}{jkd_1}\right] e^{-jkd_1} \tag{3.9}$$

$$H2_r = j \frac{ka^2 I_0 \cos\theta_2}{2d_2^2} \left[1 + \frac{1}{jkd_2}\right] e^{-jkd_2} \tag{3.10}$$

[4]the sin-theorem states that, given a triangle with a, b, c sides and α, β, γ the angles respectively in front of the sides, stands the following equality: $\frac{a}{\sin\alpha} = \frac{b}{\sin\beta} = \frac{c}{\sin\gamma}$

$$H1_\theta = -\frac{(ka)^2 I_0 \sin\theta_1}{4d_1}\left[1 + \frac{1}{jkd_1} - \frac{1}{(kd_1)^2}\right] e^{-jkd_1} \tag{3.11}$$

$$H2_\theta = -\frac{(ka)^2 I_0 \sin\theta_2}{4d_2}\left[1 + \frac{1}{jkd_2} - \frac{1}{(kd_2)^2}\right] e^{-jkd_2} \tag{3.12}$$

$$\begin{aligned} H1_z &= H1_r cos\theta - H1_\theta sin\theta \\ H2_z &= H2_r cos\theta - H2_\theta sin\theta \\ |H_{tot}| &= |H1_z + H2_z| \end{aligned} \tag{3.13}$$

Thanks to these equations, it's possible to calculate the H-field in every point of the space just knowing the current flowing in the transmitting loop.

3.5 Experimental Results

In this part of the work transmitting and receiving antennas have been built and the results, as will be shown, are very satisfactory and their behavior is very close to the theoretical predictions. To scan the frequency range and keep the ratio $C = \lambda/10$, three couples of antennas have been made. Besides, to avoid interferences with FM broadcasting, no frequency beyond 88 MHz has been considered, so the choice led to 36 MHz, 60 MHz and 85 MHz. Since we consider the free space speed of light, corresponding wavelengths are $\lambda_i = c_0/f_i$ = 8.3 , 5 and 3.53 meters. Consequently the radii were respectively 0.133 , 0.0796 and 0.0562 meters.
A number of experiments have been performed in order to evaluate the critical points already mentioned by comparing the theoretical propagation formulas with the measurements performed both in a semi-anechoic chamber and on an OATS. In particular the effect of a magnetic field source are analyzed using the loop antennas both for transmission and receive.

3.5.1 Equivalent Circuit

As seen in (3.2) the current flowing in the transmitting loop must be known to calculate the radiated field. The easiest way to get this information is by a current probe (already used in the previously measurement - figure 3.7). Current probes use the Hall effect to sense the magnetic field around a wire produced by the electric current flowing through the wire, without any need to cut or interrupt the wire. Then they generate a voltage-controlled output proportional to the current intensity with a specified ratio [mV/A]. However using such a probe there was significant interference and the probe seemed not to act linearly. So a more theoretical approach to get the current intensity has been followed using a vector network analyzer (VNA).
In transmission mode these small loops are primarily inductive. The equivalent circuit for the input impedance is shown in figure 3.10(a). Therefore the input impedance Z_{IN} is represented by:

$$Z_{IN} = R_{IN} + j \cdot X_{IN} \tag{3.14}$$

where R_{IN} represents the radiation and loss resistance of the loop conductor, while X_{IN} summarizes the external inductive and internal high-frequency reactances. In figure 3.10(a) the capacitor C_r is used in parallel to Z_{IN} described in (3.14). At resonance, the capacitor C_r must be chosen to cancel the imaginary part of (3.14). To this aim, characteristic impedances

Z_{IN} are measured by the Network Analyzer and the capacitors were positioned for each transmitting antennas. Information about the transmitting current I_0 can be obtained by:

$$I_0 = V_G \cdot \frac{Z'_{IN}}{Z_G + Z'_{IN}} \cdot \frac{1}{Z'_{IN}} \tag{3.15}$$

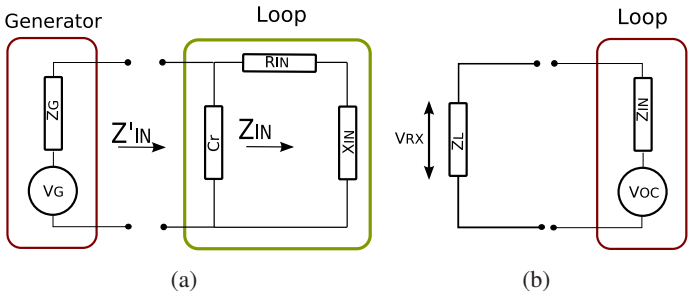

Figure 3.10: Equivalent circuit of loop antenna: (a), in transmitting mode (b) in receiving mode

In receiving mode, when a plane wave impinges upon the loop an open-circuit voltage develops across its terminals. This voltage is proportional to the incident magnetic flux as seen in (3.7). When a load impedance Z_L is connected to the output terminals of the loop as shown in figure 3.10(b), the voltage V_{RX} across the load impedance is related to the input impedance Z_{IN} of the antenna by $V_{RX} = V_{OC}\frac{Z_L}{Z_{IN}+Z_L}$.

Consequently, the H-field can be calculated from the measured voltage V_L on the 50Ω input resistance of the spectrum analyzer as [21]:

$$|H_{rx}| = |V_L|\frac{Z_{IN}+50}{50}\frac{1}{\omega\pi a^2\mu_0}$$

3.5.2 Realization and Calibration

As already discussed, a loop antenna was also used to generate the electromagnetic field. The construction is very simple, fixing the inner part of a 50 Ω coaxial cable upon a cardboard and forming a circle of different radius, according to the frequencies used as shown in figure 3.11. To analyze the the impedance of the loop, an Agilent 4396B vector network analyzer (VNA) has been used. The impedances for each frequency are reported in table 3.5.2.

$f_0[MHz]$	Z [Ω]
36	$0.065 + i240.16$
60	$0.970 + i220.22$
85	$0.062 + i207.15$

Table 3.2: Transmitting loop impedances before applying the capacitor

It is easy to see that the impedance is almost only imaginary, and in particular reactive ($\Im(Z) > 0$). So, an appropriate capacitor has been applied to each antenna in order to balance the imaginary part of its impedance. The result is not perfect, because of some approximations,

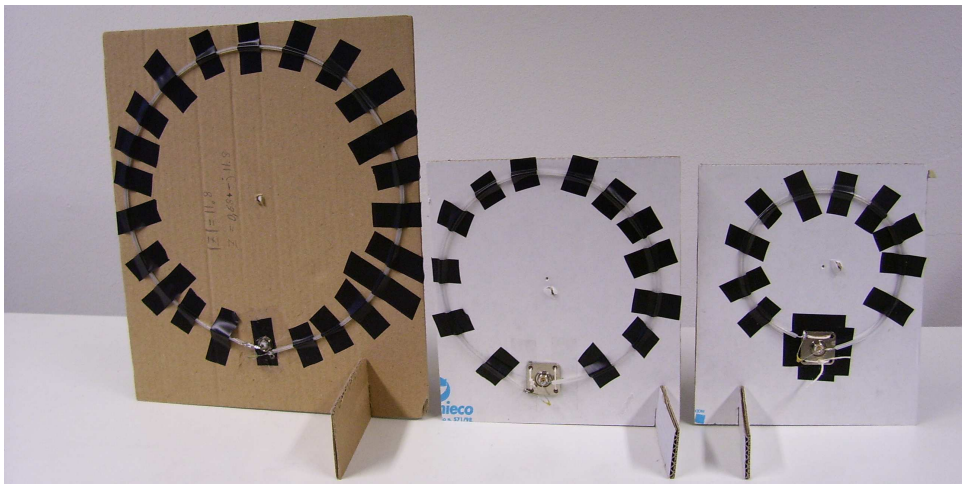

Figure 3.11: Transmitting loops

especially in the capacitors choice. Anyway the imaginary part became very small. In figures 3.12, 3.13 and 3.14 screenshots taken from the network analyzer are presented. For each antenna, a 2 MHz span around the working frequency has been considered and the marker shows the exact value in the middle. Real part is practically the same, while the imaginary part is now contained between $\pm 8\ \Omega$.

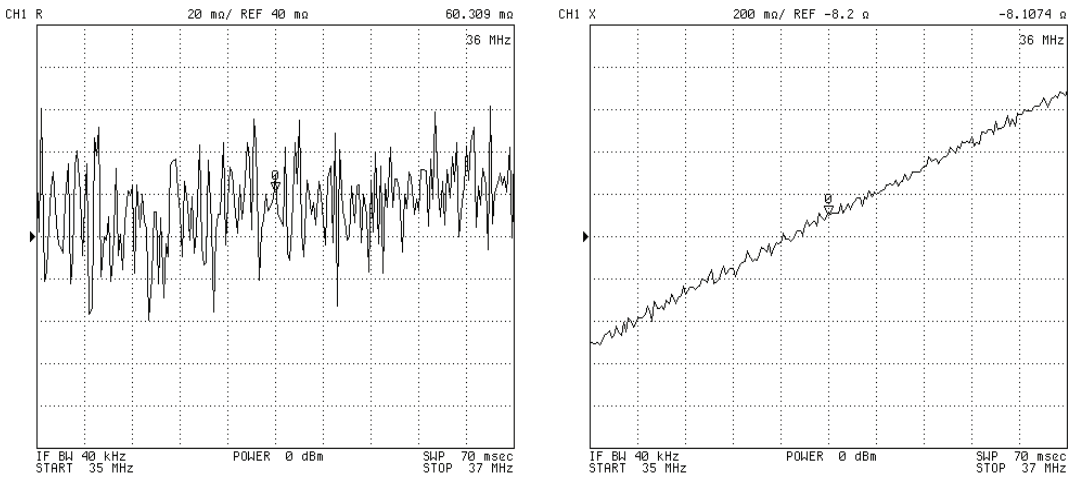

Figure 3.12: 36 MHz loop impedance after the capacitor was applied

Transmitting loops are simple wires turned into a circle and they generate an electromagnetic field. However the goal is to measure only its magnetic component so receiver loops also need a shield. The receiving loops were created starting from a copper pipe with a diameter of 10 millimeters. As its conductivity is very high ($59.6 \cdot 10^6$ S/m) it has been used as an E-field shield and inside it a wire taken from the inner part of a 50 Ω coaxial cable was placed. The copper has been bended into a circle and soldered to a support. The connector used is a BNC type. A picture of the realized antennas is reported in figure 3.15.

The external shield needs to be grounded, i.e. it has to be directly linked to a null voltage

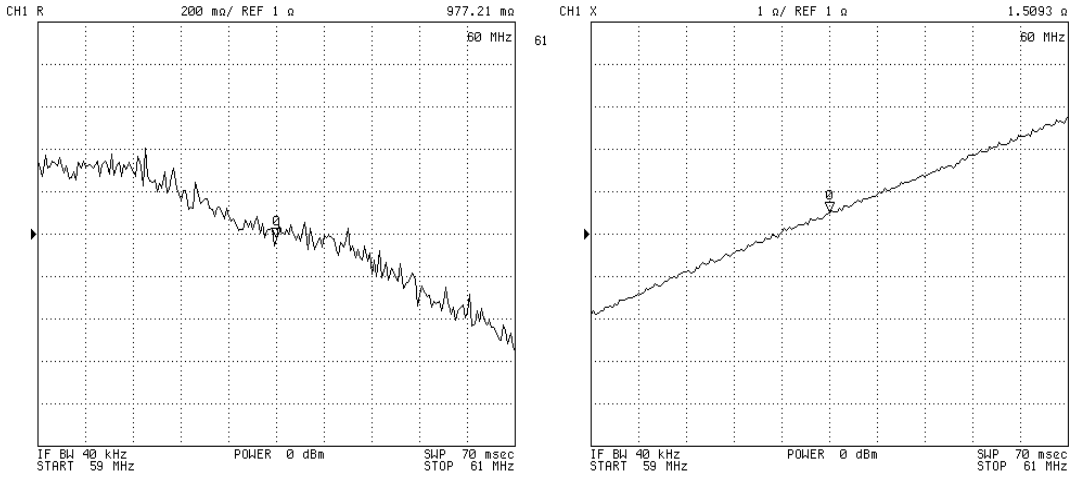

Figure 3.13: 60 MHz loop impedance after the capacitor was applied

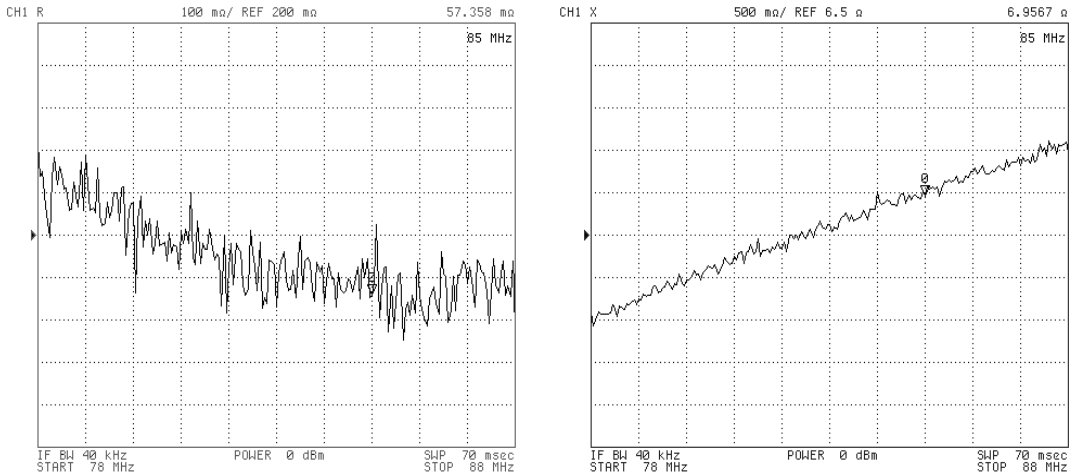

Figure 3.14: 85 MHz loop impedance after the capacitor was applied

or reference null voltage potential. To assure this circuit condition, the external conductor of the coaxial cable (our ground reference) was shorted to the copper pipe, while its internal part formed a loop before reconnecting to ground. A scheme of connections is given in figure 3.16.

In these antennas no capacitors were applied, by measuring their impedance it's possible to consider them as an equivalent Thevenin generator as seen in figure 3.10(b). Since the cable connecting the receiving antenna to the spectrum analyzer showed some coupling problems it's preferable to apply a variable attenuator between the antenna and the cable. This attenuator, set at 10 dB, made the impedance seen by the cable very close to $50 + i0\ \Omega$, so the reflection coefficient was reduced. Obviously the 10 dB attenuation was directly added to the spectrum analyzer results, since the system was linear.

Figure 3.15: Receiving loops

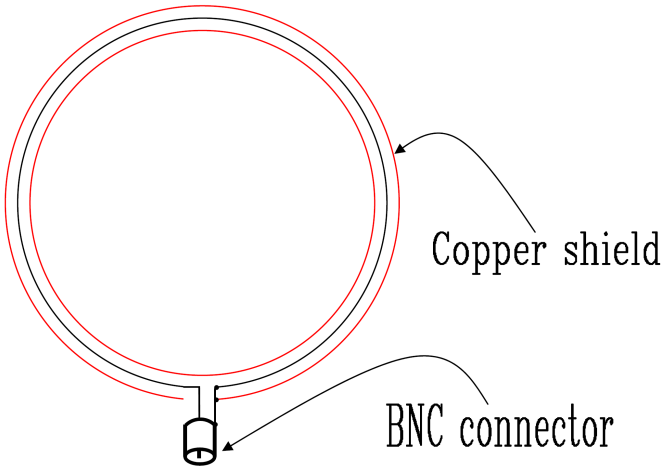

Figure 3.16: Connections between wires and shield

3.5.3 Measurement setup

To feed the transmitting antenna, a Tektronix AFG 3101 wave generator was connected to it by a BNC-type cable. The receiving loop was directly connected to a HP 8494A adjustable attenuator to adapt the 50Ω characteristic impedance of the wire. The wire was a N-Type about 5 meters long and led the signal to an Agilent E4402B spectrum analyzer. The current flowing in the transmitting loop was calculated from the impedance of the antennas and the impedance of the generator. Indeed the load was not adapted while the coaxial cable used was 50Ω characteristic impedance.

The OATS was the same considered in the previous section with a 6×7 meters reflecting surface. Since scanning the receiving antenna height is necessary in order to take account of the interference between direct and reflected waves, a special mast with wood, ropes and plastic supports without iron or ferromagnetic parts has been built. This type of construction, with a sliding support came out to be very useful to maintain the cable as stable as possible. In figure 3.17 the whole site and a detail of the mast are shown; it is also evident that the surrounding

Figure 3.17: The OATS realized at the C.R.E.I. Ven facility and the sliding support on the mast

environment is not ideal, because many ferromagnetic objects are quite close to the site and could interfere with the measurements. The distance between the mast and the transmitting loop was 3 meters while the height of the receiving loop was swept from 1 to 3 meters in 20 centimeters steps. The mast was closer to the reflecting ground edge to avoid as much as possible the cable interferences.

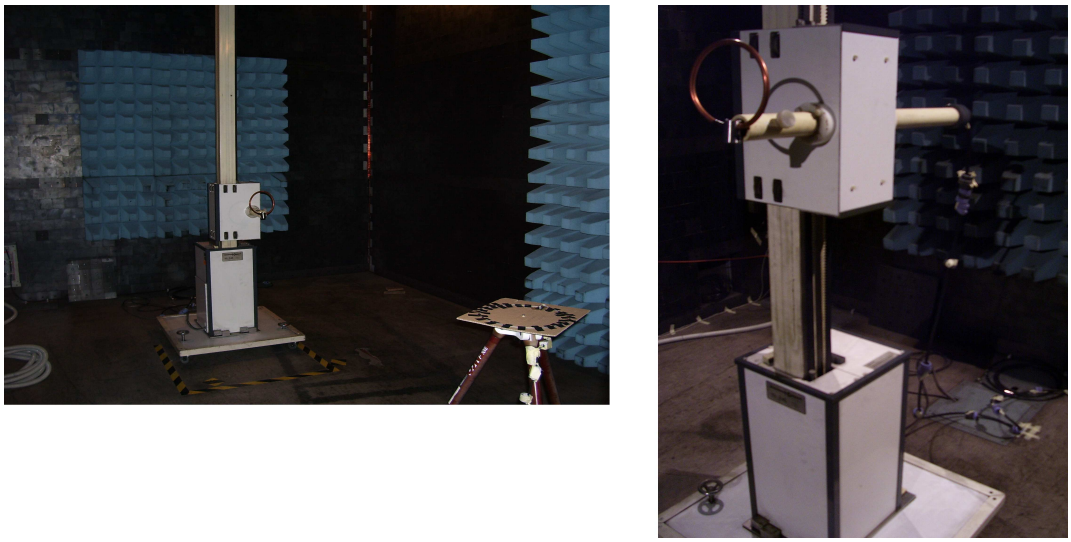

Figure 3.18: The anechoic chamber setup

The configuration used for the Anechoic Chamber was exactly the same used for the OATS: the same distance, same instruments, same orientations. The only handicap is that it could not scan the whole height as outdoor, because the maximum height inside was just two meters. Inside the chamber, in fact, the mast used was an automatic one with a height range of 1-2 meters. A picture of the employed set up is reported in figure 3.18.

3.5.4 Theoretical Predictions

Starting from all the theoretical considerations seen in previous sections, prediction of the received H-field and, in particular, its behavior while scanning the receiving antenna's height is presented here. The parameters used are the horizontal distance between antennas, the orientation of the loops, the input voltage, the frequency, the attenuation of the adjustable attenuator and obviously the receiving loop height. All computations refer to an ideal situation with ideal ground reflection and no objects around. These trends consider a $8V_{pp}$ sinusoidal voltage applied at the transmitting loop, no attenuations, a horizontal distance of 3 meters and a height scan of 1-3 meters. The estimated magnetic field strength is given as the module of the **H** vector in A/m for each working frequency and for each loop orientation. Using the following formulas all the theoretical results have been then transformed into dBm to be directly compared with the values measured by the spectrum analyzer:

$$\begin{gathered} V_{OC} = \omega \pi a_r \mu_0 H, V_{sa} = V_{OC} \frac{50}{50+|Z_{IN}|} \\ \Downarrow \\ P_{rx} = 10 \cdot \log_{10}(1000 \cdot \frac{V_{sa}^2}{50}) \quad \text{[dBm]} \end{gathered} \tag{3.16}$$

where a_r is the receiving loop radius, Z_{IN} its internal impedance and V_{sa} the voltage on the 50Ω input resistance of the spectrum analyzer. V_{OC} and H are the root mean square (RMS) values. In Figure 3.19(a), 3.19(b) and 3.19(c) the results are shown for each frequency.

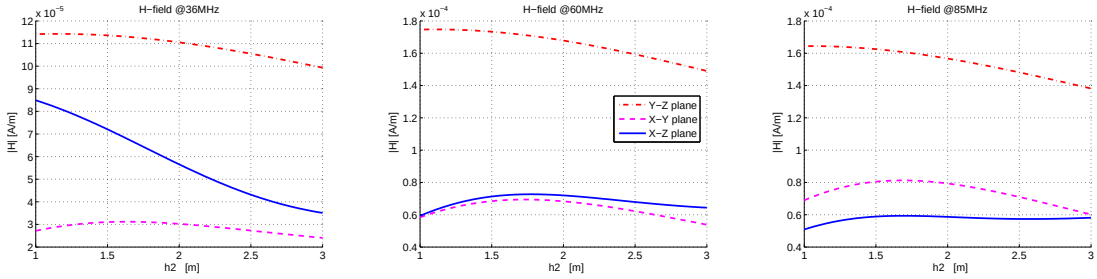

(a) (b) (c)

Figure 3.19: Estimated H-field at 36, 60 and 85 MHz

A description of the matlab script used for the simulations is reported in appendix A.

3.5.5 Grounding and parasite effects

In every circuit there has to be a path for the current leaving any supply voltage line to return to its source. This return path is commonly at a low reference potential, usually the ground potential. Ideally the ground should be at a uniform potential but this is never true, since it cannot have zero impedance and so the distribution of potentials will depend on the current flowing. The ground return is often, but not always, connected to the earth potential, which is the potential the Earth as a whole has with respect to the "rest of the universe". The combination of the current flow and the unavoidable earth impedance means that transient voltages appear at various locations on the ground. Herein lie some problems found during the OATS

measurements: a particular non-linear behavior of the setup has been revealed. The cause of such a problem is the cable carrying the received signal from the loop to the spectrum analyzer. Indeed this coaxial cable is also surrounded by the generated electromagnetic field, so the external conductor works as a dipole antenna. The scheme of this problem is shown in figure 3.20: the external shield of the N-type cable forms a parasitic capacitance with the ground and a current starts to flow on the conductor, influencing the voltage at the spectrum analyzer input. Many solutions have been tried to reduce this interference, but no one was good enough. Toroidal rings of ferrite material were put around the cable, all along it. We also tried to wrap the cable in aluminum foil to create a continuous shield. Anyway, some degree of interference to the power measured by the spectrum analyzer was still observable. To make the experiment as repeatable as possible, the cable was hung as still as possible, at a constant height.

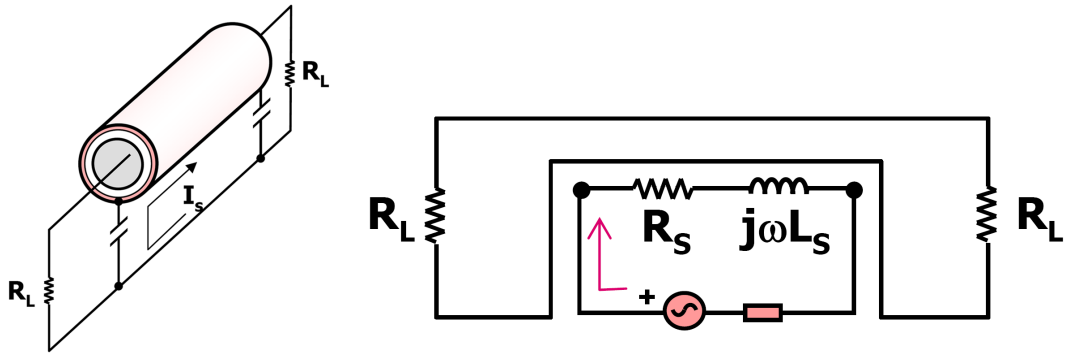

Figure 3.20: The equivalent scheme of a cable with parassite reception

3.6 Measurement analysis

Measurements have been done scanning the receiving antenna height. For the OATS the range 1-3 meters above the ground was divided into 20 centimeters steps. The first remarkable thing is that, in general, there is an attenuation between the effective power received and the theoretical power received. Obviously conditions of the OATS and the antenna factors are not ideal so this is the major problem to deal with. The same procedure was followed in the anechoic chamber. The height of the chamber is 3.34 meters so the mast built for the OATS was too tall (3.60 meters on the whole) to be used. The antennas were plugged on the automatic mast already present in the chamber. This mast can be controlled by a remote device in the control room but could only take the antennas to a height of 2 meters. In figures 3.6, 3.6 and 3.6 the continuous line represents the theoretical predictions, the stars are OATS measurements and circles are AC measurements.

36 MHz

For this working frequency the OATS trend is very similar to the predicted one. The main difference is attenuation, in each case varying between 4 and 7 dB. Also the AC trend is very close to the simulation for every antenna orientation. However the attenuation difference shown by the magnetic field between OATS and AC is bigger than 4 dB, especially in X-Y and X-Z

cases, while,as seen in Figure 3.2(a), the electrical field attenuation was within this range for every polarization.

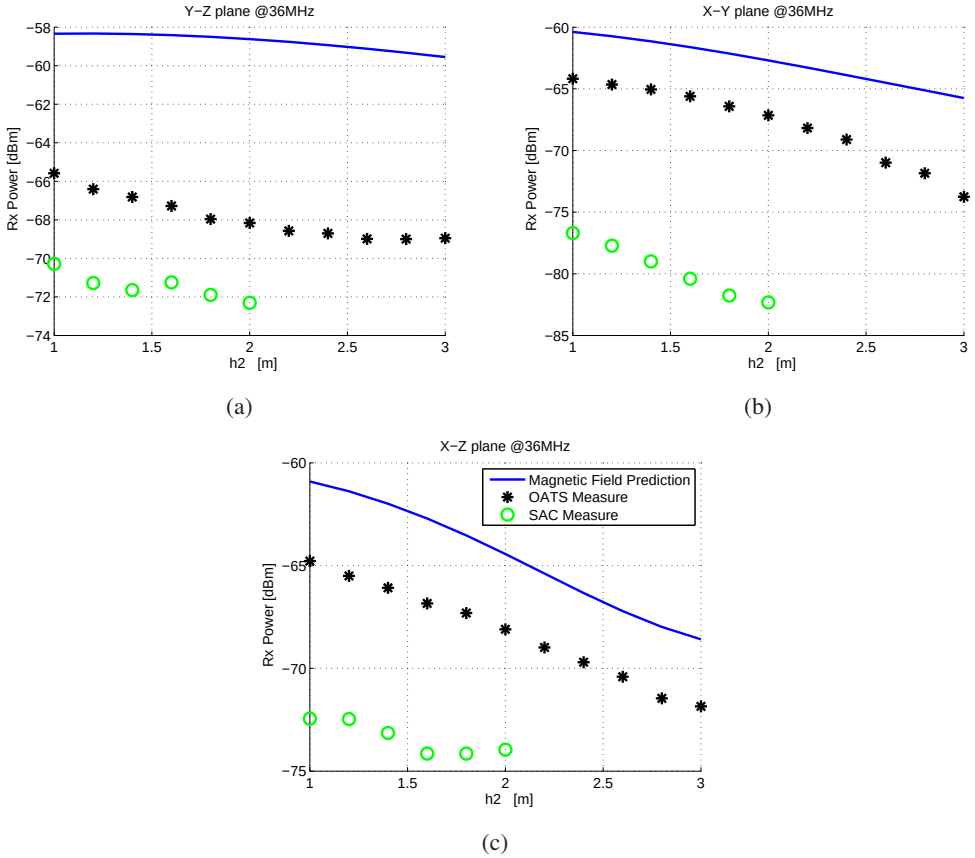

Figure 3.21: 36 MHz results

60 MHz

In this case the wavelenght is 5 meters. As a consequence the OATS can be considered "bigger", i.e. it is more similar to an ideal situation if compared with the 36 MHz case. So the trends are very similar to the simulation results even if a considerable attenuation is still present. For anechoic chamber measurements this attenuation is bigger and in the X-Z plane it is also bigger than 4 dB, that is the edge considered for the electrical field.

85 MHz

This is the highest frequency used. Beyond 88 MHz, in fact, FM broadcasting could interfer with measurements. In this situation the free-space wavelenght is about 3.5 meters. The OATS works very close to predictions even the attenuation is stronger at lower through heights of the receiving antenna. It should be considered that the the reflecting ground plane was not perfectly smooth and its wrinkles may have affected the propagation. At this frequency the attenuation difference between AC and OATS is within ± 4 dB almost everywhere. Anyway the height-scanning behavior is not comparable to the prediction and neither to the OATS trends.

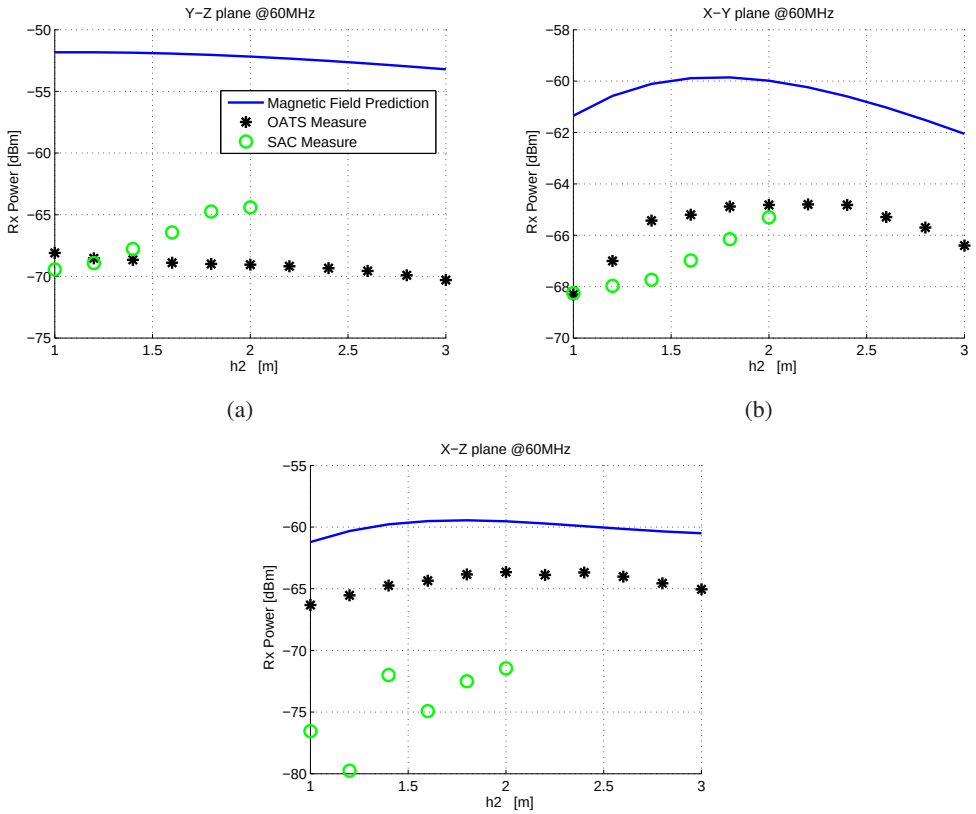

(a) (b)

(c)

Figure 3.22: 60 MHz results

From the presented results some interesting observations can be made. The equations used and their consequent computations are very powerful and precise even when their parameters and their variables are approximated, such as the constant current in the loop or the H strength on the whole loop area. Also the electrical schemes have been confirmed, specially when using the VNA, even if the realization of antennas was not carried out with a professional or industrial approach. In particular, the OATS results are very close to the estimated behavior and this is specially true for the height-scanning, which was the primary objective.
The anechoic chamber instead, turned out to be the most interesting and strange part, as already presumed in [23]. In this situation indeed, comparisons are always made using electric antennas. This approach, considering only the H-field components, has revealed that some differences may exist in this VLF range and in this particular chamber. The strangest part is that the measurements that best fit together are those relative to the lowest frequency, while we expected the opposite situation, that is, the larger the chamber is (compared to a wavelength), the better it works like an OATS. Maybe there are still some errors due to the physical limits of these setups and almost surely some small details were unavoidably not taken in consideration. By the end of next February a larger anechoic chamber will be ready in CREI Ven and more experiments are going to be done with the possibility of larger spatial scanning.

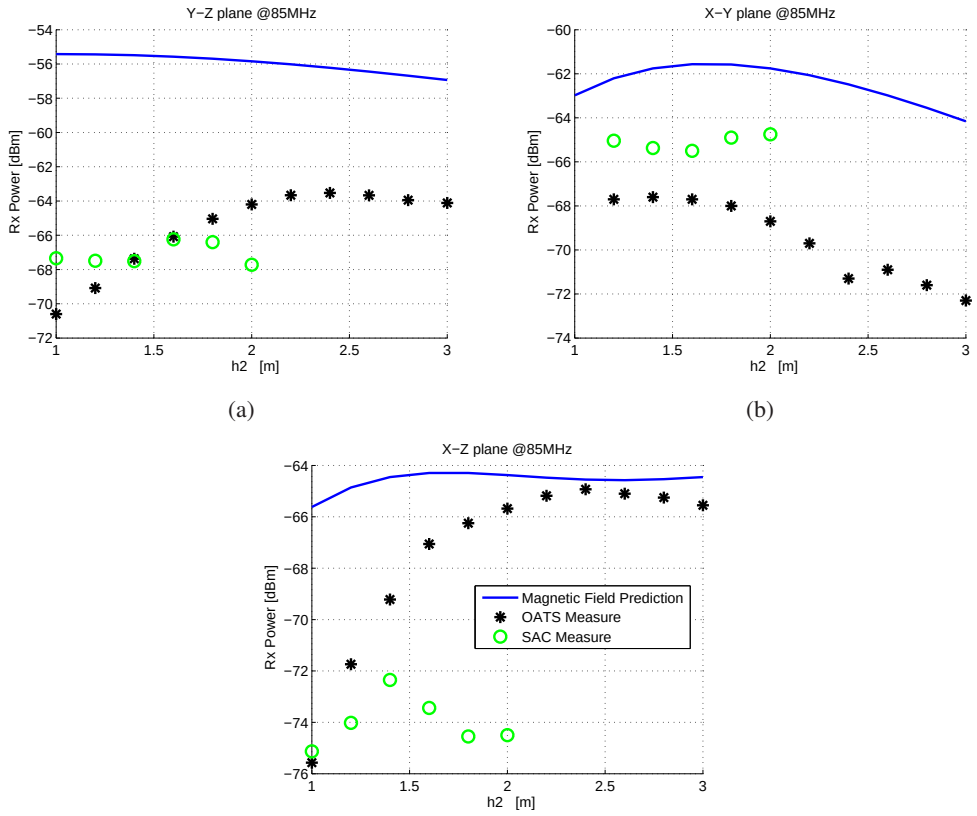

Figure 3.23: 85 MHz results

3.7 Electric Field Analysis

To complete this chapter, a simple demonstration is given here that using an electric source measurement results are better with respect the H-field analysis.

In a similar way to that used for H prediction, an estimation of the electric field radiated by a 'large' source (a folded dipole having length $l = 1.5m$) has been made starting from the basic equations for a single dipole given in [21]:

$$E_\theta = j\eta \frac{Ie^{-jkr}}{2\pi r} \cdot \left[\frac{\cos\left(\frac{kl}{2} cos\theta\right) - \cos\left(\frac{kl}{2}\right)}{sin\theta} \right] \tag{3.17}$$

where l is the physical length (resonance condition: $l = \lambda/2$), $k = 2\pi/\lambda$ and $\eta = \sqrt{\mu_0/\epsilon_0} \approx 120\pi$. Folded dipole radiation is double with respect the single one, so we compute double $I : 2I$. We have:

$$E_\theta(Folded) = j \frac{120Ie^{-jkr}}{r} \cdot \left[\frac{\cos\left(\frac{kl}{2} cos\theta\right) - \cos\left(\frac{kl}{2}\right)}{sin\theta} \right] \tag{3.18}$$

Taking into account the ground reflection (similar to figure 3.4(a)), the equation used are:

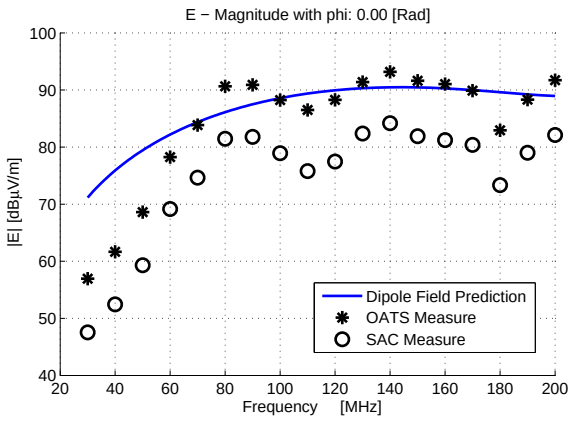

Figure 3.24: Folded Dipole: Measure and prediction

$$E_1(r=d_1) = j120Ie^{-jkd_1} \cdot \left[\frac{\cos\left(\frac{kl}{2}cos(\arcsin D/d_1)\right)-\cos\left(\frac{kl}{2}\right)}{D}\right]$$

$$E_2(r=d_2) = j120Ie^{-jkd_2-\phi_G} \cdot |\rho_G| \cdot \left[\frac{\cos\left(\frac{kl}{2}cos(\arcsin D/d_2)\right)-\cos\left(\frac{kl}{2}\right)}{D}\right] \tag{3.19}$$

$$E_{TOT} = E_1 + E_2$$

prediction of E_{TOT} magnitude in the range 30 MHz - 200 MHz (D = 3 m, h1 = h2 = 1 m) is reported in figure 3.24 (continuous line).

Effects of a large dimension field source are so examined by means of a folded dipole and the measurement of the field strength has been carried out by using a calibrated biconical antenna. Again, the tests (repeated in the OATS and inside the chamber) are compared with the theoretical propagation formula. Results are summarized in figure 3.24 (continuous line represents the electric field prediction, star dots the OATS measurements, circle dots the SAC measurements). The results show some 'attenuation' introduced by the chamber response and, of course, a better prediction in the far field region.

Chapter 4

LISN Calibration

A number of components are necessary for EMC testing. One of these is the Line Impedance Stabilization Network (LISN) used for conducted interference measurements. Conducted emission tests are performed in the frequency range 150 kHz - 30 MHz. In this range, interference sources within the equipment circuits or its power supply are coupled onto the power cable to the equipment. Interference may also be coupled either inductively or capacitively from another cable onto the power cable. In the CISPR standards attention has focused on the power cables as the prime sources on conducted emissions [26]. The measurement of common mode conducted emissions (CE) from an equipment under test (EUT) through power lines requires the use of a LISN [24]. The LISN is inserted between the power supply and the EUT as shown in figure 4.1.

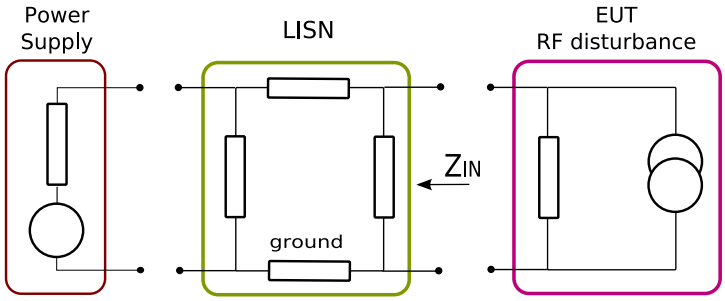

Figure 4.1: Conducted Emission Test

A LISN is a filtering device which realizes four important tasks:

i isolate EUT from AC power lines and related radiofrequency (RF) disturbances to prevent external noise from modifying measurements;

ii maintain a well-defined reference impedance at LISN EUT port with respect to frequency, this allows measurement reproducibility from site to site;

iii provide for the necessary power supply to EUT, this means that AC power can flow trough it;

iv convey EUT RF emissions to LISN RF output.

Filtering is performed through a set of 'series' inductances and 'parallel' capacitors, suitably designed and connected in order to operate in the frequency range from 9 kHz up to 30 MHz [26]. In fact, LISN parameters are not defined above 30 MHz, partly because commercial conducted measurements are not required above this frequency but also because parasitic components make a predictable design difficult to achieve.
One essential parameter of a LISN is the input impedance, Z_{IN}, at the EUT port, which must be periodically calibrated and compared to the reference values fixed in function of the frequency. In the old edition of the CISPR standard only the magnitude reference is present, instead the new one ([26]) also introduces a phase limit, as shown in figure 4.2. A lot of existing LISN present some problems in meeting the standards requirements, in particular with regards to the new phase limits. In fact, in this calibration task, non-trivial issues play a key role and must be carefully taken into account. One is related to the parasitic parameters at the LISN port, mainly due to both LISN internal components and leads at the connector side. Another is the influence of the external adapter used to connect the measurement system (RF generator and receiver) to the LISN port. Their effects are usually non-negligible variations of the Z_{IN} estimate itself [27]. For instance, in [28], results from experiments show that at frequencies close to 30 MHz, the estimated value of Z_{IN} may vary considerably, leading to measurement errors up to 5 dB.

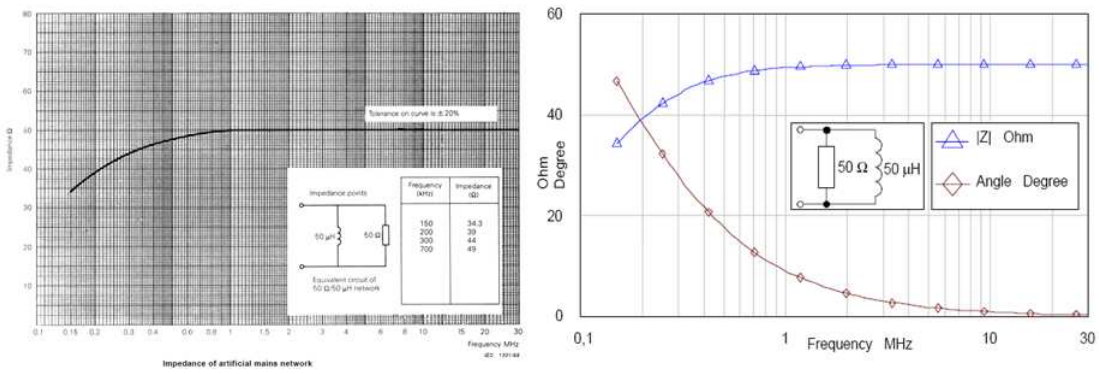

Figure 4.2: Comparison between the standard limits

In this chapter, the parasitic phenomena responsible for errors in the measurement of the LISN input impedance Z_{IN} at the EUT port are investigated. The aim of research activity is to improve the accuracy in the LISN calibration.

4.1 Parasitic phenomena on LISN input circuit

The input circuit of a LISN at the EUT side can be schematically represented as shown in figure 4.3a. In the figure, L_1 represents one of the two lines (or four lines in the case of a three-phase LISN) to which the EUT is connected. Z_{IN} is the impedance between L_1 and ground. RF signals coming from EUT are filtered by L and C_1, and drained to R, representing the impedance of the receiver input port ($R = 50\Omega$), through the bypass capacitor C_2. A more detailed scheme of the same input circuit is shown in figure 4.3b. With respect to figure 4.3a, this scheme includes some parasitic phenomena commonly arising, both inside and outside the

LISN, particularly relevant at high frequencies (near 30 MHz). In particular, C_L and C_R are the parasitic capacitances of L and R, respectively; L_R is the parasitic inductance of R, while R_1 and L_1 summarize the overall resistance and inductance at the input connector, due to both internal leads and external adapter. The model of figure 4.3b allows to analyse the effects of parasitic phenomena on the estimated Z_{IN}. An example is shown in figure 4.4, where the magnitude and phase of Z_{IN} are given in the frequency range from 150 kHz to 30 MHz for different values of L_1: 0, 150, 170, 220 nH. In the simulation, the other parasitic effects have been considered negligible, while L, C_1 and C_2 have been set according to the standard [26]: L = 50 H, C_1 = 1 F, C_2 = 100 nF. The diagrams clearly show that L_1, if not considered and suitably limited, may lead to non-negligible variations of both magnitude and phase of Z_{IN}. For instance, at 30 MHz (188 Mrad/s) and upon varying L_1 from 150 to 220 nH, the variations of magnitude and phase of Z_{IN} from the ideal values (corresponding to L_1 = 0 nH, i.e. 50 and 3 deg), are 1 to 9 and 12 to 27 deg, respectively. Therefore, L_1 should always be kept as low as possible, for instance by reducing parasitic elements at the external connector.

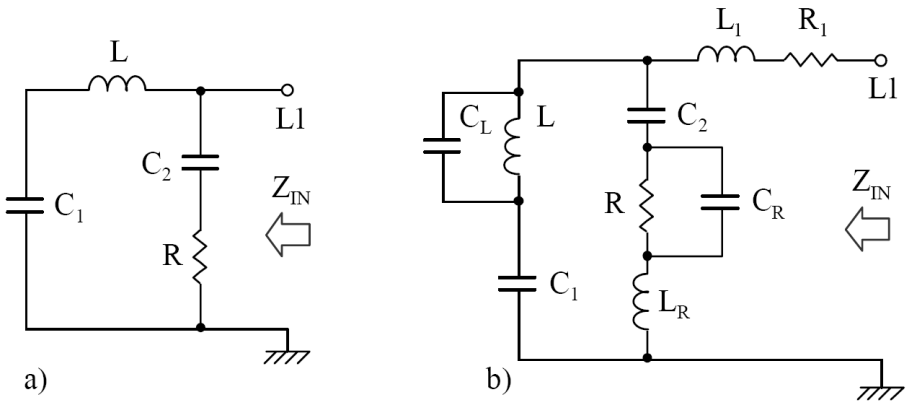

Figure 4.3: LISN input circuit at EUT side: a) without parasitic parameters, b) with parasitic parameters.

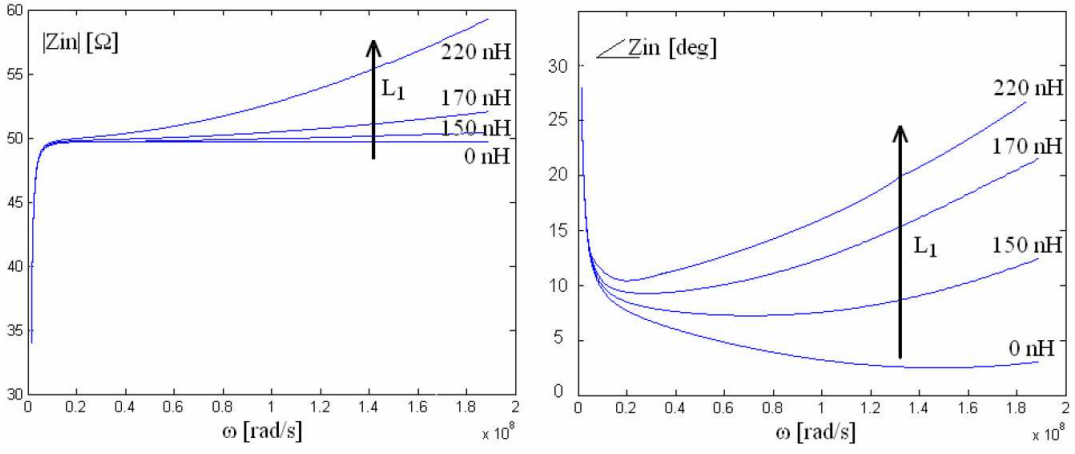

Figure 4.4: Effects of parasitic inductance L1 on magnitude and phase of Z_{IN}.

The simulation results given above have also been confirmed through suitable experiments,

carried out using a suitably made box shown in figure 4.5(a). Emulating a 'mini-lisn' it consists of a 50 Ω resistor bonded to the metallic chassis. With this simple object, we have observed how L_1 depends on wires length, and particularly, on the external connections. In fact, L_1 is a parasitic inductance due to the wire loop. A simplified equation for the value of the inductance is: $L = \mu_0 \cdot \Sigma$, where μ_0 is the magnetic permeability and Σ is the area described to the circuit. From the figure 4.5(b) we can observe the variation in the areas S1 and S2 in function to the field linked with the input circuit, from the connector through the ground loop. Consequently, the value of L_1 depends on the mechanical structure and on the wire dispositions.

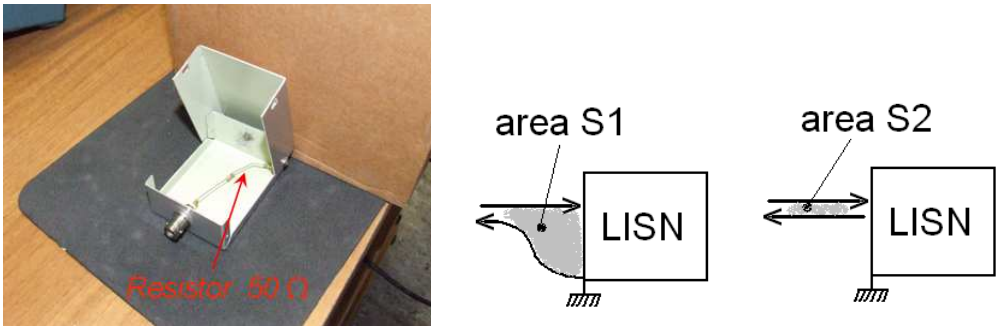

(a) (b)

Figure 4.5: fig: (a) AND (b)

4.2 Adapters and External Connections

The parasitic effects of the external connector can be mitigated through LISN adapters at the EUT port. Accordingly the research activity has been focused on the analysis of special adapters for the external connections. Three different adapters are presented in this section: Type A, B and C. A picture is shown in figure 4.6.

4.2.1 Type A adapter

The Type A adapter is commonly used for the calibration of Z_{IN} in a LISN. As shown in figure 4.7, it consists of an injecting pin and three bonding straps. In a typical calibration task, one strap is directly connected to the test bench ground, while the others are bonded to the LISN chassis. A schematic representation of the connection between the LISN and one adapter pin, together with its simplified equivalent circuit, are given in figure 4.7.

The figure highlights the path of the injected current, which flows through the injecting pin and returns through the bonding straps. It should be noted that the parasitic inductance L1 (= LA) depends on the area SA between the injecting pin and straps. This area may be very large and vary significantly from a measurement to another, depending on the disposition of straps chosen by the operator. This clearly implies large values of L1 and poor levels of achievable test repeatability.

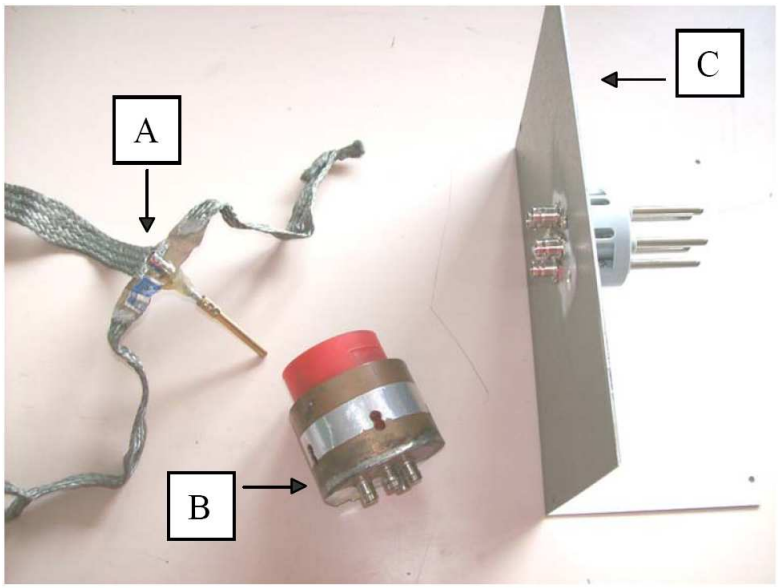

Figure 4.6: Different LISN adapters: Type A, B and C.

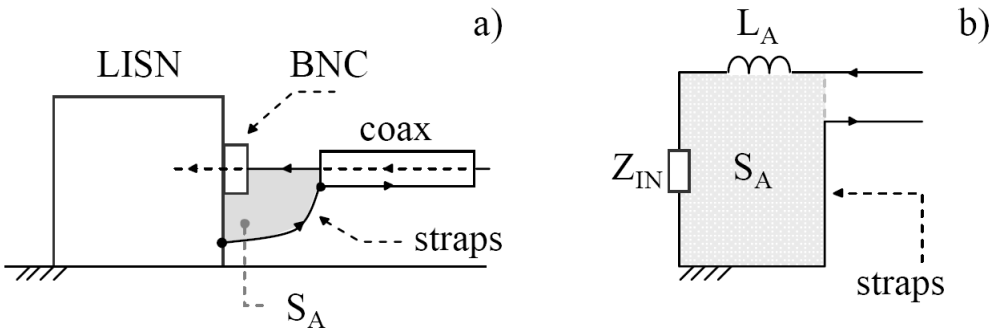

Figure 4.7: Type A adapter: a) description, b) equivalent circuit.

4.2.2 Type B adapter

The first improved adapter, denoted as Type B, is shown in figures 4.8 and 4.9. It consists of a common three-phase plastic socket to be plugged into the LISN connector (the same structure can be adopted for other socket versions). At the other side, four BNC connectors allow to measure Z_{IN} at each line of the LISN socket. The whole adapter and LISN socket are enclosed into cylindrical copper shields, used to minimize the return current path. The adapter shield is connected to the LISN chassis at one side, and to the outer metal covering of the BNC connectors at the other side.

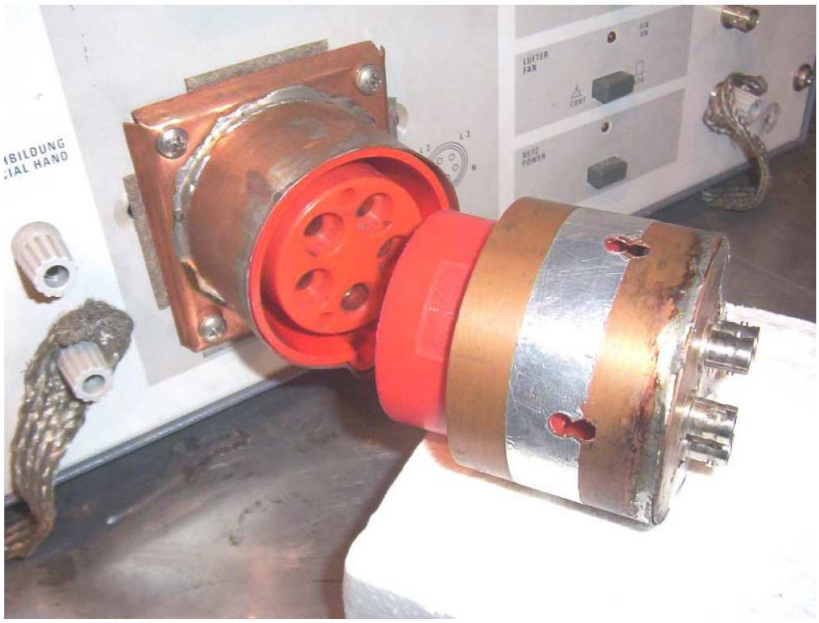

Figure 4.8: Type B proposed adapter for the calibration of LISN input impedance.

A schematic representation of the adapter and its simplified equivalent circuit are given in figure 4.9. With respect to Type A configuration, adapter B presents two essential advantages: (*i*) SB $\ll$ SA, hence LB $\ll$ LA, (*ii*) the mutual position of the injecting pin and return path is now fixed, and does not vary depending on the user choice of straps disposition. A much better measurement repeatability, and a consequently reduced calibration uncertainty, can be thus practically achieved.

4.2.3 Type C adapter

A second improved adapter, also shown in figure 4.6 (Type C), consists of a metallic L-shaped plate supporting the EUT socket. On the vertical plate, a BNC connector allows the connection of the EUT cable, while the horizontal plate is positioned under the LISN chassis to ensure a good ground connection. The adapter offers the possibility to bond, or not, the EUT socket ground pin directly to the metallic plate. A schematic representation of the adapter and the corresponding simplified equivalent circuit are shown in figure 4.10. In the figure, the injected current returns through the metal plate, along a circuit of area SC. The parasitic inductance

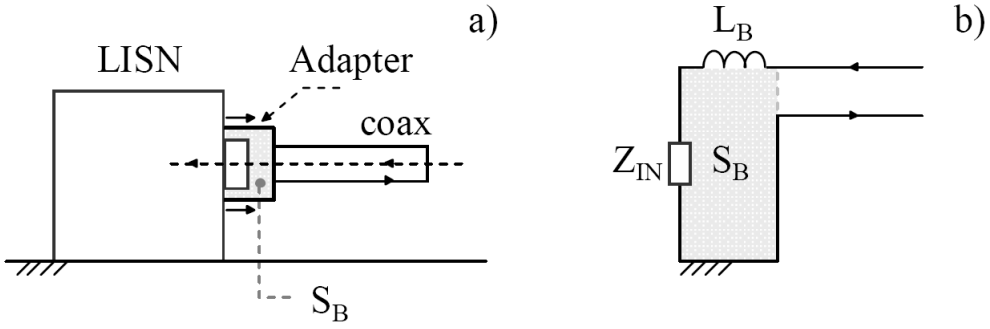

Figure 4.9: Type B adapter: a) description, b) equivalent circuit.

L_1 is represented as a series of two contributions: L_C, accounting for the 'self-inductance' of the circuit of area S_C, and L'_C accounting for leads internal inductance. In this case, $S_C \gg S_B$, hence $L_C \gg LB$. Nevertheless, the contribution of the capacitance, C_{LP}, should be also considered. It represents the parasitic capacitance between the LISN chassis and adapter vertical plate. A rough estimation of C_{LP} can be obtained through the expression: $C_{LP} = \epsilon_0 \cdot S_{LP}/d_{LP}$, where ϵ_0 is the dielectric permittivity of air, S_{LP} is the area of the facing portions of the LISN and vertical plate faced portions, while d_{LP} is their mutual distance. As shown in figure 4.10, and confirmed experimentally, C_{LP}, being in-parallel with L_C, should compensate for it, keeping the overall parasitic effect of L_1 low. Due to the fixed reciprocal positions between adapter and LISN, the measurement repeatability can be greatly enhanced with respect to adapter A also in this case.

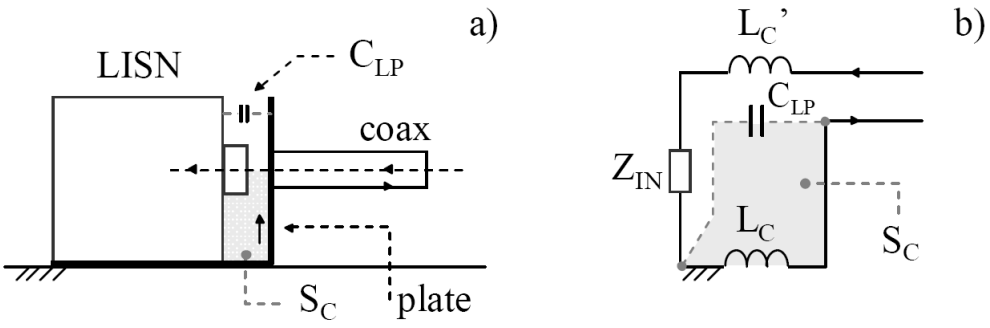

Figure 4.10: Type C adapter: a) description, b) equivalent circuit.

For the Type C adapter of figure 4.6, $C_{LP} \cong 5$ pF. In figure 4.11, results from simulations performed on the equivalent circuit of figure 4.10 are summarized. In particular, the values of Z_{IN} are shown (magnitude and phase) upon the varying of frequency and with: C_{LP} = 5 pF, L_C = 120 nH, L'_C = 50 nH (i.e. L_1 = 170 nH). With respect to figure 4.4 , lower deviations of Z_{IN} from the case L_1 = 0 nH, both in magnitude and phase, can be observed. For instance, at the highest considered frequency, 30 MHz, the values of $|Z_{IN}|$ and $\angle Z_{IN}$ decrease from 53 Ω and 20 deg (figure 4.4, L_1 = 170 Ω) to 51 Ω and 15 deg (figure 4.11), respectively.

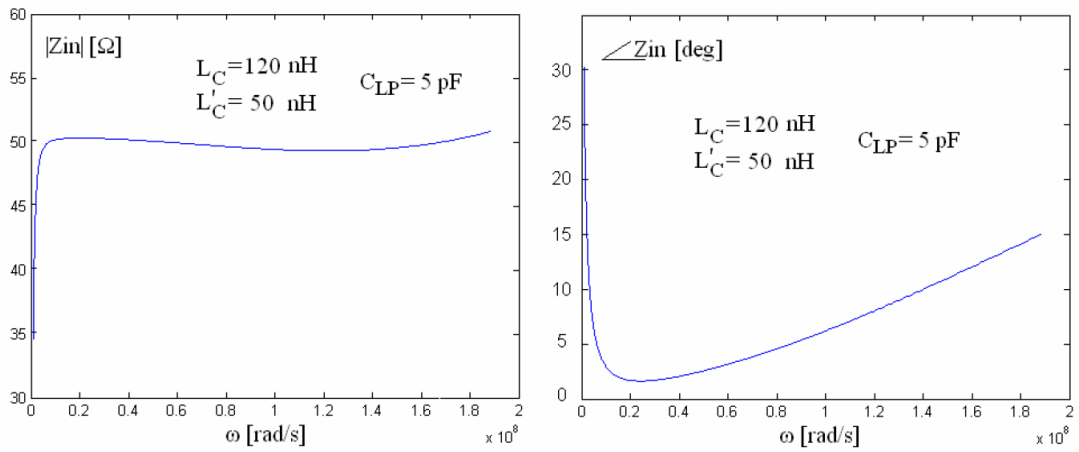

Figure 4.11: Type C adapter: Z_{IN} magnitude and phase simulations.

4.3 Experimental Results

A number of experimental tests have been performed, aimed at verifying and quantifying the effectiveness of the proposed solutions. A schematic representation of the test bed is shown in figure 4.12(a). It consist of a vector network analyzer (VNA) which generates a RF sweep into the LISN; incident and reflected component are separated by the RF power splitter (figure 4.12(b)).

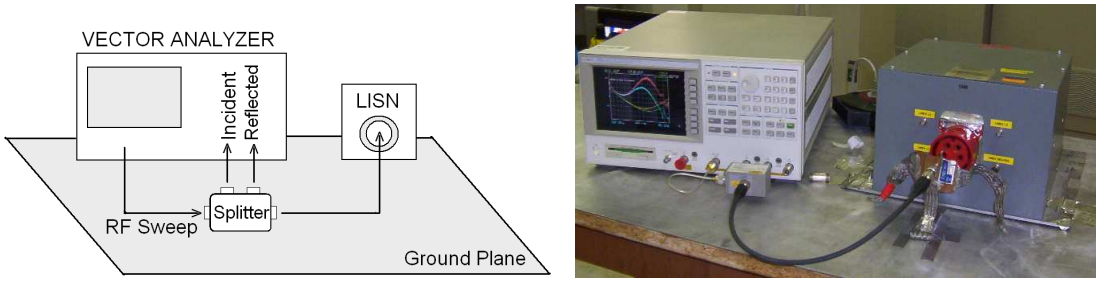

(a) (b)

Figure 4.12: Digram and picture of employed set up

Measurements have been performed in the whole frequency range 150 kHz to 30 MHz, and in the following adapter configurations:
a) Type A, with two straps bonded to the LISN chassis and positioned to minimize SA, and the third strap connected to the test bench ground plane;
b) Type A, like a), but with straps positioned to maximize SA.
c) Type A, with one strap bonded to the test bench ground plane and the others not connected (open);
d) Type B;
e) Type C, with ground pin unconnected;
f) Type C, with ground pin connected to metallic plate.

Some interesting results from experiments, obtained at the frequency of 27.2 MHz, are

summarized in Table 4.1 for the case of the Type A adapter. In the table, $|Z_{IN}|$ values are expressed in dBΩ (i.e. $dB_{1\Omega}$) and configurations a, b, c are analyzed.

Type A	(a)	(b)	(c)
$\|Z_{IN}\|$*[dB*Ω*]*	34.1	34.6	36.6
$\angle Z_{IN}[deg]$	19.7	21.3	27.5

Table 4.1: Measurement results for different Type A adapter configurations

The table clearly shows that with respect to the ideal value of Z_{IN}, i.e. 50 Ω ($\cong$ 34 dBΩ) and 0 deg, estimates of $|Z_{IN}|$ and $\angle Z_{IN}$ strictly depend on the position of the bonding straps. For instance, configurations a and c present differences in terms of $|Z_{IN}|$ and $\angle Z_{IN}$ even up to 2.5 dB and 7.8 deg. This confirms the dependency of Type A adapter measurements on the position of the straps chosen by the operator, and thus the poor repeatability of the test. Measurements have also been performed with Type B and Type C adapters. The whole set of results obtained in the frequency range from 150 kHz to 30 MHz, for configurations a, d, e, f, is shown in figures 4.13 and 4.14. From the figures, it can be observed that:

(i) the differences among adapter configurations are more evident at higher frequencies,

(ii) with respect to Type A, Type B and C adapters present a similar and more regular behaviour in the whole considered frequency range,

(iii) case d and f curves are rather close to each other, especially in terms of Z_{IN}, (iv) with configurations d and f, the obtained curves of $|Z_{IN}|$ and $\angle Z_{IN}$ are below the corresponding ones of a and e.

Therefore, Type B and C adapters, with ground pin connected, can be considered equivalent solutions to be used for minimizing the effect of inductive parasitic phenomena, and, consequently, for a more accurate characterization of the LISN input impedance.

In the above measurements of $|Z_{IN}|$ and $\angle Z_{IN}$, the effect of the adapter insertion loss has been implicitly accounted for. To check the frequency behaviour and 'quality' of the Type C adapter, a couple of them ('male' and 'female', see figure 4.15) has been realized and tested in a way somewhat similar to that used in immunity standards [29] to verify the characteristics of the coupling-decoupling networks (CDNs). The input reflection coefficient (S_{11}) and the transmission coefficient (S_{21}) of the adapters connected together (cascade) have been measured with a 50 Ω load at the output port. The results are quite good, the insertion loss of the couple of adapters being less than 0.1 dB up to 30 MHz and the variation of the input impedance well within 1 dB of the reference value (figure 4.16). Therefore, the insertion loss effect of Type C adapter on LISN Z_{IN} calibration measurements can be considered negligible, and the results shown in figures 4.13 and 4.14 can be assumed as accurate estimates of the analysed LISN input impedance.

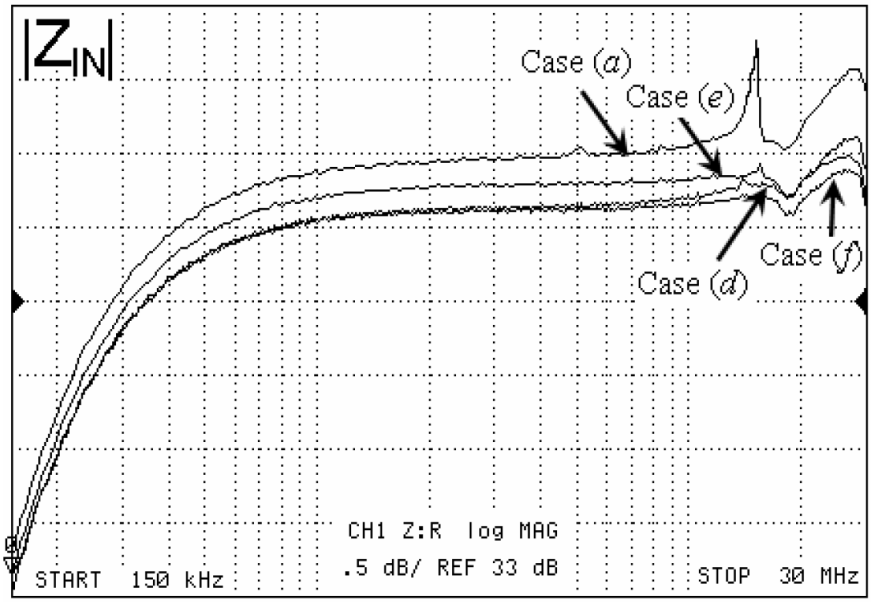

Figure 4.13: Measured values of $|Z_{IN}|$ with configurations a, d, e and f.

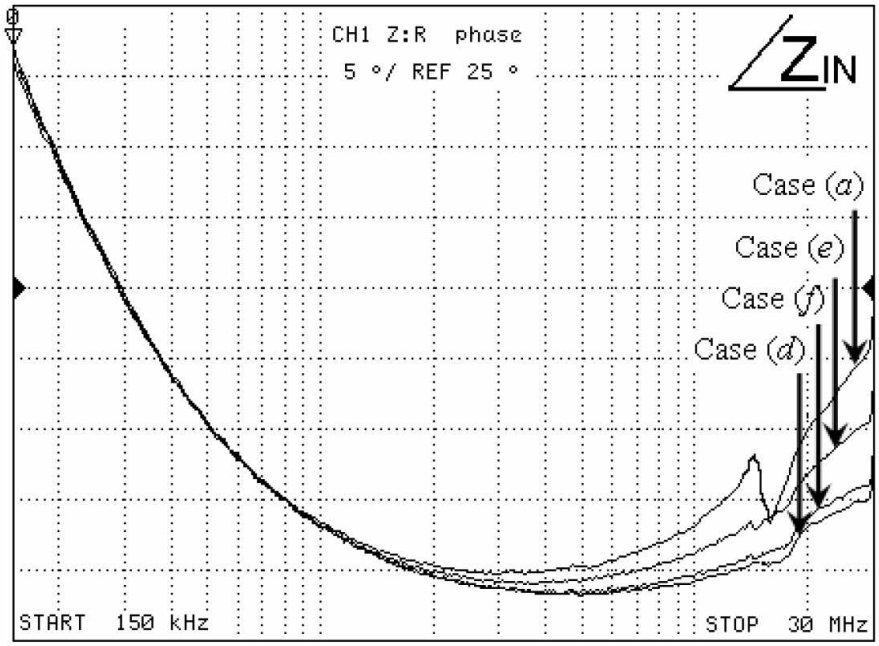

Figure 4.14: Measured values of $\angle Z_{IN}$ with configurations a, d, e and f.

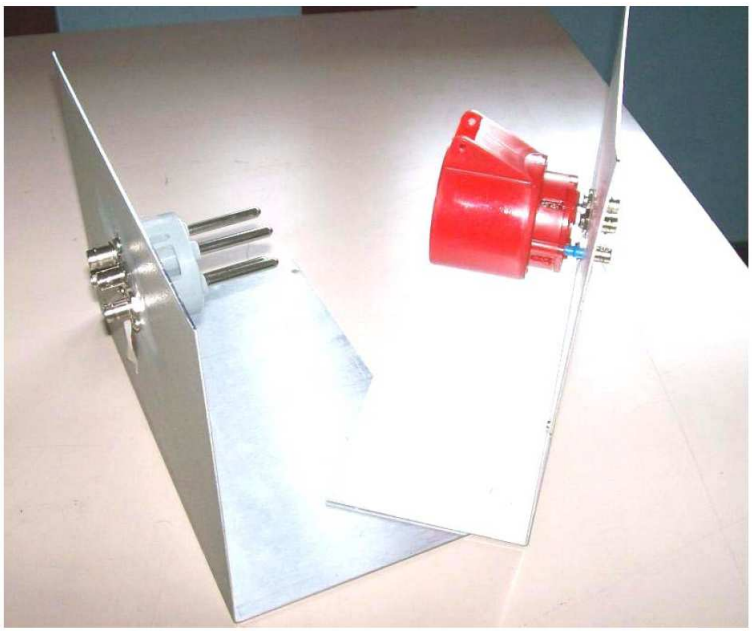

Figure 4.15: A couple of type C adapters (male - female).

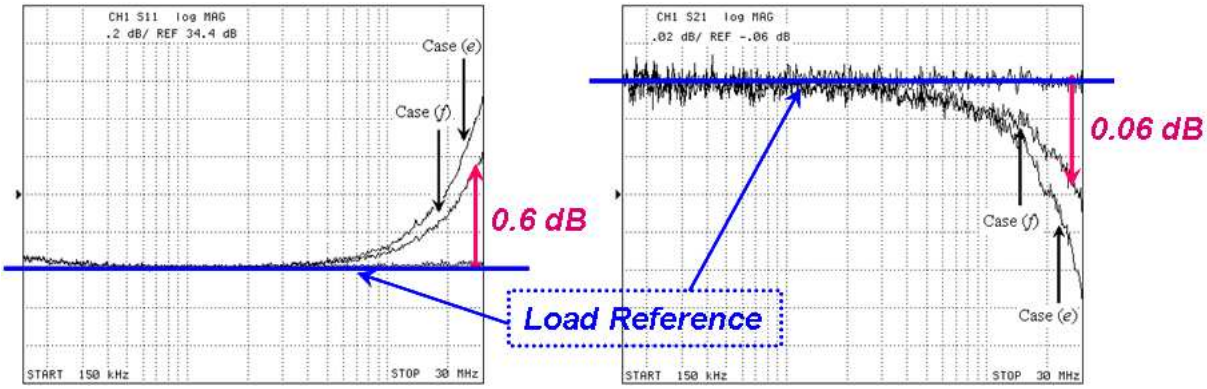

Figure 4.16: calibration of Type C adapter

Chapter 5

Uncertainty Evaluation in ESD Tests

When two non-conductive materials are rubbed together or separated, electrons from one material are transferred to the other. This results in the accumulation of triboelectric charge on the surface of the material. The amount of charge caused by movement of the materials is a function of the separation of the materials in the triboelectric series. Additional factors are the closeness of contact, rate of separation and humidity [24]. The human body can be charged by triboelectric induction to several kilovolt.
When the body approaches a conductive object, the charge is transferred to that object normally via a spark, when the potential gradient across the narrowing air gap is high enough to cause breakdown. Electrostatic discharges (ESDs) represent a well-known phenomenon in electronics The effects of such phenomena can be rather critical for electronic devices, and may provoke system failures or even permanent damages. In order to assess the immunity level of an equipment under test (EUT) to ESD, specific standards can be followed [30], [31]. In these standards, the immunity requirements and the test methods are defined for both contact and air discharge. The characteristics of the ESD discharges are also provided. Standard prescriptions are used in the setup stage of the ESD generator (also known as "gun") in order to provide discharges similar to those generated by the human body.
One important issue of ESD tests is the evaluation of the test uncertainty, and in particular the uncertainty contribution associated to repeatability. In these tests, in fact, repeatability is usually very low and the corresponding uncertainty contribution is typically rather high. In the literature, the repeatability of ESD tests is investigated in-depth in a number of specific contributions. For instance, [32] provides interesting results from an international comparison among ESD-generator calibration tasks. The results reported in this paper confirm the high variability of ESD test outputs and underline the importance of the measurement setup, which, in the comparison, was different from one laboratory to another. In [33], the uncertainty budget of an ESD test is discussed, with special regard to some specific uncertainty factors like measurement repeatability, cable and adaptor loss and time resolution. The uncertainty contributions in an ESD test are also dealt with in [30]. This standard suggests the diagram shown in figure 5.1 to take into account the influence on the test of parameters like the position and orientation of the ESD gun.

Unfortunately, in most such contributions attention is paid to the only case of contact dis-

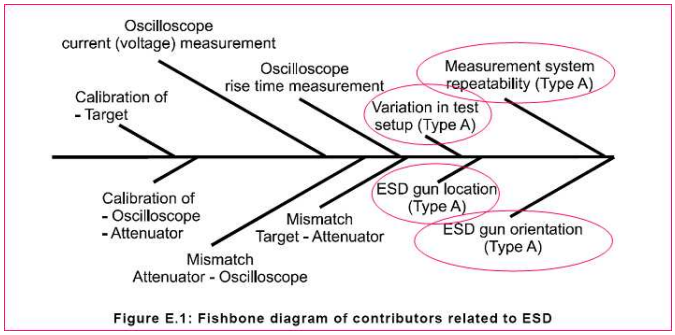

Figure 5.1: Fish diagram of IEC Standard

charges. Air discharge tests are instead seldom taken into account and little information is provided in terms of uncertainty evaluation. Interesting results are however provided in [34], in the case of air discharge tests and in terms of current waveform versus some physical parameters.

The contact discharge method represents the approach most considered in the standards. It also represents the simplest case to be analyzed in an uncertainty evaluation budget. In fact, being based on fixed positions of the gun, it requires a smaller number of terms to be accounted for. However, air discharge tests become needed any time contact discharge tests cannot be performed. In this case, the IEC standard [30] recommends to approach the gun tip as fast as possible to touch the EUT. Conversely, the ISO standard [31] recommends to move the tip very slowly in order to minimize the multiple discharges and ringing in the measurement equipment. In this chapter, the uncertainty of air discharge tests is analyzed with special regard to the contributions associated to the different parameters like speed and movement of the gun tip during the approach phase, gun inclination and relative humidity. The purpose of the research activities is to provide an original and efficient solution for improving uncertainty evaluation in air discharge tests.

5.1 Measurement Setup

5.1.1 Test Repeatability

The starting point is, as already mentioned, to acknowledge that the ESD phenomenon is scarcely repeatable by nature. Indeed, this fact affects remarkably the calibration task of an ESD generator. The calibration of the generator, performed as recommended in [30] or [31], gives the first important contribution when evaluating the uncertainty budget of an ESD test. From the examination of many ESD calibration reports produced by accredited laboratories, it is evident that:

- the uncertainty values associated to the measurement of the contact discharge parameters are lower than those associated to the air discharge parameters (typically, 8% for the peak of the current waveform and for current values at fixed discharge times, 5 to 7% for the rise time, in a contact mode calibration; in the order of 25% for rise time and 10 to 15% for discharge time constant, in an air mode calibration);

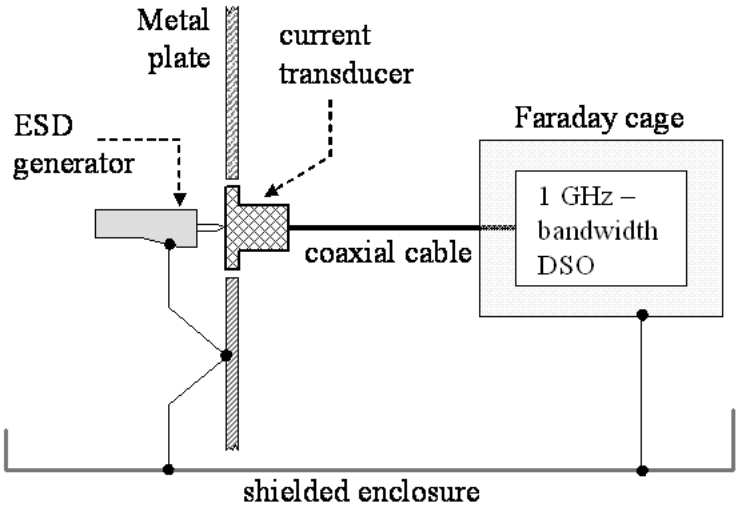

Figure 5.2: Description of the used measurement system

- the type A contribution (σ) to the uncertainty value (mainly due to the measurement repeatability) cannot be better than 20% (for instance, in the case of INRIM[1] calibration reports) for ten to twenty repeated air discharges, while it is usually in the order of 3 to 5% for ten repeated contact discharges. To investigate this matter a measurement system will be proposed and described in the following section.

5.1.2 Measurement System and Setup

A schematic representation of the measurement system used in the ESD calibration is sketched in figure 5.2. The system is compliant with the standard [30] and is suitable for the assessment and verification of ESD generator characteristics.

The set up is composed of the ESD generator, a digital oscilloscope placed inside a Faraday cage to shield it from the electromagnetic field radiated by the ESD generator discharge and the target which consists of a metal plate and a current transducer.

The system used for the experiments is shown in figure 5.3 and is similar to the previous one. It presents a special slide allowing horizontal movement, with speed control and includes the following items:

1) ESD generators: KeyTek MZ-15/EC MiniZap or EMC-Partner ESD 2000, placed over the slide;

2) a 1.0 m x 1.0 m vertical metal plane;

3) a coaxial current transducer mounted in the centre of the vertical metal plate;

4) a radiofrequency (RF) interconnection coaxial cable;

5) a digital storage oscilloscope (DSO) Tektronix DPO 7054 (1 GHz frequency band),.

As shown in the figure, the metal plate and Faraday cage are both grounded to the surrounding shielded enclosure. The ESD generator is instead connected to the metal plate. Pictures of

[1]National Institute of Metrological Research - Torino, Italy

the test system, with a detail view of the ESD generators and the sliding mechanism are given in figures 5.4(a) and 5.4(b) for the KeyTek and EMC-Partner generator respectively. The two micro-switches are used to monitor the length of the time interval in which the slide is moved and consequently the speed of the gun.

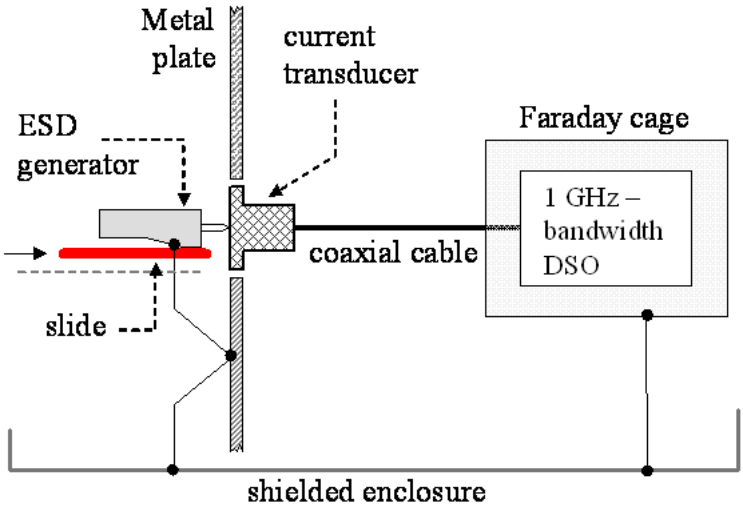

Figure 5.3: Detail of the used test system

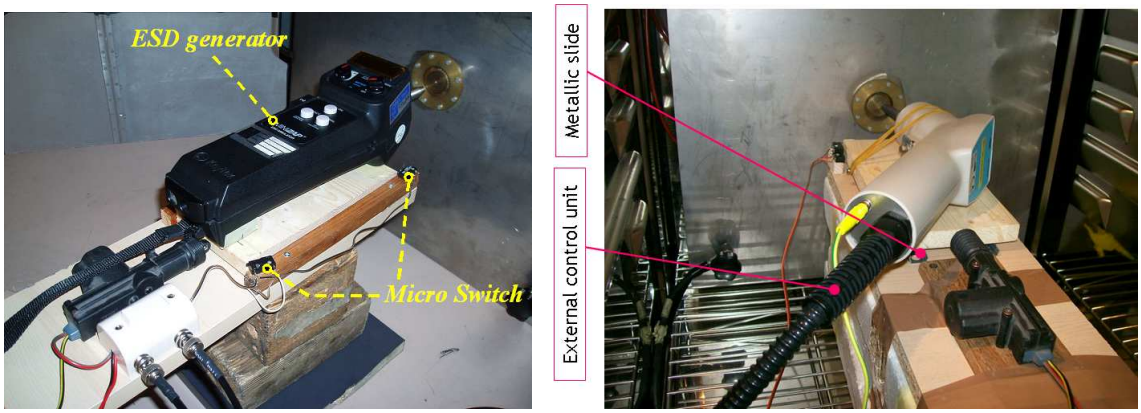

(a) (b)

Figure 5.4: Pictures of the used guns

A typical waveform of the output current from the ESD generator is shown in figure 5.5 [30]. The figure highlights the main parameters to be considered for the characterization of an ESD generator: the peak value of current, I_P, the current values at 30 ns and 60 ns from the peak instant, I_{30ns} and I_{60ns}, respectively, and the rise timet_r.

Special attention has been paid in order to reduce the influence of humidity variations on test repeatability and accuracy. To this aim, both the humidity and temperature have been properly monitored and controlled in all the performed tests. An effort has been also made to reduce the influence on test accuracy of the variations of the angle between the ESD gun tip and the target plane (current transducer) [35]. To this aim, the angle has been maintained as

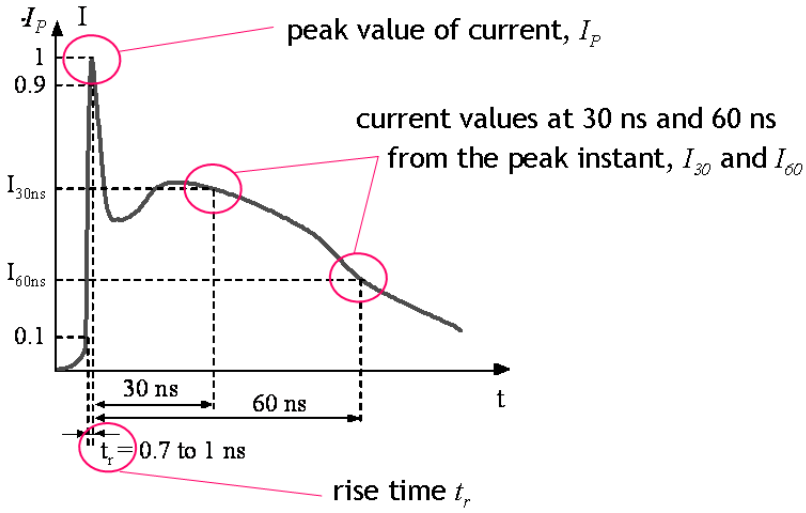

Figure 5.5: Typical waveform from an ESD generator output

orthogonal as possible with respect to the target plane, during all the performed experiments. In order to investigate the effects of the gun speed on the measurement, five different values have been considered: (i) very slow (≈1 cm/s), (ii) slow (≈2 cm/s), (iii) normal (≈4 cm/s), (iv) fast (≈7 cm/s), (v) very fast (≈12 cm/s). Such values have been chosen considering the experience of some in-the-field operators, interviewed on purpose about their perceived meaning of the speed concept introduced in [30] and [31]. The voltage at the tip side has finally been set at the following peak values: 4, 6, and 8 kV, while the current, I, has been measured through the DSO, by means of ten repeated observations.

5.2 Experimental Results

A number of experiments have been performed with the measurement setup described in the previous Section. Tests have been repeated in different setup configurations, while varying the gun speed, humidity and tip angle.

5.2.1 Gun speed effects

In figures 5.6, 5.7, and 5.8, the results obtained from ten acquired waveforms of I and for the voltage levels 4, 6, and 8 kV are shown. The standard deviation (σ) for each time sample is shown to better highlight the variability of the current estimates around the mean value, and, ultimately, to check the repeatability of the test. In the diagrams, only the two boundary speed configurations ('very fast' and 'very slow') are shown.

The diagrams clearly show a remarkable difference between the curves obtained with a very slow speed compared to those obtained with a very fast speed. In particular, the major differences can be noted at the peak time instant. This confirms the strong influence that the chosen ESD gun speed may have on the current waveform and on parameters like the peak value. They also highlight non-negligible values of the standard deviation around the mean

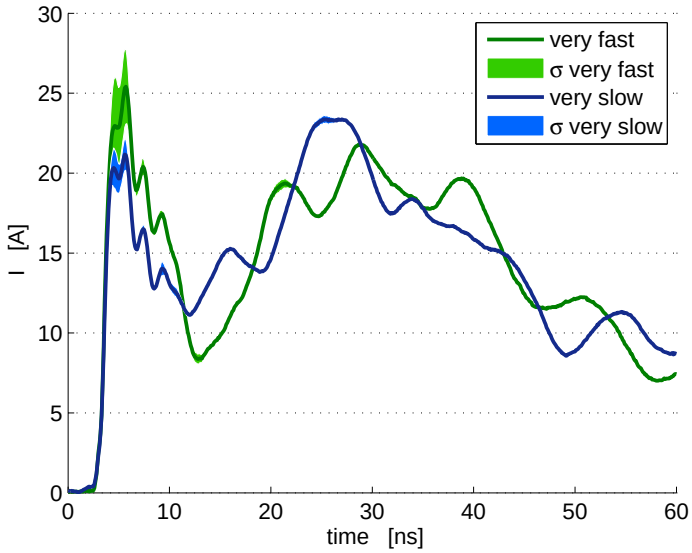

Figure 5.6: Acquired current waveforms with a 4 kV voltage

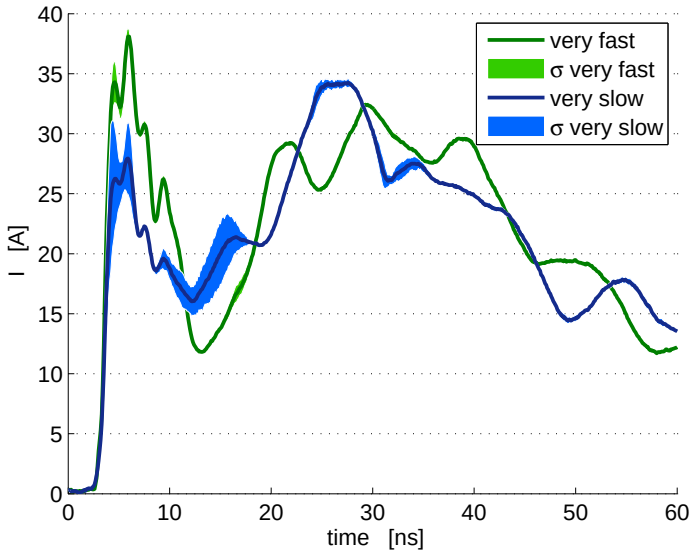

Figure 5.7: Acquired current waveforms with a 6 kV voltage

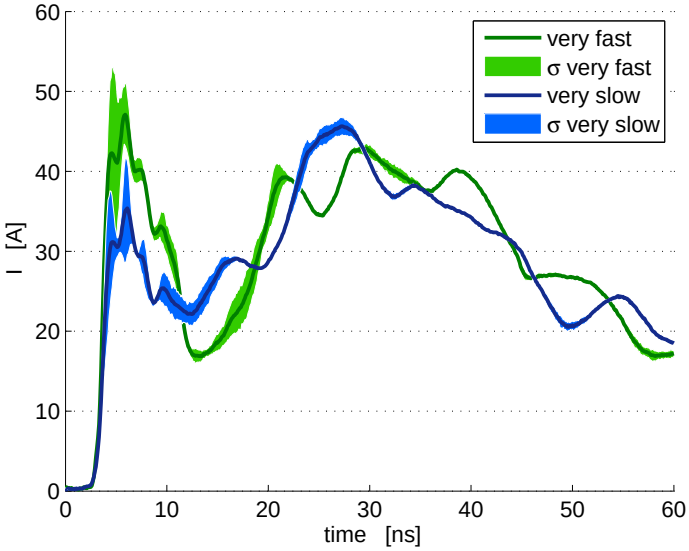

Figure 5.8: Acquired current waveforms with a 8 kV voltage

value, especially at the peak time instant (in figures 5.7 and 5.8). Clearly this fact has severe consequences in terms of measurement repeatability.
From the curves of figures 5.6, 5.7 and 5.8, the above recalled parameters I_P, I_{30ns}, I_{60ns}, and t_r can be estimated. Such results (mean values) are summarized in tables 5.1, 5.2, 5.3 and, for convenience, also in figures 5.9(a), 5.9(c), 5.9(b), and 5.9(d).

4 kV	t_r [ns]	I_P [A]	I_{30ns} [A]	I_{60ns} [A]
Very Fast	1.4	25.41	18.87	8.01
Fast	1.5	24.40	18.00	7.85
Normal	1.1	20.77	17.75	8.11
Slow	1.1	20.02	17.26	7.75
Very Slow	1.1	21.17	17.98	7.78

Table 5.1: Results with a 4 kV voltage

6 kV	t_r [ns]	I_P [A]	I_{30ns} [A]	I_{60ns} [A]
Very Fast	1.6	38.10	29.30	12.62
Fast	1.6	35.52	29.46	12.80
Normal	1.3	31.54	27.16	12.24
Slow	1.3	29.97	21.17	11.57
Very Slow	1.3	27.93	26.98	12.44

Table 5.2: Results with a 6 kV voltage

Tables and figures confirm the strong dependence of the current values on the ESD gun speed. For instance, in the case of the peak current, an I_P reduction of 21.2, 26.7, 24.4% is observed by reducing the speed from 'very fast' to 'very slow', for the cases of 4, 6, 8 kV respectively. Smaller differences can be observed for the other parameters, where the obtained values appear more independent of the chosen gun speed.

8 kV	t_r [ns]	I_P [A]	I_{30ns} [A]	I_{60ns} [A]
Very Fast	1.8	47.10	39.59	17.28
Fast	1.8	46.96	39.76	17.28
Normal	1.8	43.60	39.40	16.16
Slow	1.7	37.89	35.61	16.15
Very Slow	1.7	35.39	37.02	17.33

Table 5.3: Results with a 8 kV voltage

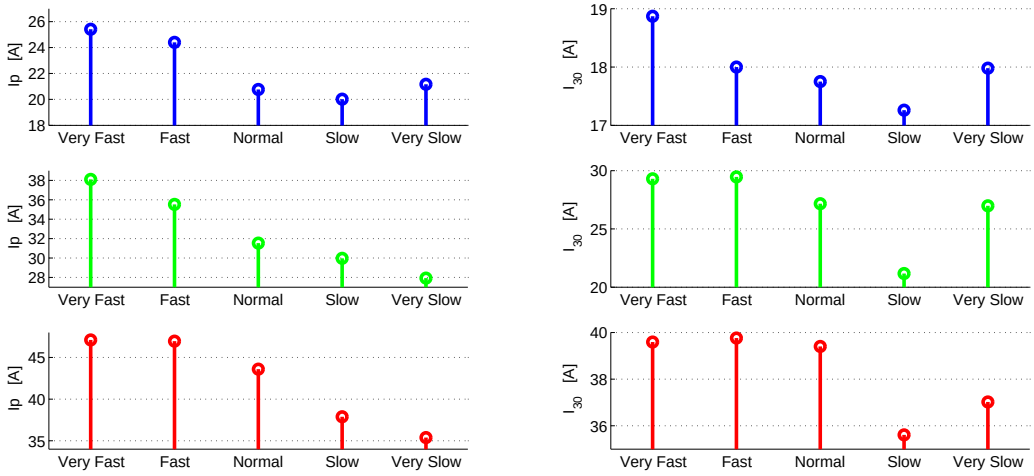

(a) (b)

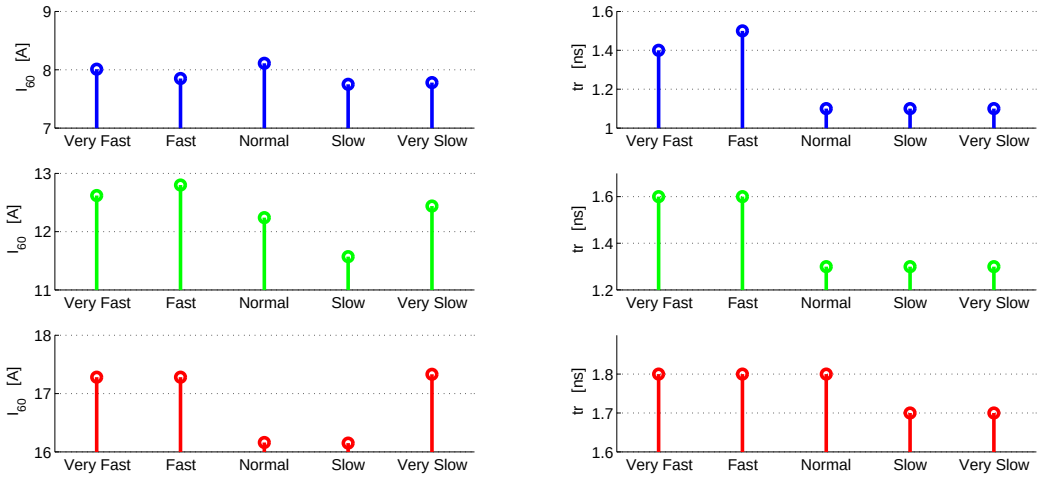

(c) (d)

Figure 5.9: Summary of values: (a) I_P, (b) I_{30ns}, (c) I_{60ns} and (d) t_r,

The fact that the speed of the gun influences the first peak of the discharge current is due to the different instant at which the arc occurs. In fact the time required for air ionization is comparable with the path-time of the gun during the approach. As a consequence, with a high speed the arc occurs at shorter distance than that occurring with a slow speed. Moreover, the parasitic capacitance between the body of the ESD gun and the object where the discharge occurs should be taken into account, as shown in [36]. For the high frequency components of the ESD current this capacitance (typically some picofarad) offers an alternative path with respect to the strap used for grounding the ESD gun. When approaching the gun to the object with a faster speed, the ESD event occurs at a smaller distance and consequently is higher the parasitic capacitance causing 'more' current. Further details about this point will be provided in the subsequent simulation section.

5.2.2 Angle effects

A possible effect of the angle between the ESD gun tip and the target plane (β) is the reduction of the speed component perpendicular to the target. Referring to figure 5.10, the approach speed (S_{APP}) is decomposed into two components: $S_{\parallel}$ and $S_{\perp}$. The latter is the speed component proportional to $sin\beta$ and responsible for the discharge. The best case is for β = 90°, at which the gun is orthogonal to the target plane.

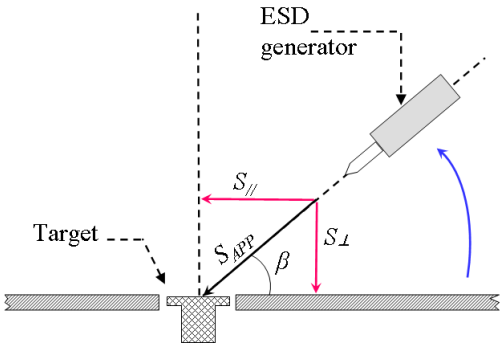

Figure 5.10: Effect of the angle between the gun and the target

Some tests have been done with different β values: i) 90°, i.e. the ideal case, ii) 75°, and iii) 60°. Results of the mean values for the case of 4 kV voltage with the 'normal' approach speed are summarized in figure 5.11, where an important reduction of the discharge waveform can be noted when the gun is not orthogonal to the metallic plate.

Other tests have been performed with the gun oriented as orthogonal as possible to the plate. This measure proves that for small variations of the gun angle (below 2°) the uncertainty discharge trend is very close to that obtained during the normal test.

5.2.3 Humidity effects

In order to investigate the effects of humidity, tests have been carried out within a calibrated climatic chamber. In this case, the EMC-Partner ESD 2000 gun equipped with an external control apparatus has been used, as shown in figure 5.12. Tests have been accomplished with

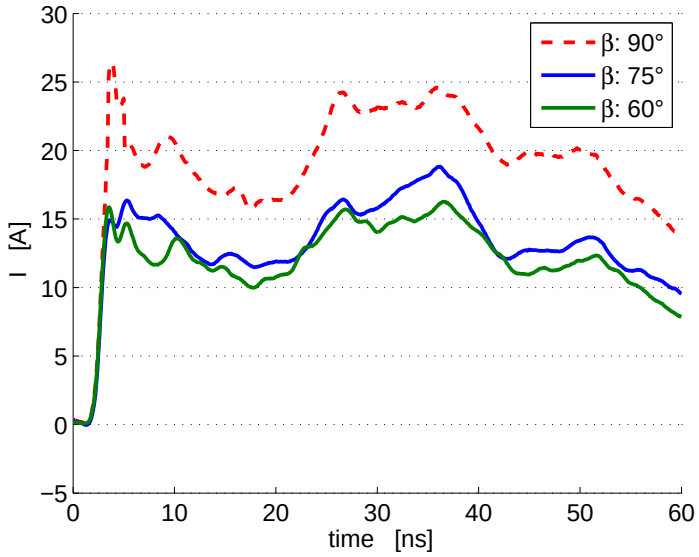

Figure 5.11: Angle effects: 4 kV voltage, 'normal' approach speed

a constant chamber temperature of 20°. In this scenario, quite the same results in terms of current waveforms have been obtained with respect to the case previously discussed.

Some results from the performed tests are summarized in table 5.4 in terms of peak current values I_P. Different relative humidity (RH) levels (35 and 50%), tip peak voltages (4 and 8 kV), and gun speeds have been considered in the tests.

I_P [A]	4 kV		8 kV	
	35% RH	50% RH	35% RH	50% RH
Very Fast	21.52	16.80	39.48	26.80
Fast	21.16	16.35	37.51	26.32
Normal	20.80	15.75	35.20	24.91
Slow	19.75	15.27	31.33	24.26
Very Slow	18.50	12.96	28.85	24.12

Table 5.4: Results with Humidity Variation

The results, also reported in figure 5.13, highlight a visible dependence of current peak values on humidity variations (from 20% up to 30%). This is due to the fact that the air itself, being dry, becomes a part of the electrostatic build-up mechanism. These results can be considered in good agreement with those documented in [36], where a strong correlation between RH and the peak current is shown. In [36], it is also shown that the peak current is approximately related to the inverse cube of RH. Therefore, for a given probability of ESD events, the current values at RH=15% are expected to be 20 to 40 times higher than at RH=45%.

5.3 Simulation Analysis

The model used in the simulations, sketched in figure 5.14, is based on the circuit described in [37]. Some modifications have been purposely introduced in order to better approximate the

Figure 5.12: ESD test into climatic chamber

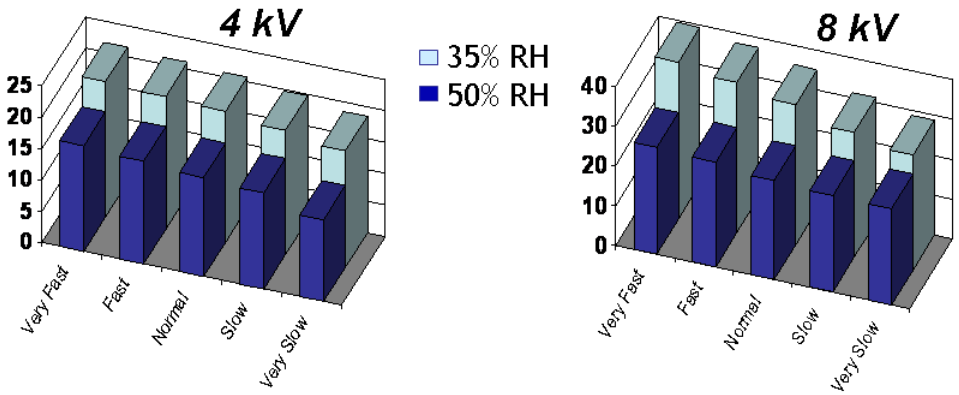

Figure 5.13: Histogram of humidity ESD variation

experimental waveforms of figure 5.6. The main parameters causing the different discharge current peak are the inductance associated to the tip (pLtip), and the stray capacitance between the ESD gun body and the target, or EUT (pCgb). These parameters change when an air discharge occurs and are dependent on the approaching speed of the ESD gun to the object. This means a greater stray capacitance pCgb and a lower inductance pLtip associated to the tip in the fast approach. The values considered for the simulations are: pCgb = 7.5 pF, pLtip = 0.14 μH for 'very slow' case; pCgb = 15 pF, pLtip = 0.1 μH for 'very fast' case. No intermediate speeds have been investigated. The length of the strap was 2 m.

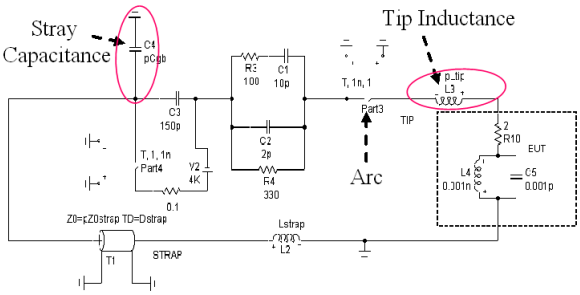

Figure 5.14: Equivalent circuit used for simulations

Figure 5.15 shows the simulation results of the discharge trend both for the very slow and the very fast approach. The figure confirms, once again, that the fast approach is the cause of a higher current peak. It is also important to emphasize that the ESD discharge generates a radiated field around and within the EUT. This field is the major responsible for failures in the victim apparatuses and its value is directly related to the current peak trend.

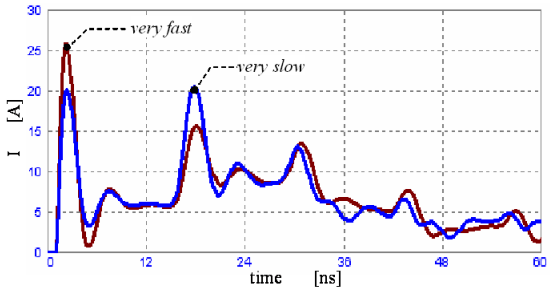

Figure 5.15: Simulation results for different approach speed

5.4 Uncertainty Budget

As defined in the ISO GUM [6], the type A uncertainty contribution of the performed current amplitude measurements is just the standard deviation of the obtained observations. In the previous tests, a visible variability of such observations has been noted upon the variation of the approach speed. In Table 5.5 the standard deviation of the current peak I_P is shown for the different speed cases previously analyzed.

I_P [A]	4 kV	6 kV	8 kV
Very Fast	2.34	1.08	7.85
Fast	3.15	10.76	2.47
Normal	1.87	11.45	6.05
Slow	3.65	6.65	8.27
Very Slow	2.04	5.99	11.75

Table 5.5: Standard Deviation of I_P

It can be observed that the variability does not seem to be related to the speed. This confirms that such tests are not very repeatable, although the same speed has been used during the test. However, the uncertainty of the discharge current also depends on the repeatability of the cable/adaptor connection, the measuring instrument errors, the current conversion factor of the target, the mismatch error between the input port of the DSO and the current transducer. In [33] an expanded uncertainty with confidence level of 95.5% is computed with a coverage factor k = 2. The relative uncertainty (U_{RE} %) is obtained by dividing the expanded uncertainty by the corresponding current parameter. A comparison between the combined uncertainty due to the different contributions and the uncertainty due only to speed and humidity variation is now considered. In Table 5.6 the relative uncertainty for the current peak I_P is shown. In case I, all the contributions obtained without approach speed and humidity effects [4] are considered, which corresponds to type B uncertainty. In the other cases, the uncertainties U_{RE} are computed using the mean values for each voltage level as a function of the speed variation, which corresponds to the type A uncertainty contributions. In case II, all the intervals between "very slow" and "very fast" are considered; in case III all the intervals between "normal" and "very fast" are taken into account; in case IV all the intervals between "very slow" and "normal" are instead accounted for. Indeed, in the case in which many repeated measurements are performed, there is a higher possibility to have a non-constant speed from one test to another: in this circumstance, cases III or IV are more likely. Finally the effects of humidity variation are summarized in case V for a normal speed and 15% humidity variation.

U_{RE} [%]	4 kV	6 kV	8 kV
case I	6.07	5.05	6.14
case II	21.39	25.40	24.93
case III	8.63	18.85	20.74
case IV	21.13	12.14	5.65
case V	39.07	28.76	48.41

Table 5.6: Relative speed Uncertainty of I_P

Since the effects of the other physical parameters on the uncertainty of repeated measurements are negligible, the errors due to the different speeds or humidity used during the test could reduce the effectiveness of any solution adopted to improve test repeatability. The effects of the angle can instead be contained by maintaining the gun as orthogonal as possible with respect to the target plane.

Chapter 6

TASER

Activity described in this chapter has been conducted in the Department of Electrical Engineering at the Houston University. Project regards measurement and analysis of field distribution in TASER *applications. In particular, a specific test bed has been realized and the effects of field variations due to the presence of a pacemaker in the human body are presented.*

The TASER M26 and the more recently deployed TASER X26 are battery operated electrical incapacitation devices (EIDs) that are becoming increasingly popular among law enforcement agencies as 'less-lethal' alternatives to firearms. The devices fire two tethered barbs at the target and pulses of high-voltage electricity are delivered through the conductive tethering wires.
The TASER discharge induces involuntary muscle contraction and intense pain. Although the mechanism underlying this action is not known with certainty, it is likely to involve one or more of the following: (1) direct stimulation of skeletal muscle; (2) indirect stimulation of skeletal muscle by way of the motor nerve innervation; (3) disruption of orderly signalling in proprioceptive feedback pathways [38].
Given the electrical nature of these incapacitation devices, it is perhaps not surprising that concerns have also been expressed regarding their potential to exert adverse effects on cardiac excitability. Moreover, the inducted current in the people who have a heart assistant like a pacemaker could have unknown effects.
In the spring of 2008, the EMC Laboratory in the University of Houston started a special research topic to study in depth the field distributions in the human body when a TASER discharge flows in the body itself. Thanks to my specific measuring skills, I was chosen by the Prof. Ji Chen to participate in the deployment of the project.

6.1 Waveform Analysis

The TASER generates a high-voltage waveform with a current of approximately 10 - 12 A depending on the load the device is fired into. The X26 TASER waveform is a fast, damped sinusoid having a fundamental frequency of about 120 kHz which, at the start of the pulse, is superimposed upon a unipolar double exponential pulse. The peak voltage of the X26 pulse

is about 300 V into a load of about 50 Ω and approximately 120 μs duration. The TASER device is a current source-it has a high output impedance-which means that any impedance it is fired into will not appreciably change the current amplitude unless it is a significant fraction of the TASER output impedance. Test data indicates a reduction in peak current of about 20% when the impedance is increased from 470 to 4700 Ω. The damping of the sinusoidal is also influenced by impedance [39].
The Shaped Pulse generator is the technology used in the X26 model (the same kind used in the next experiments). This technology uses a highly refined energy pulse that concentrates a small portion of energy to first penetrate the barrier, while the majority of electrical charge is held in reserve, flowing freely through the barrier once the leading edge has penetrated. The Shaped Pulse is comprised of two pulse phases. The first phase, called the 'Arc Phase' is optimized to generate a very high voltage (about 50kV) short duration pulse to penetrate clothing, skin or other barriers. Once the arc is created, the air in the arc is ionized and becomes a low impedance electrical conductor that conducts the second pulse phase into the body. The second phase is the 'Stimulation Phase' that does not have to arc across a barrier, since this was accomplished by the Arc Phase.

In order to acquire the current waveform with the digital oscilloscope (DSO) a specific current transducer has been realized, similar to the target used in electrostatic discharge tests (see chapter 5). A simplified scheme is the following:

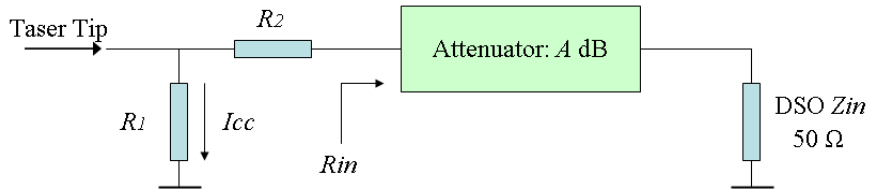

Figure 6.1: schematic of transducer

R_1 is the equivalent value of a set of parallel corona resistors, R_2 is the connection resistor, R_{IN} is the input resistance at the attenuator port, A represents the attenuation value in dB and V_{MIS} is the measured value.
Using the equation (6.1) it is possible to convert the voltage measured (V_{MIS}) with DSO in equivalent current through R_1.

$$\begin{aligned} I_{CC} &= f(R_1, R_2, R_{IN}, V_{MIS}, A) \\ &= \frac{R_2+R_{IN}}{R_{IN}} \cdot \frac{1}{R_1} \cdot 10^{\frac{A}{20}} \cdot V_{MIS} \end{aligned} \tag{6.1}$$

To prevent parasitic discharges, R_1 is made with a set of corona resistors placed around a hole in a metallic plate as suggested in the ESD standard [30] (details are given in figure 6.2(a)). Pictures of realized target are shown in figures 6.2(b) and 6.2(c).

To better investigate the effects of the load, it was necessary to determine the impedance between the darts in the model scenario to select the appropriate resistors as this can vary in shape and amplitude depending on the load the TASER is fired into. Based on the assumptions

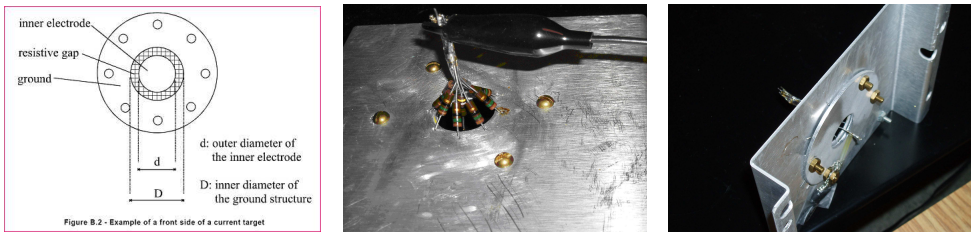

(a) (b) (c)

Figure 6.2: (a) target details - (b) and (c) pictures of target

that the TASER barbs completely penetrate the epidermis into the fatty tissue and the overall hand-to-foot impedance of the human body is 750 Ω, the impedance between the electrodes for the 225 mm case was determined to be 6.3 Ω [38].
Two different solutions are so analyzed:
i) $R_1 = 2.6\Omega,\ R_2 = 51\Omega,\ R_{IN} = 92.8\Omega,\ A = 6dB$;
ii) $R_1 = 50.6\Omega,\ R_2 = 51\Omega,\ R_{IN} = 45.8\Omega,\ A = 21dB$.
Both current transducers have been calibrated using the DSO with a tracking generator. Attenuations (dB) in function of the frequency are plotted in figures 6.3(a) and 6.3(b) for $R_1 = 2.6\Omega$ and $R_1 = 50.6\Omega$ respectively. Figures show the limit of resistors at higher frequencies, however this is still good since the frequency of TASER waveform discharge is around 100 kHz.

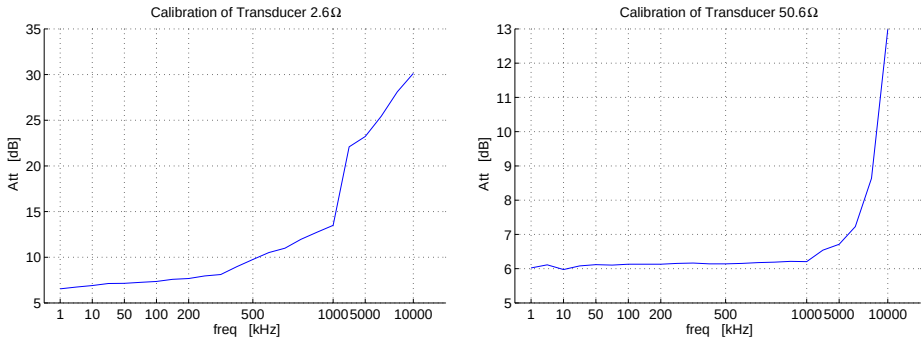

(a) (b)

Figure 6.3: Calibration of transducers

As before recalled, there are two TASER discharge phases: 'Arc Phase' and 'Stimulation Phase'. The last one is the measured phase during these tests, in fact air gap is directly simulated in a cartridge used for the tests as shown in figure 6.4.

For the measurement, a large metallic plane has been used for a good ground reference. Target was positioned over the ground plane and connected with a BNC cable to the attenuator and finally to the DSO (Tektronix TDS 3052B - 500 MHz) (figure 6.5). TASER tips are connected to the target from the cartridge with two wires 3 m long. Two different wire dispositions are analyzed: the one with the linear cables (lie flat) and the second with the roll up cables (figure 6.6).

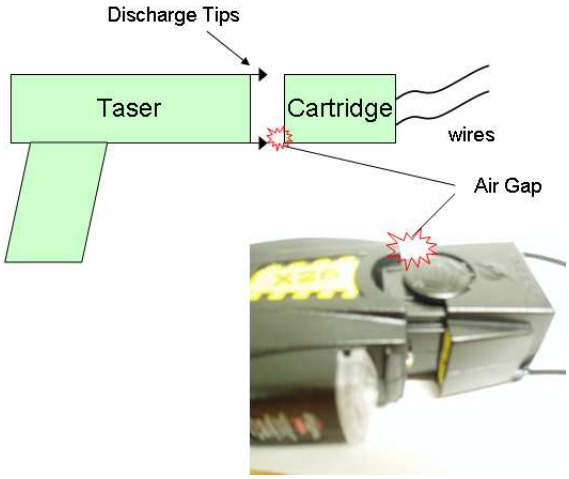

Figure 6.4: Air-Gap in the used cartridge

Figure 6.5: SetUp for waveform acquisition

Figure 6.6: Cable dispositions

Figure 6.7(a) shows the comparison between acquired waveform with linear and roll up wires using the transducer with equivalent $R_1 = 2.6\Omega$. FFT of these signals shows a signal frequency around 125 kHz. Figure 6.7(b) is like the previous one but with the transducer $R_1 = 50.6\Omega$.

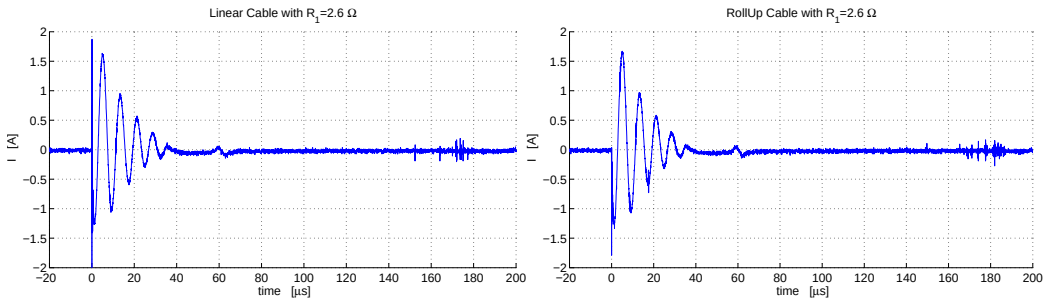

(a)

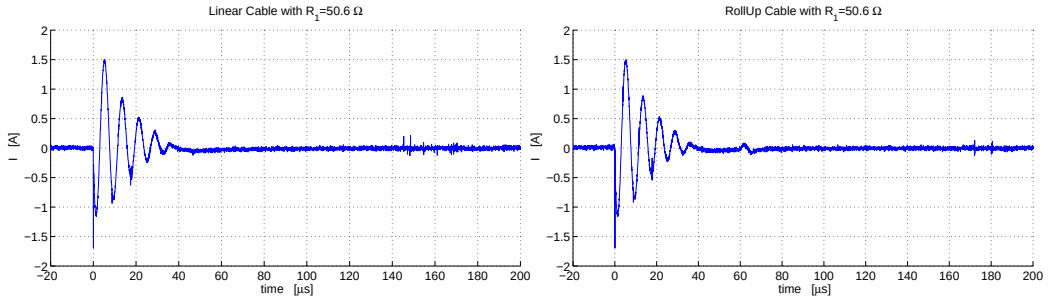

(b)

Figure 6.7: Comparison between different measurement configurations: (a) $R_1 = 2.6\Omega$ - (b) $R_1 = 50.6\Omega$

6.2 Field distribution

Human body is now approximated as a rectangular prism (cuboid) with the dimensions of 30 cm x 48 cm x h 30 cm and filled with 0.9% saline solution. The entire volume is divided in 45 cubes of about cm^3 10 x 10 x 10, as shown in figure 6.8(a). Taser tips are positioned in the middle of one face and are 20 cm spaced. (figure 6.8(b))

Experimental tests are performed analyzing the field distribution, for each cell, due to the TASER discharge, with the only saline solution and with a pacemaker positioned in the middle of the cuboid. The pacemaker consists of a box with dimensions 6 cm x 6 cm x 1.5 cm covered with metallic material.

6.3 Simulation Analysis

Computational electromagnetic modelling techniques were used to estimate electric and magnetic field in a digitized representation of the used box following application of the X26 TASER waveforms to the anterior side wall. A picture of the employed model is shown in figure 6.9.

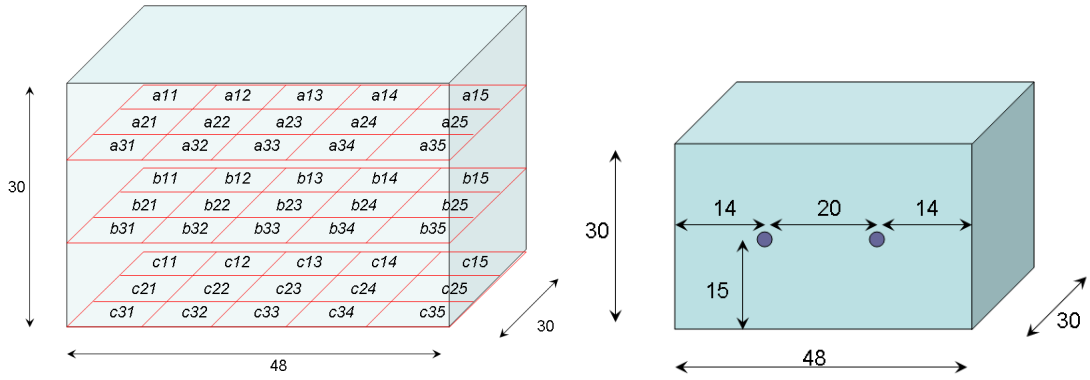

(a) (b)

Figure 6.8: (a) cuboid1 - (b) cuboid2

Signal is applied using 2 long wires and the model represents the plastic box with the saline solution.

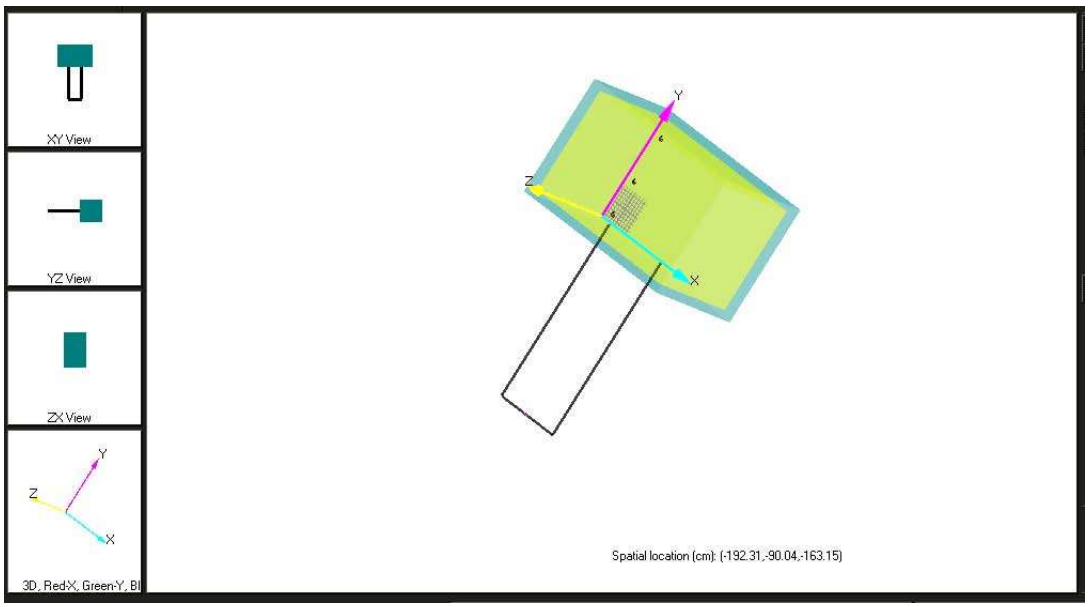

Figure 6.9: Employed model for the simulations

The prediction data was derived from the modelling for the position 'b23' both for electric (Ex, Ey) and magnetic fields (Hyz, Hxz). Results of simulation analysis are presented in figures 6.10(a) and 6.10(b) for the electric field in directions Ex and Ey respectively, and in figures 6.11(a) and 6.11(b) for magnetic field Hyz and Hxz.

6.4 Experimental Results

To investigate the field distribution, a set of probes for near field analysis have been used (EMCO ETS 7405 Near Field Probe Set). In particular, one magnetic probe 6 cm loop diameter, one electric omni-directional ball and one electric selective stub have been chosen for the investigations. To perform the measurements, a plastic box was filled with 0.9% saline

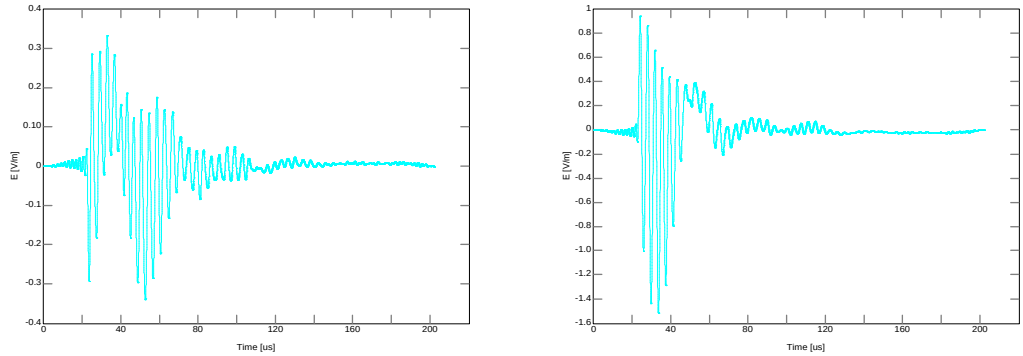

(a) (b)

Figure 6.10: Results of simulations analysis, Electric field

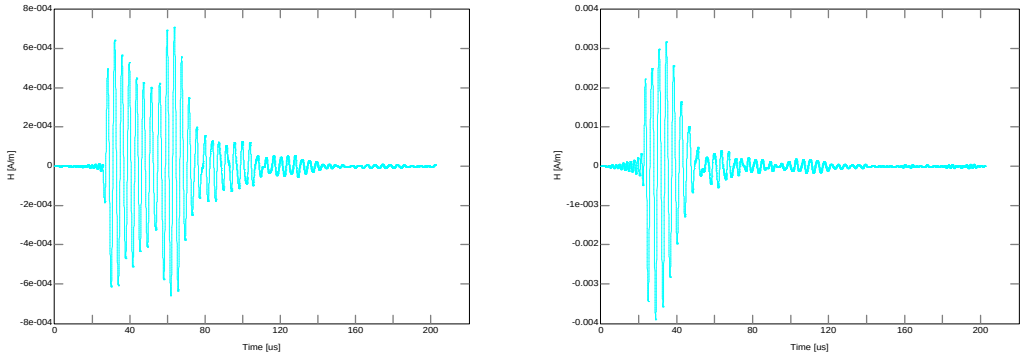

(a) (b)

Figure 6.11: Results of simulations analysis, Magnetic field

solution, and a special slide has been made to move the probes every time in the same position in the middle of the cells (see figure 6.12(a)). A particular of tips position is shown in figure 6.12(b). More pictures of the employed set up are shown in figures 6.13.

(a) (b) (c)

Figure 6.12: Details of used Box and axis orientation

6.4.1 Probes calibrations

Magnetic and electric probes are used for the tests. In the first case, it consists of a shielded loop antenna like the model used in the chapter 3 for the magnetic measurement. The original probes are not calibrated so the measure doesn't have physical sense since the antenna factors are unknown. However, as already shown in the chapter 3, it is possible to relate the voltage measured with the magnetic field through the probe when the antenna input impedance Z_{IN} is known. Moreover, since the frequency of analyzed waveforms are around 120 kHz ($\lambda \approx 1.5km$) the cable length is negligible so the constant concentrate model is applicable.

When a plane wave impinges upon the loop an open-circuit voltage develops across its terminals. This voltage is proportional to the incident magnetic flux with the relation (3.7): $V_{OC} = j\omega\pi a^2\mu_0 H$. When a load impedance Z_L is connected to the output terminals of the loop as shown in figure 6.14, the voltage V_{RX} across the load impedance is related to the input impedance Z_{IN} of the antenna by $V_{RX} = V_{OC}\frac{Z_L}{|Z_{IN}|+Z_L}$. We used the module of Z_{IN} since we obtained the RMS value of the voltage.

Under the hypothesis of $\theta = 90°$ and $\phi = 0°$ (see picture 3.4(a)), the H-field can be calculated from the measured voltage V_L on the 50Ω input resistance of the digital oscilloscope as [21]:

$$H_{rx} = V_L \frac{|Z_{IN}| + 50}{50} \frac{1}{j\omega\pi a^2\mu_S}$$

where a is the radius of the loop and $\mu_S \approx 1.25 \cdot 10^{-6}[H/m]$ the magnetic permeability of saline solution. The antenna input impedance Z_{IN} is measured by a vector network analyzed (VNA) in function of the frequency. Trends for the 6 cm magnetic loop in the range 0-1 MHz are reported in figure 6.15. The value of Z_{IN} in the range around 120 kHz is about $60 + j18$.

For the electric probes similar considerations can be made. From [21] we obtain:

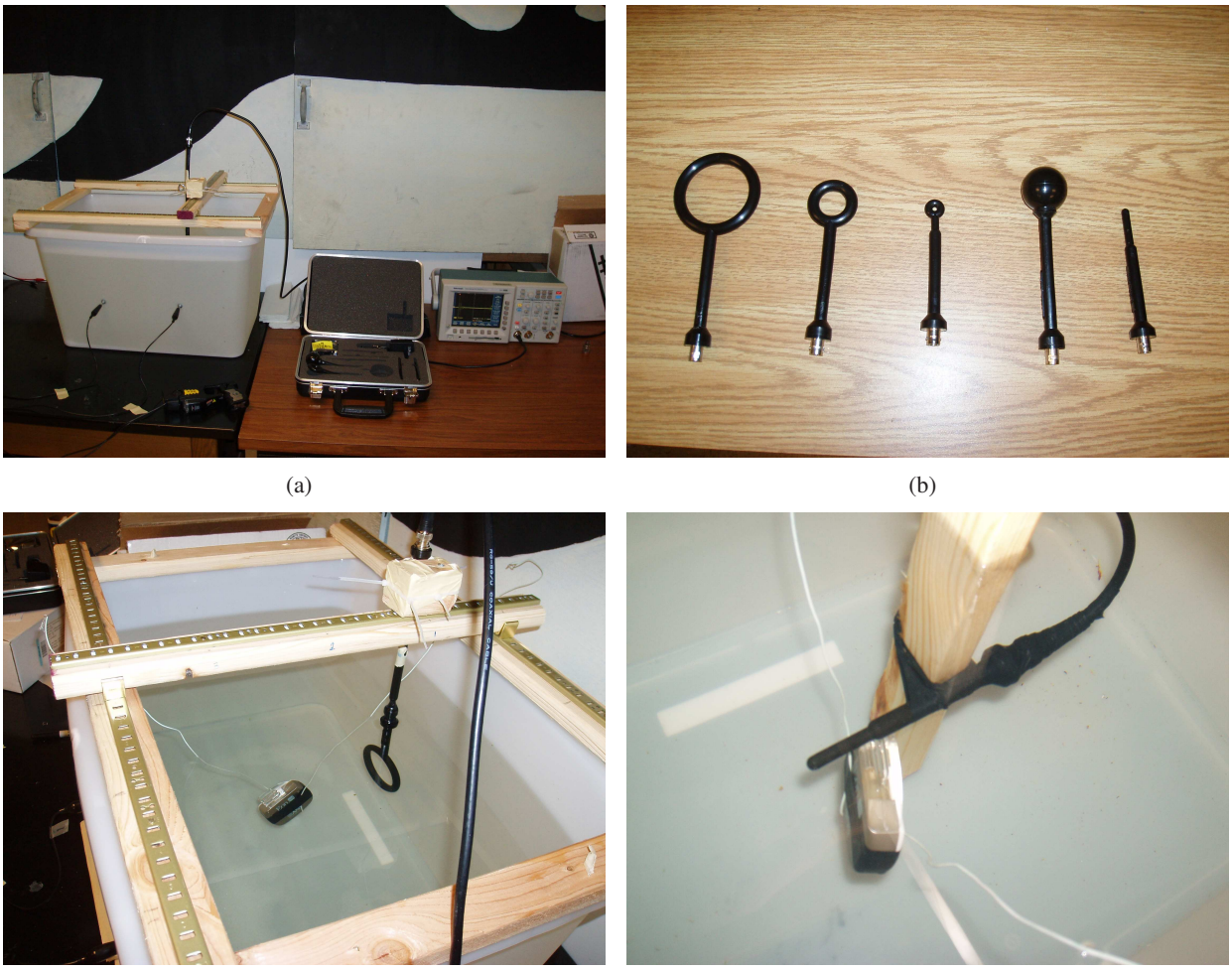

(a) (b)

(c) (d)

Figure 6.13: (a) Box Setup - (b) Emco probes - (c) Magnetic probe - (d) Electric stub

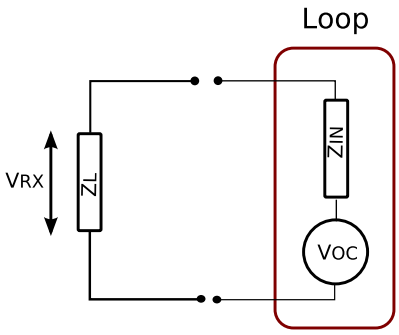

Figure 6.14: Equivalent circuit of loop antenna in receiving mode

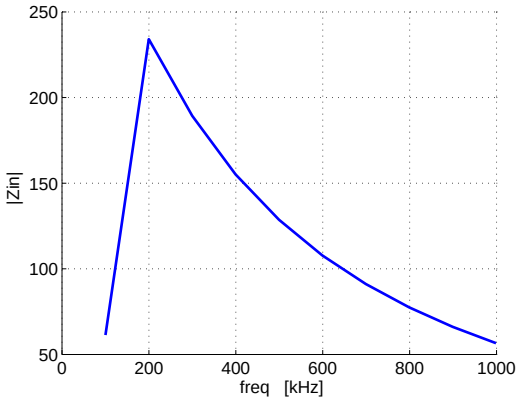

Figure 6.15: $|Z_{IN}|$ of 6 cm H Loop

$$E_{rx}^2 = \frac{|Z_{IN}|}{2}\sqrt{\frac{\mu_S}{\epsilon_S}}\left(\frac{V_L}{50}\right)^2$$

where V_L is the measured voltage, $\epsilon_S \approx 6.94 \cdot 10^{-10}[F/m]$ and $\mu_S \approx 1.25 \cdot 10^{-6}[H/m]$ the electric permittivity and the magnetic permeability of saline solution respectively. Magnitude of Z_{IN} in the range 0-1MHz for the directive electric stub and for the electric omni directional ball are reported in figures 6.16(a) and 6.16(b) respectively.

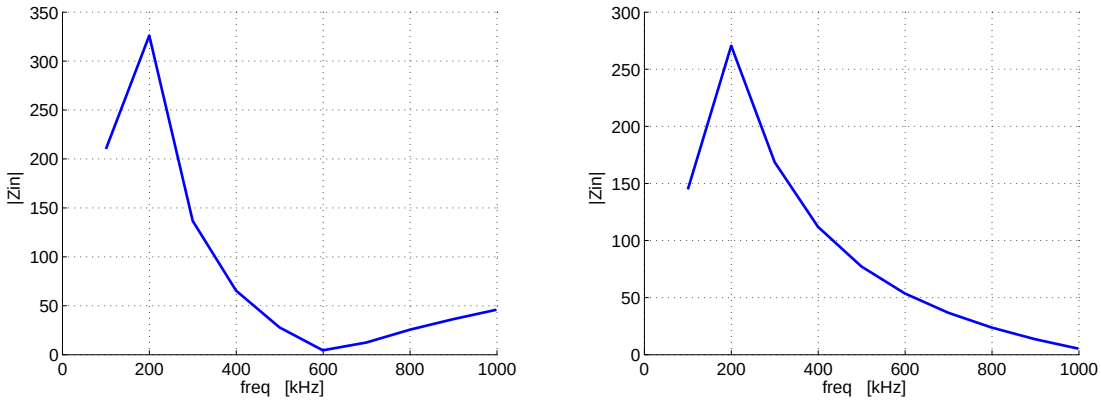

(a) (b)

Figure 6.16: $|Z_{IN}|$ of electric stub and omni directional ball

6.4.2 Measurement Analysis

The evaluation of field distribution is an important task, now some results are presented. The values of peak measured for magnetic and electric field are computed and three-dimensional figures are proposed to better understand the acquired measurement. For the magnetic field the loop was positioned in three different plane orientations: XY, XZ, YZ. In figures 6.17(a), 6.17(b), 6.17(c) magnetic field distributions are reported in the case with only saline solution, while in figures 6.17(d), 6.17(e), 6.17(f) the case with metallic pacemaker. The values in the

color bar are already presented in A/m. We can note the different values in function of the probe orientation and also an increasing of the field in the central area (layer 'b') when the pacemaker is present.

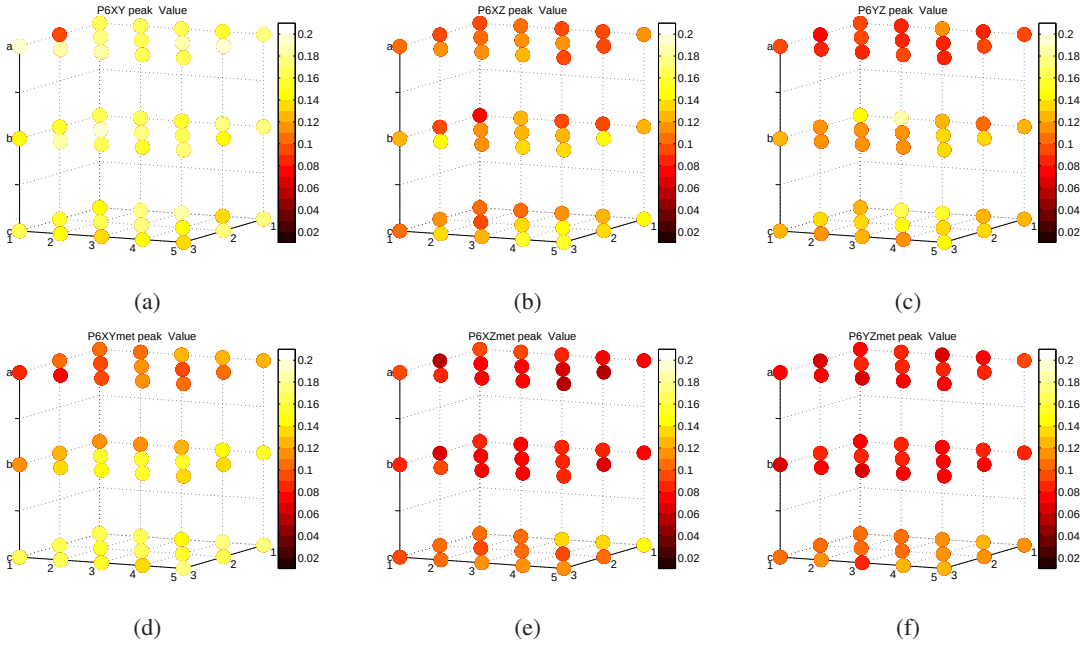

Figure 6.17: Magnetic Field Distribution [A/m]

Also for the electric field the distribution is plotted for each case with directional stub positioned in the three axes: x, y and z. Figures 6.18(a), 6.18(b), 6.18(c) present the values in the case without pacemaker and figures 6.18(d), 6.18(e), 6.18(f) present the case with pace maker. Also in this case we can note the different values due to the field polarization and distribution.

Finally the values measured with the omni directional ball are reported. Once again without and with pacemaker, figures 6.19(a) and 6.19(b) respectively.

6.4.3 Repeatability of Measurements

Also in these measure an analysis of repeatability is interesting for this thesis. The variation in the results is mainly due to the poor repeatability of the test. For example the mean value of ten repeated acquisitions with their variations are reported in figures 6.20(a) and 6.20(b) for E and H probe respectively in position b23.

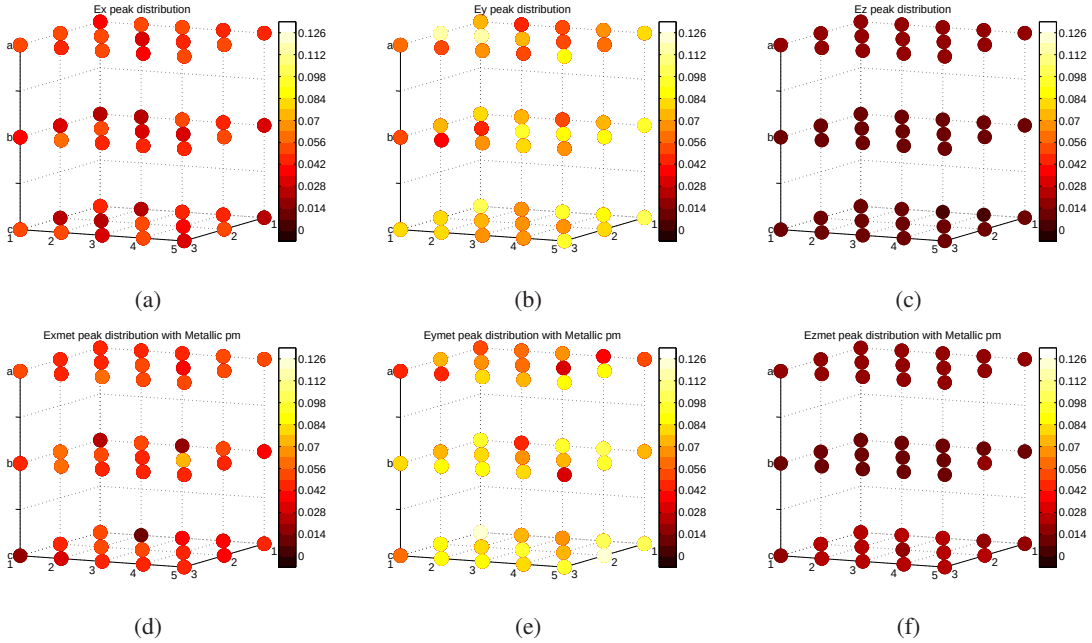

Figure 6.18: Electric Field Distribution [V/m] with directional probe

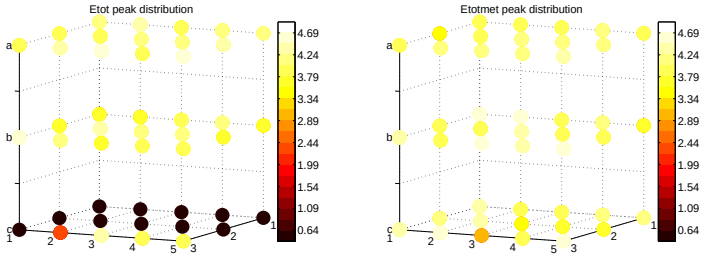

Figure 6.19: Electric Field Distribution [V/m] with omni-directional probe

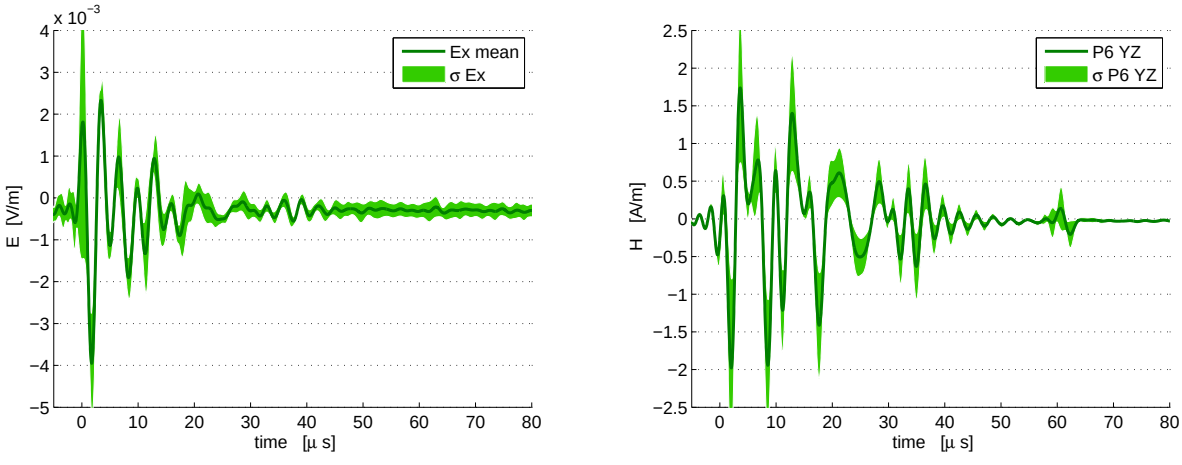

Figure 6.20: Variation in the measure, E and H

Chapter 7

Conclusions

A number of examples are presented in this thesis to underline the importance of the investigation into both the repeatability and the uncertainty of measurement.
In the first part some critical tasks regard the synchronization measure are analyzed. A procedure for precision time stamps is achieved with the support of specialized hardware interfaces in the physical layer of the network. Even with dedicated hardware, many legacy systems lack such hardware interfaces. A PTP protocol over Ethernet has been used to synchronize a common network (LAN) with software-only implementations. The results obtained so far show that synchronization to within 100 μs is feasible, but the system should be carefully designed to ensure that nodes are not overloaded by disk I/O activities and CPU tasks. This requires particular care in software development, to achieve a good repeatability.

In the second part of the thesis some EMC test set ups are proposed to address some critical repeatability issues. The purpose is to provide information and solutions allowing to enhance accuracy in calibration and test repeatability. The first example regards the characteristic of magnetic field propagation in a Semi-Anechoic chamber and the different response of the chamber walls as a function of the radiation sources. This is an important task especially for standards validation in term of normalized site attenuation (NSA). The theoretical radiated field has been first calculated by adopting the same hypothesis made for NSA prediction and then using a more generic hypothesis, i.e. near field area. Theoretical predictions and experimental measurements are compared. The obtained results highlight the need of some considerations about the 'near-field' area in the computation of NSA requirements.
Another case is the study of two improved adapters for LISN calibration. Meaningful results from simulations and experimental tests are given, showing the key role played by the LISN connector to reduce some parasitic effects, and the effectiveness of the proposed solutions. The calibration of LISN input impedance may be greatly affected by inductive parasitic effects of internal leads and external adapter. With the proposed adapters, accuracy and repeatability of these tests can be significantly enhanced. In particular the adapters allow to minimize the effect of parasitic inductances on $|Z_{IN}|$ and $\angle Z_{IN}$ estimates, and make the corresponding curves more regular and repeatable as a function of frequency. Besides, the mechanical design of the proposed adapters, made of only fixed parts, obliges the operator to perform the test always at

the same physical conditions of test bench components.
The repeatability contribution on the evaluation of uncertainty has also been analyzed for the air discharge tests. It has been shown that the type A uncertainty, which is not so important for contact ESD tests, becomes essential in the case of air ESD tests. In fact, if not adequately controlled, it may lead to a relevant degradation of the test repeatability in an ESD generator. Conflicting requirements are provided about this issue in the available standards. This means that lab technicians might interpret such requirements in different ways, to the detriment of the test repeatability. To this aim, a proposal has been reported based on a specific device, to be used for the control of the gun speed in air discharge tests. The uncertainty contribution associated to the humidity variation during the tests performed within the climatic chamber is also significant. It has been found that it must be below 2% with humidity variations lower than 1%.
Finally, a set of measurements aimed to understand the field distribution when a TASER discharge affects a human body is presented. Selected results from proper simulations and experiments are proposed to confer reliability and generality to the research activity. Details concerning the test bed, which includes a purposely-developed system, measurement procedure and experiment are also provided.

Appendix A

Matlab code for theoretical fields evaluation

```
clear all
close all

% DATA INPUT
a=0.0796; % radius of Tx loop [m]
b=0.0796; % radius of Rx antenna [m]
freq=60; % MHz
I=16/(52.18*sqrt(2)*2); % current [A RMS]
D=3; % antennas' distance [mt]
h2=[1:0.2:3]; % Rx antenna height 1-3 mt
Zrx=93.775; %|Z|Rx antenna
att= 10; % attenuation at Rx out [dB]
measureyz=[-78.10,-78.54,-78.66,-78.90,-78.99,-79.05,
                                        -79.18,-79.33,-79.56,-79.91,-80.30];
measurexy=[-78.31,-77.00,-75.43,-75.20,-74.88,-74.82,
                                        -74.80,-74.82,-75.29,-75.70,-76.40];
measurexz=[-76.32,-75.53,-74.74,-74.35,-73.84,-73.65,
                                        -73.88,-73.68,-74.02,-74.56,-75.05];


lung=300/freq; % wavelenght [m]
k=2*pi/lung; % wave number

% (Y-Z) Plane
measureyz=measureyz+att;
h1=1.1; % Tx antenna height
d1=(D^2+(h1-h2).^2).^0.5; % distance for direct waves
d2=(D^2+(h1+h2).^2).^0.5; % distance for reflected waves
Q1=pi/2; % theta 1
Q2=pi/2; % theta 2

H1r=j*(k*a^2*I*cos(Q1))./(2*d1.^2).*(1+1./(j*k.*d1)).*exp(-j*k.*d1);
H2r=j*(k*a^2*I*cos(Q2))./(2*d2.^2).*(1+1./(j*k.*d2)).*exp(-j*k.*d2);

H1Q=-((k*a)^2*I*sin(Q1))./(4*d1).*(1+1./(j*k.*d1)-1./(k.*d1).^2)
```

```
                                                    .*exp(-j*k.*d1);
H2Q=-((k*a)^2*I*sin(Q2))./(4*d2).*(1+1./(j*k.*d2)-1./(k.*d2).^2)
                                                    .*exp(-j*k.*d2);

Hr=H1r+H2r;
HQ=H1Q+H1Q;

Htot=abs(Hr+HQ); % theorical H-field received
Voc=sqrt(((10.^(measureyz./10))./1000).*50); % voltage at Rx loop terminal
Hmeas=Voc./((b*b*pi)*(4*pi*0.0000001)
                    *(2*pi*freq*1000000)); % H-field impinging upon the loop
err=Htot-Hmeas; % error between theorical  and practical results

figure('name', '|H|');
set(gca,'FontSize',12);
title('Y-Z plane @ 60MHz');
hold on;
grid;
plot(h2,Htot,h2,Hmeas,'o');
xlabel('\fontsize{12}  h2   [m]');
ylabel('\fontsize{12} |H| [A/m]');
hold off
pause;

figure('name', 'measured |H|');
set(gca,'FontSize',12);
title('Y-Z plane @ 60MHz');
hold on;
grid;
plot(h2,Hmeas);
xlabel('\fontsize{12}  h2   [m]');
ylabel('\fontsize{12} |H| Rx');
hold off
pause;

figure('name', 'Error Y-Z');
set(gca,'FontSize',12);
title('Y-Z Plane @ 60MHz');
hold on;
grid;
plot(h2,err);
xlabel('\fontsize{12}  h2   [m]');
ylabel('\fontsize{12} gap [dBm]');
hold off
pause;


% (X-Y) Plane
measurexy=measurexy+att;
h1=0.985; % Tx antenna height
d1=(D^2+(h1-h2).^2).^0.5; % distance for direct waves
d2=(D^2+(h1+h2).^2).^0.5; % distance for reflected waves
```

```
Q1=asin(D./d1); % teta 1
Q2=asin(D./d2); % teta 2

H1r=j*(k*a^2*I*cos(Q1))./(2*d1.^2).*(1+1./(j*k.*d1)).*exp(-j*k.*d1);
H2r=j*(k*a^2*(-I)*cos(Q2))./(2*d2.^2).*(1+1./(j*k.*d2)).*exp(-j*k.*d2);

H1Q=-((k*a)^2*I*sin(Q1))./(4*d1).*(1+1./(j*k.*d1)-1./(k.*d1).^2)
                                                    .*exp(-j*k.*d1);
H2Q=-((k*a)^2*(-I)*sin(Q2))./(4*d2).*(1+1./(j*k.*d2)-1./(k.*d2).^2)
                                                    .*exp(-j*k.*d2);

H1z=H1r.*cos(Q1)-H1Q.*sin(Q1);
H2z=H2r.*cos(Q1)-H2Q.*sin(Q2);

Htot=abs(Hr+HQ); % theorical H-field received
Voc=sqrt(((10.^(measureyz./10))./1000).*50); % voltage at Rx loop terminal
Hmeas=Voc./((b*b*pi)*(4*pi*0.0000001
                    )*(2*pi*freq*1000000)); % H-field impinging upon the loop
err=Htot-Hmeas; % error between theorical  and practical results

figure('name', '|H|');
set(gca,'FontSize',12);
title('X-Y plane @ 60MHz');
hold on;
grid;
plot(h2,Htot,h2,Hmeas,'o');
xlabel('\fontsize{12}  h2   [m]');
ylabel('\fontsize{12} |H| [A/m]');
hold off
pause;

figure('name', 'measured |H|');
set(gca,'FontSize',12);
title('X-Y plane @ 60MHz');
hold on;
grid;
plot(h2,Hmeas);
xlabel('\fontsize{12}  h2   [m]');
ylabel('\fontsize{12} |H| Rx');
hold off
pause;

figure('name', 'Error X-Y');
set(gca,'FontSize',12);
title('X-Y Plane @ 60MHz');
hold on;
grid;
plot(h2,err);
xlabel('\fontsize{12}  h2   [m]');
ylabel('\fontsize{12} gap [dBm]');
hold off
pause;
```

```
%(X–Z) Plane
measurexz=measurexz+att;
h1=1.1; %Tx antenna height
d1=(D^2+(h1-h2).^2).^0.5; %distance for direct waves
d2=(D^2+(h1+h2).^2).^0.5; %distance for reflected waves
Q1=asin((h2-h1)./d1); %teta 1
Q2=asin((h2+h1)./d2); %teta 2

H1r=j*(k*a^2*I*cos(Q1))./(2*d1.^2).*(1+1./(j*k.*d1)).*exp(-j*k.*d1);
H2r=j*(k*a^2*I*cos(Q2))./(2*d2.^2).*(1+1./(j*k.*d2)).*exp(-j*k.*d2);

H1Q=-((k*a)^2*I*sin(Q1))./(4*d1).*(1+1./(j*k.*d1)-1./(k.*d1).^2)
                                                    .*exp(-j*k.*d1);
H2Q=-((k*a)^2*I*sin(Q2))./(4*d2).*(1+1./(j*k.*d2)-1./(k.*d2).^2)
                                                    .*exp(-j*k.*d2);

H1z=H1r.*cos(Q1)-H1Q.*sin(Q1);
H2z=H2r.*cos(Q1)-H2Q.*sin(Q2);

Htot=abs(Hr+HQ); %theorical H–field received
Voc=sqrt(((10.^(measureyz./10))./1000).*50); % voltage at Rx loop terminal
Hmeas=Voc./((b*b*pi)*(4*pi*0.0000001)
                    *(2*pi*freq*1000000)); %H–field impinging upon the loop
err=Htot-Hmeas; %error between theorical and practical results

figure('name', '|H|');
set(gca,'FontSize',12);
title('X–Z plane @ 60MHz');
hold on;
grid;
plot(h2,Htot,h2,Hmeas,'o');
xlabel('\fontsize{12} h2 [m]');
ylabel('\fontsize{12} |H| [A/m]');
hold off
pause;

figure('name', 'measured |H|');
set(gca,'FontSize',12);
title('X–Z plane @ 60MHz');
hold on;
grid;
plot(h2,Hmeas);
xlabel('\fontsize{12} h2 [m]');
ylabel('\fontsize{12} |H| Rx');
hold off
pause;

figure('name', 'Error X–Z');
set(gca,'FontSize',12);
title('X–Z Plane @ 60MHz');
hold on;
```

```
grid;
plot(h2,err);
xlabel('\fontsize{12}  h2    [m]');
ylabel('\fontsize{12} gap [dBm]');
hold off
pause;
```

Bibliography

[1] ISO GUM, *Guide to the Expression of Uncertainty in Measurement*, Ed. 1, 1995. International Organisation for Standardisation, Geneva (Switzerland).

[2] Barry N. Taylor, Chris E. Kuyatt *Guidelines for Evaluating and Expressing the Uncertainty of NIST Measurement Results*, NIST First Ed.

[3] www.acmesystems.it

[4] D.L. Mills, "Network Time Protocol (Version 3) Specification, Implementation and Analysis", RFC 1305, *Internet Engineering Task Force Network Working Group*.

[5] N. M. Freris, P. R. Kumar, "Fundamental Limits on synchronization of Affine clocks in Networks", *Proc. of the 46th IEEE Conference on Decision and Control*, New Orleans, USA, Dec. 12-14, 2007.

[6] IEEE 1588^{TM} 2002, "Standard for a Precision Clock Synchronization Protocol for Networked Measurement and control Systems".

[7] G. Giorgi, C. Narduzzi, "Modeling and Simulation Analysis of PTP Clock Servo", *Proc. of ISPCS2007 Symposium*, Vienna, austria, October 1-3, 2007, pp. 155-161.

[8] Endace: *http://www.endace.com*.

[9] L. Benetazzo, C. Narduzzi, M. Stellini, "Analysis of clock tracking performances for a software-only IEEE 1588 implemetation", *Proc. of the Instr. Meas. Tech. Conf. IMTC2007*, Warsaw, Poland, May 1-3, 2007.

[10] W. Leland, M. Taqqu, W. Willinger, D. Wilson, "On the Self-Similar Nature of Ethernet Traffic", *IEEE/ACM Transaction on Networking*, vol. 2, February 1994, pp. 1-15.

[11] A. Erramilli, R. P. Singh, P. Pruthi, "Chaotic maps as models of packet traffic", *Proc. ITC 14. the Fundamental Role of Teletraffic in the Evolution of Telecommunication Networks*, 1994, pp. 329-338.

[12] P. Abry, D. Veitch, "Wavelet analysis of long-range-dependent traffic", *IEEE Transactions on Information Theory*, vol. 44. n. 1, 1998, pp. 2-15.

[13] D. L. Mills, P. H. Kamp, "The Nanokernel", *Proc. of the Precision Time and Time Interval (PTTI) Applications and Planning Meeting*, 2000.

[14] K. Correll, N. Barendt, M. Branicky, "Design Considerations for Software Only Implementations of the IEEE 1588 Precision Time Protocol", *Proc. of the 2005 Conference on IEEE 1588*, Zurich, Switzerland, October 10-12, 2005.

[15] EN 50081-1:1992 and -2:1993, *Electromagnetic compatibility - Generic emission standard*, BSI, 1992

[16] EN 50081-1:1997 (second edition) and -2:1995, *Electromagnetic compatibility - Generic immunity standard*, BSI, 1997

[17] CISPR 16-2-3 (edition 2.0), *Specification for radio disturbance and immunity measuring apparatus and methods - Part 2-3: Methods of measurement of disturbances and immunity - Radiated disturbance measurements*, July 2006

[18] CISPR 16-1-4 (edition 2.0) *Specification for radio disturbance and immunity measuring apparatus and methods - Part 1-4: Radio disturbance and immunity measuring apparatus - Ancillary equipment - Radiated disturbances*, Oct. 2007

[19] H.F. Garn, E. Zink, W. Mullwer, R. Kremser, *A new Instrument for the Determination of Product-Specific Chamber Factors for Radiated-Emissions Tests*, EMC Zurich 1993, pp. 93-98.

[20] CENELEC Technical Report R210-003, *Guidelines on how to use anechoic enclosure that do not fulfil the requirements regarding normalized site attenuation for pre-compliance tests of products*, Nov. 1995.

[21] Constantine A. Balanis, *Antenna Theory, -analysis and desing-* - Wiley- Interscince, 3th ed.

[22] A.A. Smith, Jr., R.F. German, and J.B. Pate, *Calculation of site attenuation from antenna factors*, IEEE Trans. Electr. Comp. vol. EMC-24, pp. 301-316, 1982.

[23] Michele Borsero, Andrea Dalla Chiara, Claudio Pravato, Alessandro Sona, Marco Stellini, Alessandro Zuccato. *Cosiderations about Radiated Emission Tests in Anechoic Chamber that do not fullfill the NSA Requirements*, IMEKO TC4 Symposium, 2008.

[24] Tim Williams: *EMC for product designer*, (second edition) BH NewNes, 1996.

[25] Clayton R. Paul: *Introduction to Electromagnetic Compatibility*, John Wiley & Sons, 1992.

[26] CISPR 16-1-2: 2006, *Specification for radio disturbance and immunity measuring apparatus and methods. Part 1.2: Radio disturbance and immunity measuring apparatus - Ancillary equipment - Conducted disturbances*, IEC, Ginevra.

[27] Bronaugh E. L., *Mains Simulation Network (LISN or AMN) Uncertainty - How Good are Your Conducted Emission Measurements ?*, EMC International Zurich Symposium on EMC, Zurich, February 1999, pp. 521 - 526.

[28] Zuccato A., Tomasin P., Florean D., *Undesired Uncertainty in Conducted Full-Compliance Measurement: A Proposal for Verification of Conformity of LISN Parameters According to Requirements of CISPR16-1*. IEEE International Symposium on EMC, Montreal, August 2001. Volume 1, pp. 7-12.

[29] International Standard - IEC 61000-4-6 *Electromagnetic compatibility (EMC) - Testing and measurement techniques - Immunity to conducted disturbances, induced by radio-frequency fields* Basic EMC publication (Ed. 2000).

[30] IEC, Std 61000-4-2, *Electromagnetic Compatibility (EMC), Part 4: Testing and measurement techniques - Section 2: Electrostatic discharge immuty test*, Ed. 1.2, 2001.

[31] ISO, Std 10605, *Road vehicles - Test methods for electrical disturbances from electrostatic discharge*, 2001.

[32] K. Hilty, H. Ryser, U. Herrmann, *Calibration of Electrostaic Dischareg Generators and results of an International Comparison*, IEEE Trans. on Instrumentation and Measurement, vol. 50, no. 2, Apr. 2001, pp. 414-418.

[33] K. Tae-Weon, C. Yeon-Choon, W. Sung-Ho, K. Hyo-Tae, *On the Uncertainty in the Current Waveform Measurement of an ESD Generator*, IEEE Trans. on EMC, vol. 42, no. 4, Nov. 2000, pp. 405-413.

[34] P. Richman, *Classification of ESD hand/metal current waves versus approach speed, voltage, electrode geometry and humidity*, Proc. IEEE Int. Symp. EMC, 1986, pp. 451-460.

[35] J.S. Maas and D.J. Pratt, *A study of the repeatability of electrostatic discharge simulator*, Proc. IEEE Int. Symp. EMC, 1990, pp. 265-269.

[36] M. Mardiguian, *Electrostatic Discharge, Interference Control Technologies*, Gainsville, Virginia, 1986.

[37] S.Caniggia, F. Maradei, *Circuit and Numerical Modeling of Electrostatic Discharge Generators*, IEEE Trans. On Industry Application, Vol.42, No.6, November/December 2006.

[38] S.J. Holden, R.D. Sheridan, T.J. Coffey, R.A. Scaramuzza and P. Diamantopoulos, *Electromagnetic modelling of current flow in the heart from TASER devices and the risk of cardiac dysrhythmias*, Phys. Med. Biol. 52 (2007) 7193-7209.

[39] Taser official web site, *www.taser.com*